UNIVERSITÀ DEGLI STUDI DI PADOVA

Dipartimento di Fisica e Astronomia "Galileo Galilei"

Master Degree in Physics

Final Dissertation

Investigation of Toroidal Magnetic Moments in

Dy-based molecular nanomagnets

External thesis supervisor

Prof. Oliver Waldmann

Internal thesis supervisor

Prof. Giovanni Mattei

Candidate

Denny Lamon

Academic year 2021/2022

Contents

Introduction

The magnetic properties of certain materials have been known since ancient times, and the first magnetic materials found in archaeology date back as far as the Egyptians, in the 4th millennium BC [1]. The magnetism of macroscopic materials has therefore been widely investigated for an extremely long time, but it is very recently (early 1990s) that nanoscopic materials have begun to take on particular significance, after the first reported single molecule magnet SMM [2]. Some molecules, in fact, are made up of metal atoms and display special magnetic properties that give hope for industrial uses in quantum technologies and information storing, favored by their nanometric sizes.

These molecules include those named *Single Molecule Toroics* or *Single Toroid Magnets* [3], in which the particular arrangement of the ions and their total magnetic moments generates what is called a *toroidal moment*. Intuitively it can be compared to an angular momentum of classical mechanics, and its presence would guarantee particular stability properties to the molecule. A promising example of toroidal molecules is given by compounds based on Dy^{3+} ions, with toroidal arrangement of the anisotropy axis and a non-magnetic ground state, subject of a large number of studies [4].

Also in this work, it will be analysed a new $3Dy^{3+}$ molecule, recently synthesised in the Institute of Inorganic Chemistry of the Karlsruhe Institute of Technology and not yet published. The aim will therefore be to derive the magnetic properties of this molecule and, in particular, to see if a direct measurement of the toroidicity is possible using an experimental apparatus.

In **chapter 2** it is provided a theoretical introduction to the main topics covered in this thesis, namely the spin Hamiltonian model used, definition of magnetization, susceptibility and toroidicity, and a theoretical overview of neutron scattering experiments.

Chapter 3 will show in more details the structure of the molecule, its magnetic properties and the adopted frame of reference.

In **chapter 4**, the complete Hamiltonian model will be first compared with the effective one. After that, fits of the experimental susceptibility and magnetization data will be performed, deriving a possible set of parameters which characterize the anisotropy axes. It will shown, however, that it is not possible to obtain complete information on the orientation of these axes (and thus on the toroidicity), which justifies the attempt to investigate the possibilities offered by other experiments (Inelastic Neutron Scattering).

Before having a closer look into the toroidicity of the molecule, a detailed study of its energy eigenvalues is carried out in **chapter 5**. In this way, we can better understand the orientation of the spin expectation values in the various energy levels, and then relate each energy level to a certain toroidal moment. In particular, it will be shown the analogous description between ferromagnetic and antiferromagnetic coupling under particular conditions of the anisotropy polar angles *theta*.

Chapter 6 will explore the toroidal moment of a compound of three Dy ions within the used spin

Hamiltonian model by varying the parameters on which it depends, in particular the reference system and the anisotropy polar angles *theta*. This will show the possibility that the studied Al_2Dy_3 molecule carries a toroidal moment, under the assumption of particular ideal azimuthal angles *phi*.

Finally, in **chapter 7** neutron scattering experiments will be simulated, showing how satisfactory results cannot be obtained by focusing only on the lower energy states of the molecule and/or considering a powder sample. Thus, preliminary results on the use of a single crystal inelastic neutron scattering will be shown.

Chapter 1

Motivation

Single molecule magnets (SMMs) have become the subject of extensive studies, given their possible applications in information storage or as quantum bits (QuBits) [5][6][7][8]. In fact, with this particular types of molecules it is possible to obtain a slow relaxation of the magnetization and long decoherence times. Previous works then (for ex. [9]) has shown the possibility of synthesising compounds with practically zero total magnetic moment, increasing the stability properties of the molecule.

Among these particularly stable molecules, there are those whose total magnetic moments arrangement give rise to a toroidal moment, defined as $\hat{\boldsymbol{t}} = \frac{g\mu_B}{2} \sum_{i=1,2,3} \boldsymbol{r_i} \times \hat{\boldsymbol{S_i}}$, where g is the Landé factor of the ions, μ_B the Bohr magneton, $\boldsymbol{r_i}$ and $\hat{\boldsymbol{S_i}}$ the vector position and spin operator of the i-esim ion. A clear analogy can be made with a classical angular momentum $\mathbf{L} = \mathbf{r} \times \mathbf{p}$, which tends to stabilize a rotating system. Toroidal molecules are bistable, presenting two spin configurations in the ground state in which the total magnetic moment is canceled out. The possibility of reducing the total magnetic moment favours a lower decoherence rate and increases the stability, since the molecule has a smaller possibility of coupling with external magnetic noises.

A $3Dy$ molecule in a triangular arrangement, therefore, is an ideal candidate to exhibit such properties. To avoid spin frustration, the total magnetic moments of the ions will tend to lie on the plane formed by the three ions themselves. If then, thanks to the contribution of the anisotropy, they are oriented in a circular, clockwise or anticlockwise manner, they can give rise to a toroidal moment.

But from the definition of toroidal moment, one can see a dependence on the positions of the three ions, whereas in the usual magnetic Hamiltonian model, there are only relations between the spins, and it is therefore invariant on the positions of the ions. Moreover powder susceptibility and magnetization measurements have trends that can be described with such a Hamiltonian model; therefore it is not possible to derive complete information on the toroidicity of the molecule since the dependency on the position cannot be investigated.

For this reason, other types of experiments must be considered, and, in particular, in this thesis work we will simulate the possible results of inelastic neutron scattering experiments. The intensity peaks of the transitions from one state to another of the molecule have in fact a dependence on the scattering vector of the neutrons, thus enclosing a position dependence.

Chapter 2

Theoretical Background

2.1 The spin Hamiltonian model

The key point in the modelling of the magnetic behaviour of molecules is the choice of the Hamiltonian, through which all thermodynamic properties of interest can be derived. The Hamiltonian operator then allows to obtain the energy eigenvalues of the system when applied to the relative eigenfunctions. The latter live in a Hilbert space constructed from the bases of the angular moments of each of the ions in the molecule. We need so an Hamiltonian in which only spin-related interactions are taken into account to describe the magnetic properties we are interested in.

Among these interactions, the fundamental contributions are: the Heisenberg exchange interaction, which can be assumed between neighbouring spins in a cluster and is linked to both a Coulombian action and the Pauli principle; an anisotropy term, related to the environment in which the system is immersed; the Zeeman interaction, which tends to align the magnetic moments (spins) with an external magnetic field. In formulae, the complete Hamiltonian is thus given by:

$$H = -\sum_{i,j} \mathbf{S}_i \cdot \mathbf{J}_{i,j} \cdot \mathbf{S}_j + \sum_i \mathbf{S}_i \cdot \mathbf{D}_i \cdot \mathbf{S}_i + \mu_B \sum_i \mathbf{S}_i \cdot \boldsymbol{g_L} \cdot \boldsymbol{B} \qquad (2.1)$$

Further explanations of the various terms that make up Hamiltonian are given in the following. It can be shown that in the case of isotropic exchange interactions between ions in the cluster, the Hamiltonian just described commutes with the total spin operator $\hat{S}^2$. This makes possible a spin-based description of the eigenfunctions.

It is important to make clear from the outset the nomenclature that will be used throughout. In particular, the term "spin" or "total spin" will be used to indicate the total magnetic moment given by the sum of the orbital magnetic moment and the usual spin magnetic moment.

2.1.1 Heisenberg coupling

The Heisenberg coupling is the term of the Hamiltonian that summarizes the interactions between couples of spins. The classical Hamiltonian of interaction between two electrons is

$$H = \frac{p_1^2}{2m_e} + \frac{p_2^2}{2m_e} + V(\mathbf{r}_1, \mathbf{r}_2)$$

thus simply a sum of two kinetic terms and one interacting potential term, without considering the spin of the particles.

However, due to the Pauli exclusion principle, the wave functions of the two particles must contain a spin-orbit term, which leads to a splitting of the energy levels into a triplet and singlet spin state. Therefore it must be considered an additional term in the Hamiltonian that operates in spin space and, in particular, that describes the coupling between the spins of the particles. It is possible to show that this Hamiltonian is simply related to the dot product between the spin vectors and, up to an additive constant that can be omitted by redefining the zero energy, it is given by the Heisenberg model, namely:

$$H = -\sum_{i,j} \mathbf{S}_i \cdot \mathbf{J}_{i,j} \cdot \mathbf{S}_j \tag{2.2}$$

where we directly considered the sum of the interactions between all the pairs of spin.

The terms $\mathbf{J}_{i,j}$ are tensors that describe the spins interactions, but in general they are not symmetric and not traceless. It is so possible to write them as a sum of three contributes, namely:

$$H = -\sum_{i,j} J_{i,j} \mathbf{S}_i \cdot \mathbf{S}_j + \sum_{i,j} \mathbf{S}_i \Delta_{i,j} \mathbf{S}_j + \sum_{i,j} \mathbf{d}_{i,j}^{DM} \cdot (\mathbf{S}_i \times \mathbf{S}_j) \tag{2.3}$$

these three terms are respectively:

- *isotropic exchange*, $T0$[1] tensor describing the scalar product which tends to align the spins in a parallel or antiparallel manner, depending on whether the sign is positive ($J > 0$, ferromagnetic) or negative ($J < 0$, antiferromagnetic); it can be represented as a diagonal matrix.

- *anisotropic exchange*, traceless $T2$ tensor derived from the dot product, which tends to align the spins along a certain spacial direction given by the anisotropy axes, and it includes non-diagonal terms in the matrix.

- *antisymmetric exchange*, traceless $T1$ tensor derived from the cross product, which tends to align the spins in different directions by 90° from each other; it is also known as Dzyaloshinskii–Moriya interaction.

Therefore in the code that will be used for the simulations, the input values are specified and then converted into 3D matrices. These can be then summed up and multiplied by the spins to describe the complete exchange Heisenberg coupling. Very often, however, the Dzyaloshinskii–Moriya term makes a negligible contribution to the energy. The Hamiltonian will be therefore considered in the following simulations as a simple sum of the isotropic and anisotropic terms; further description is given in the following.

2.1.2 Magnetic anisotropy

Every day experience shows that, when we are dealing with magnets, a fundamental aspect to take into account is the direction of alignment in space. Well known is, for example, the tendency of a magnetic bar to align itself with respect to another bar to which it is near, or the tendency of a metallic needle to align with respect to the Earth magnetic field, process behind the operation of compasses. Thus, similarly, even at the microscopic scale of molecules, materials are more likely to magnetize in one direction than another. This different material response to different spatial orientations is called *magnetic anisotropy*.
As we pointed out above, the magnetic properties of an atomic specie are governed by the

---

[1]The notation Tn refers to a tensor of n-esim order.

electronic structure, and so by the arrangement of the electrons in the atom. The spin of a single electron has spherical symmetry, and so the description would be completely isotropic, as there would be no difference between the different orientations in space. On the other hand the anisotropy causes a distortion of the symmetry and a removal of the degeneracy of the energy eigenvalues. This occurs in the coupling between the spin and a possible source of anisotropy like the orbital motion of the electron itself or an external magnetic field. We can in fact summarise the main sources of anisotropy in three different phenomena: the anisotropic interaction between two neighbour spins; the interaction with an external magnetic field; the anisotropy of the single ion, which depends on the interaction between spin-orbit coupling and the crystalline field.

Intuitive origin of anisotropy

Each of the three Dy^{3+} ions has 7 valence electrons that can be arranged in the seven different f atomic orbitals, represented in different shapes and shown in figure 2.1.
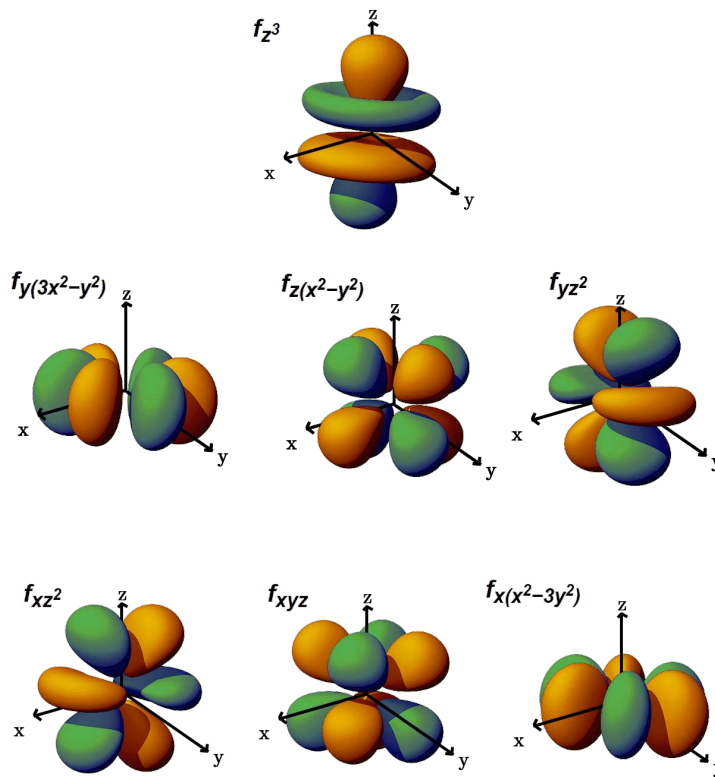

Figure 2.1: Angular distribution of f orbitals.

As it is straightforward to see, none of the seven orbitals present a spherical symmetry, characteristic that is typical only of the s orbital. So one can expect an angular dependency of the electric density of the electrons that occupy different orbitals.

Moreover each ion is embedded in a complex structure of atoms that does not show a high symmetry; in fact if the environment was spherically symmetric each electron would experience the same global electrical effect. But in this case, due to the more complex structure, the different f orbitals can overlap in a more ore less strongly way with the atomic orbitals of the surrounding elements. This leads therefore to dissimilar Coulomb interactions and so to different energy levels in which the electrons of the Dy ions can sit. In other words, the initial $2J + 1$ degeneracy of the energy level of the electrons is partially removed and the f orbitals are split in the interactions with the neighbouring ions and this effect is also called *ligands field splitting*.

It is clear, therefore, how different ligand structures lead to a symmetry break in the molecule, and thus to the anisotropy.

Mathematical description

Mathematically the interactions between the metal ions and the surrounding ligands are described by the *Crystal Field Theory* (CFT), in which each ligand is approximated with a point charge. In this view the interaction is simply treated as a Coulomb term depending on the charge density of the neighbour atoms and on their relative distance with the ion. The complete Hamiltonian was computed for the first time by Stevens[10] in 1952, applying the Wigner-Eckart theorem to the expansion in spherical harmonics of the Coulomb potential, and it can be written as:

$$\widehat{H}_{LF} = \sum_{k,q} B_{kq}\widehat{O}_{kq} \qquad \text{with } |q| \leq k \text{ and } k > 0 \tag{2.4}$$

where k is limited by the orbital angular momentum number of a partially filled shell of the ion.

- B_{kq} are called *crystal field parameters*, which should be calculated considering the actual charge distribution of all the ligands. The calculation is very tedious and therefore certain approximations are used, such as the not rigorous point-charge model, which we mentioned above, or are used values coming from spectroscopic measurements. In any case they depend on the coupling between the ion and the ligand structure, and so they has to be calculated for each different molecule.

- $\widehat{O}_{kq}$ are then the *Stevens Operators*, and can be written as a combination of the angular momentum operators $\widehat{S}_x$, $\widehat{S}_y$ and $\widehat{S}_z$; these values strongly depend on the symmetry of the molecule, which determines whether their value is zero or not.

The expressions of the first Stevens Operators up to $k = 2$ are listed in the following:

$$\begin{aligned}
\hat{O}_{20} &= 3\hat{S}_z^2 - \hat{S}^2 = 2\hat{S}_z^2 - \hat{S}_x^2 - \hat{S}_y^2 \\
\hat{O}_{21} &= \frac{1}{4}\left[\hat{S}_z\left(\hat{S}_+ + \hat{S}_-\right) + \left(\hat{S}_+ + \hat{S}_-\right)\hat{S}_z\right] = \frac{1}{2}\left[\hat{S}_z\hat{S}_x + \hat{S}_x\hat{S}_z\right] \\
\hat{O}_{2-1} &= \frac{1}{4i}\left[\hat{S}_z\left(\hat{S}_+ - \hat{S}_-\right) + \left(\hat{S}_+ - \hat{S}_-\right)\hat{S}_z\right] = \frac{1}{2}\left[\hat{S}_z\hat{S}_y + \hat{S}_y\hat{S}_z\right] \\
\hat{O}_{22} &= \frac{1}{2}\left[\hat{S}_+\hat{S}_+ + \hat{S}_-\hat{S}_-\right] = \hat{S}_x^2 - \hat{S}_y^2 \\
\hat{O}_{2-2} &= \frac{1}{2}\left[\hat{S}_+\hat{S}_+ - \hat{S}_-\hat{S}_-\right] = \hat{S}_x\hat{S}_y + \hat{S}_y\hat{S}_x
\end{aligned} \tag{2.5}$$

The above coefficients are those commonly used to describe the Hamiltonian up to second order, or in the so called *zero-field splitting* approximation. By inserting these results in equation 2.4, and making the matrix notation explicit, one can arrive at a writing of the type

$$\widehat{H}_{LF}^{k=2} = \begin{pmatrix} \hat{S}'_x & \hat{S}'_y & \hat{S}'_z \end{pmatrix} \cdot \begin{pmatrix} B_{22} - B_{20} & B_{2-2} & \frac{1}{2}B_{21} \\ B_{2-2} & -B_{22} - B_{20} & \frac{1}{2}B_{2-1} \\ \frac{1}{2}B_{21} & \frac{1}{2}B_{2-1} & 2B_{20} \end{pmatrix} \cdot \begin{pmatrix} \hat{S}'_x \\ \hat{S}'_y \\ \hat{S}'_z \end{pmatrix} = \hat{S}'\mathbf{B}\hat{S}' \tag{2.6}$$

where the notation "'" has been inserted in the Stevens operators to distinguish the spin operators that will be used later.

It is therefore possible to make some redefinitions of the matrix elements, in particular introducing the quantities D' and E' such that

$$B_{20} = \frac{1}{3}D, \quad B_{21} = 2D_{xy}, \quad B_{2-1} = 2D_{yy}, \quad B_{22} = E, \quad B_{2-2} = D_{xy}$$

In this way the Hamiltonian can be written in a simplified way, introducing the *anisotropy tensor* $\mathbf{D}'$, with which the Hamiltonian becomes:

$$\hat{S}'\mathbf{D}'\hat{S}' = \begin{pmatrix} \hat{S}'_x & \hat{S}'_y & \hat{S}'_z \end{pmatrix} \cdot \begin{pmatrix} -\frac{1}{3}D' + E' & D'_{xy} & D'_{xz} \\ D'_{xy} & -\frac{1}{3}D' - E' & D'_{yz} \\ D'_{xz} & D'_{yz} & \frac{2}{3}D' \end{pmatrix} \cdot \begin{pmatrix} \hat{S}'_x \\ \hat{S}'_y \\ \hat{S}'_z \end{pmatrix} \tag{2.7}$$

The latter has simply been found rewriting in a different notation the tensor $\mathbf{B}$, which is traceless, real and symmetric. This means that its eigenvalues $(\lambda_1, \lambda_2, \lambda_3)$ have to be real and the eigenvectors $(\overrightarrow{v}_1, \overrightarrow{v}_2, \overrightarrow{v}_3)$ are real and orthonormal. As a consequence it is always possible to find an orthogonal frame of reference in which the tensor is diagonal, so all the non-diagonal terms are vanishing. This procedure consists of nothing more than aligning one of the axes of the reference system with the principal axis of anisotropy. In this new notation[11] the Hamiltonian reads:

$$\hat{S}\mathbf{D}\hat{S} = \begin{pmatrix} \hat{S}_x & \hat{S}_y & \hat{S}_z \end{pmatrix} \cdot \begin{pmatrix} -\frac{1}{3}D + E & 0 & 0 \\ 0 & -\frac{1}{3}D - E & 0 \\ 0 & 0 & \frac{2}{3}D \end{pmatrix} \cdot \begin{pmatrix} \hat{S}_x \\ \hat{S}_y \\ \hat{S}_z \end{pmatrix} \tag{2.8}$$

Where the anisotropy tensor, as pointed out above, is a diagonal matrix like:

$$\mathbf{D} = \begin{pmatrix} D_{xx} & 0 & 0 \\ 0 & D_{yy} & 0 \\ 0 & 0 & D_{zz} \end{pmatrix}$$

in which, by convention, it holds usually $|D_{zz}| > |D_{yy}| > |D_{xx}|$, and the ratio E/D is usually limited in the range

$$-1/3 \leqslant E/D \leqslant 1/3$$

since out of this range the same physics is described unless a rotation of the reference system.

It is then straightforward to relate the entries of the $\mathbf{D}$ matrix to the D and E values defined above:

$$D = D_{zz} - \frac{1}{2}(D_{xx} + D_{yy}), \qquad E = \frac{1}{2}(D_{xx} - D_{yy})$$

Computing the matrix product in 2.8 and neglecting the constants, it is possible to write the anisotropy Hamiltonian as:

$$\widehat{H}_{anis} = D\widehat{S}_z^2 + E(\widehat{S}_x^2 - \widehat{S}_y^2) \tag{2.9}$$

from which it is easy to distinguish the spatial dependencies of the different contributions in energy. In fact if $E = D = 0$ no magnetic anisotropy is present and the system is isotropic. If $E = 0 \neq D$ an axial symmetry occurs with one of the eigenvalues of the tensor that becomes bigger than the others so the spin has a preferential orientation called *easy axis*. When E is non zero the reduction of symmetry leads to an additional anisotropy in the xy plane, with a consequent removal of degeneracy and splitting of the energy eigenvalues even in the absence of a magnetic field (from here the name *zero-field splitting*).
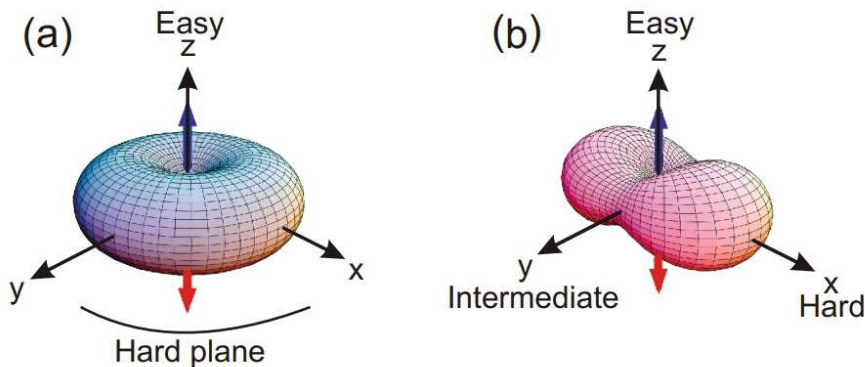
Figure 2.2: Anisotropy energy contribution in a Cartesian frame of reference; uniaxial symmetry on the left (a) and second order correction with the anisotropy term E on the right (b).

An intuitive representation of the behaviour of anisotropy can be seen in the figure 2.2, in which the energy of a classical spin is represented in a Cartesian graph ([12]).

The E value breaks so the symmetry and introduces in general a splitting in the energy eigenvalues; but in the case of the molecules analyzed in this work, so made up of $3Dy^{3+}$ of spin 15/2, the lowest single ion energy spin state is $|\pm 15/2\rangle$, and the energies are non affected by this E term. In fact, looking at the effect of the anisotropy from a perturbation theory point of view, the second order correction is related to the product

$$\left\langle -\frac{15}{2}\middle|\widehat{E}\middle|m\right\rangle\left\langle m\middle|\widehat{E}\middle|-\frac{15}{2}\right\rangle$$

with m a general state. Knowing the structure of the $\widehat{E}$ operator, see eq. 2.9, it is straightforward to see how there is no state m that makes the expression non-null. So at this order of perturbation no energy splitting is introduced in the Dy molecule; only a quadratic curvature of the energy eigenvalues is present, due to terms like $\left\langle -\frac{15}{2}\middle|\widehat{E}\middle|m\right\rangle\langle m|\widehat{E}\middle|-\frac{15}{2}\rangle$ with $m = 15/2$ which introduce this quadratic dependency on E.

Anticipating what will be discussed in chapter 7, it can be pointed out that in neutron scattering experiments it is possible to assess the presence of the anisotropy E term despite not having splitting in energy. In fact, the neutron scattering technique does not only provide information on energies, but also on wave functions where the E term can introduce some changes.

2.1.3   Zeeman term

Another way in which the symmetry of the system can be broken is through the application of an external magnetic field, since the space in which the atoms are immersed is no longer isotropic. In this case, the different possible orientations of the total angular momentum J, i.e. the different possible values of the quantum number m_J, are no longer degenerate, which leads to a further splitting of the energy levels.

To explain this phenomenon, it can be considered that each particle possesses an orbital angular momentum given by the application of the $\hat{\mathbf{L}}$ operator to the wave function, which can be seen as a quantum extension of the classical definition $\mathbf{L} = \boldsymbol{r} \times \mathbf{p}$ through the momentum operator $\hat{\mathbf{p}} = -i\hbar\nabla$. It is then possible to define a magnetic dipole moment associated with the orbital angular momentum $\mathbf{L}$, given by:

$$\boldsymbol{\mu_L} = -g_L\mu_B\mathbf{L} \tag{2.10}$$

with $\mu_B = \frac{e\hbar}{2m} = 9.27 \times 10^{-24} \; A \cdot m^2$ the *Bohr magneton* and $g_L = 1$ the gyromagnetic factor of the orbital angular momentum. Similarly, it is also possible to define a dipole moment for the spin angular momentum, given by:

$$\boldsymbol{\mu_S} = -g_S \mu_B \mathbf{S} \tag{2.11}$$

where this time the spin-related gyromagnetic factor is 2.00231, and can be measured with extreme experimental precision [13].

Then by adding the two magnetic moments defined above, the total angular momentum can be derived, namely:

$$\boldsymbol{\mu} = \boldsymbol{\mu_L} + \boldsymbol{\mu_S} = -\mu_B(g_L \mathbf{L} + g_S \mathbf{S}) \tag{2.12}$$

Therefore, by introducing an external magnetic field $\mathbf{B_{EXT}}$, the ion will be subjected to an external momentum given by $\boldsymbol{\tau} = \boldsymbol{\mu} \times \mathbf{B_{EXT}}$, and it can be shown ([14]) that this results in an energy change given by:

$$\delta E = g_L \mu_B B M J \tag{2.13}$$

where g_J is called *Landé factor* and can be computed as:

$$g_L = 1 + \frac{J(J+1) + S(S+1) - L(L+1)}{2J(J+1)} \tag{2.14}$$

We will see (chapter 3) that a Dy^{3+} ion has total, spin and orbital quantum number respectively equal to $J = \frac{15}{2}$, $S = \frac{5}{2}$ and $L = \frac{10}{2}$. It is so straightforward to compute the Landé factor, which value is equal to:

$$g_L = \frac{4}{3} \simeq 1.33333 \tag{2.15}$$

Finally, the equation 2.13 can be generalised by considering not only the projection of angular momenta along the Z axis, but in all the three dimensions. Thus calling $\mathbf{S}$ the total angular momentum ($\mathbf{J}$ above), the presence of the magnetic field in the ion system adds a term to the Hamiltonian given by:

$$\hat{H}_{Zeeman} = \mu_B \mathbf{S} \bar{\mathbf{g_L}} \boldsymbol{B} \tag{2.16}$$

2.2 Effective Hamiltonian model

Dimensions and computational time in the full model

The Hamiltonian described so far is a model that allows to obtain an optimally accurate description of the system, but the Hilbert space in which it operates can assume considerable dimensions and greatly increases the computation time. In fact, the dimension of the Hilbert space depends on the value of the total angular momentum of the ions that make up the molecule, and the greater this value, the greater the number of ions and the greater will be the dimension of the space.

In particular, the molecule under study is made of 3 ions of Dy of total angular momentum $S = 15/2$; each ion will therefore have a Hilbert space dimension equal to:

$$dim(H_{Dy}) = 2S + 1 = 16$$

Therefore, the total dimension of the molecule, given by the number of all the possible combinations of the spins of the Dy ions, will be given by:

$$dim(H_{3Dy}) = dim(H_{3Dy})^3 = 16 \cdot 16 \cdot 16 = 4096$$

Consequently a lot of computational time (up to days) is needed to perform fits and simulations within this model.

Effective model of single ion(s)

One possibility to considerably increase the speed of calculation and still obtain satisfactory results, is to use an effective Hamiltonian model, which allows the dimensions of the Hilbert space to be reduced without jeopardize the final results too much. In this respect, one can consider the approximation of high anisotropy, i.e. with a big anisotropy constant D. This makes it possible to obtain, for a single ion, an energy spectrum characterised by a parabolic pattern as a function of the spin of the ion, as can be expected from the Hamiltonian term $\hat{\mathbf{S}}_\mathbf{i} D \hat{\mathbf{S}}_\mathbf{i}$. An example plot for the Dy ion is shown in the left hand side of figure 2.3.
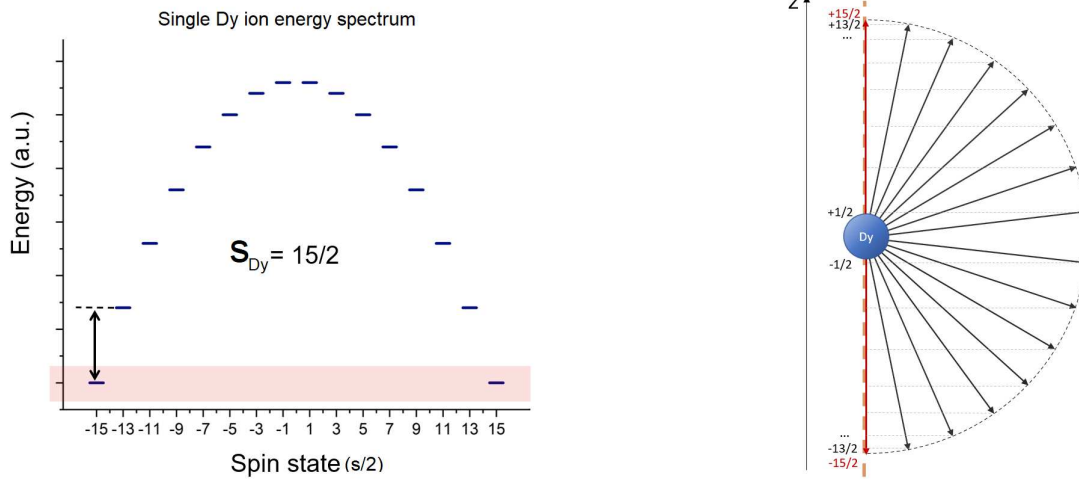

Figure 2.3: Energy spectra (on the left) and spin projection on the anisotropy axes (on the right) of a single Dy ions with a strong anisotropy component directed along the z axes.

One can immediately recognise that the ground state turns out to be occupied by the spin states $S = \pm 15/2$, while in the subsequent energy levels one finds the states $S = \pm 13/2$, $S = \pm 11/2$ and so on, where the z axis of the reference system has been made to coincide with the main anisotropy axis. Consequently, given the large value of anisotropy and, in this case, the absence of Heisenberg coupling, it can be expected that the ion´s spin tends to align with the anisotropy axis, minimising its energy, while possible inclinations between spin and anisotropy axis end up in the higher energy levels. It can then be seen that the ground state is doubly degenerate, including both spin possibilities $S = +15/2$ and $S = -15/2$, which turn out to be perfectly symmetrical.

At very low temperatures, then, used in experiments, the system can be expected to be in the ground state, while the other states have extremely low probabilities of being occupied, also given the usually large energy gap between the ground state and excited ones, due to the huge anisotropy value considered. Hence the idea of neglecting the high-energy states and focusing on the low energy ones, in which spins can only take on two values, namely $S = +15/2$ and $S = -15/2$, aligned with the anisotropy axis. In this new binary system, therefore, the modulus of the spin vector turns out to be only a multiplicative constant, while the physics of the ion can be described with a simpler $\tau = \pm 1/2$ spin system.

Even in the case of a system made up of several ions, in the absence of interactions between them, it is possible to choose the reference system locally, so as to align, as just discussed,

the z axis of each system with the relative anisotropy axis, and to describe the total angular momentum in each of these systems as a spin of $\tau = \pm 1/2$. See figure 2.4.
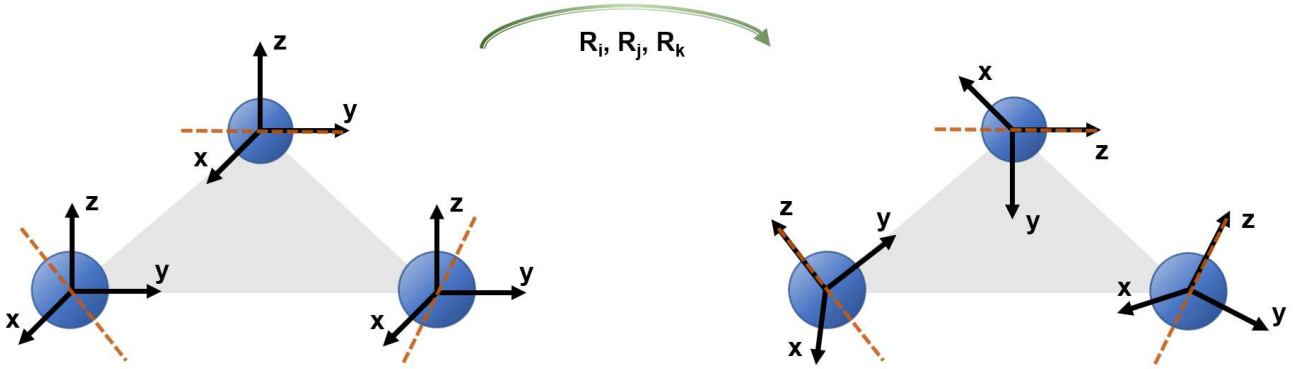

Figure 2.4: Basic idea of the effective model: local rotation of the Cartesian frame of reference aligning each z axis with the main anisotropy axis of the relative ion. The rotation is performed through a rotational matrix $\mathbf{R}_i$, different for each ion.

Mathematically then, the local rotation can be seen as the inclusion of an identity in the Hamiltonian term in the form of a product between two rotation matrices. As a consequence, this will lead the anisotropy matrix to be diagonal; in formulae:

$$\boldsymbol{S}_i \boldsymbol{D}_i \boldsymbol{S}_i = \boldsymbol{S}_i \boldsymbol{R}_i^T \boldsymbol{R}_i \boldsymbol{D}_i \boldsymbol{R}_i^T \boldsymbol{R}_i \boldsymbol{S}_i = \boldsymbol{S}_i' \boldsymbol{R}_i \boldsymbol{D}_i \boldsymbol{R}_i^T \boldsymbol{S}_i' = 15 \cdot 15 \cdot \boldsymbol{\tau}_i \boldsymbol{D}_i' \boldsymbol{\tau}_i = 225 \boldsymbol{\tau}_i \boldsymbol{D}_i' \boldsymbol{\tau}_i \qquad (2.17)$$

where we used the fact that in this binary system the spin can assume only the values $\pm 15/2$, so it is possible to write $S = \pm 15/2 = 15\tau = \pm 1/2 \cdot 15$, and where we defined the rotated anisotropy matrix $\boldsymbol{D}_i'$ as:

$$\boldsymbol{D}_i = \begin{pmatrix} D_{xx} & D_{xy} & D_{xz} \\ D_{yx} & D_{yy} & D_{yz} \\ D_{zx} & D_{zy} & D_{zz} \end{pmatrix} \qquad \Rightarrow \qquad \boldsymbol{D}_i' = \boldsymbol{R}_i \boldsymbol{D}_i \boldsymbol{R}_i^T = \begin{pmatrix} D_{xx}' & 0 & 0 \\ 0 & D_{yy}' & 0 \\ 0 & 0 & D_{zz}' \end{pmatrix} \qquad (2.18)$$

Including couplings

So far, the model described is correct in the ground state, as each ion is isolated, and the choice of reference frame does not change the physics of the system. However, we are interested in the study of a molecule in which Heisenberg interactions between the spins also appear, and we can therefore show how the effective model is also applicable in this case, but introducing a small approximation. This will consist of neglecting any inclinations of the spin vectors with respect to their respective axes of anisotropy, and thus thinking of them as parallel. This approximation will then be all the better as the anisotropy value is dominant with respect to the coupling value (high anisotropy approximation).

In our framework, the tensor $\mathbf{J}$ of the Heisenberg coupling is isotropic in the initial reference system (left-hand drawing in figure 2.4), and can therefore be represented as a diagonal matrix; the introduction of local rotations, however, as done above, will lead to the appearance of off-diagonal terms. Approximating the spin as parallel to the z axis, however, it is possible to neglect all components of the tensor that provide contributions along x or y, and, consequently, it will be sufficient to include only the J_{zz} term in the calculation. Mathematically we have:

$$\boldsymbol{S}_i \boldsymbol{J}_{ij} \boldsymbol{S}_j = \boldsymbol{S}_i \boldsymbol{R}_i^T \boldsymbol{R}_i \boldsymbol{J}_{ij} \boldsymbol{R}_j^T \boldsymbol{R}_j \boldsymbol{S}_j = \boldsymbol{S}_i' \boldsymbol{R}_i \boldsymbol{J}_{ij} \boldsymbol{R}_j^T \boldsymbol{S}_j' = 15 \cdot 15 \cdot \boldsymbol{\tau}_i \boldsymbol{J}_{ij}' \boldsymbol{\tau}_j = 225 \boldsymbol{\tau}_i \boldsymbol{J}_{ij}' \boldsymbol{\tau}_j \qquad (2.19)$$

Where the matrix $\boldsymbol{J}_{ij}'$ can be approximated as:

$$\boldsymbol{J}_{ij}' = \boldsymbol{R}_i \boldsymbol{J}_{ij} \boldsymbol{R}_j^T = J \boldsymbol{R}_i \mathbb{1} \boldsymbol{R}_j^T \simeq J \begin{pmatrix} 0 & 0 & 0 \\ 0 & 0 & 0 \\ 0 & 0 & (\boldsymbol{R}_i \boldsymbol{R}_j^T)_{zz} \end{pmatrix} \qquad (2.20)$$

Zeeman term

Similarly to what have been done for anisotropy and coupling, the same reasoning can be applied to the Zeeman term, in which the Landé factor appears in the form of an isotropic tensor. We can so apply the same approximation made for z component, along which the spins in our model are aligned, and neglect what happens along x and y. We thus have:

$$\boldsymbol{S}_i g \boldsymbol{B} = \boldsymbol{S}_i \boldsymbol{R}_i^T \boldsymbol{R}_i g \boldsymbol{B} = \boldsymbol{S}_i' \boldsymbol{R}_i g \boldsymbol{B} = 15 \boldsymbol{\tau}_i g' \boldsymbol{B} \qquad (2.21)$$

where $\boldsymbol{g}'$ can be approximated as:

$$\boldsymbol{g}' = \boldsymbol{R}_i g = g \boldsymbol{R}_i \mathbb{1} \simeq g \begin{pmatrix} 0 & 0 & R_{xz} \\ 0 & 0 & R_{yz} \\ 0 & 0 & R_{zz} \end{pmatrix} \qquad (2.22)$$

2.3   Magnetization and Susceptibility

Magnetization

By applying the Hamiltonian operator described so far to the eigenfunctions of the system, it is possible to derive the eigenvalues of energy $E_1, E_2, ... E_n$, where n is the dimension of the Hilbert space, with $n = 4096$ in the case of the 3Dy molecule. Using the eigenvalues, it is then possible to calculate the system's partition function, given by:

$$Z(T, B) = \sum_n e^{-\beta E_n} \qquad (2.23)$$

where $\beta = \frac{1}{k_B T}$ and k_B is the Boltzmann constant.

Thus, by calculating the free energy of the system as $F = -k_B T \ln(Z)$, one can define the magnetization as the response of the free energy to small variations of an externally applied magnetic field **B**. In formulas:

$$\mathbf{M}(\mathbf{B}) = -\frac{\partial F}{\partial \mathbf{B}} = k_B T \frac{\partial (\ln(Z))}{\partial \mathbf{B}} = k_B T \frac{1}{Z} \frac{\partial Z}{\partial \mathbf{B}} \qquad (2.24)$$

Therefore, in principle, the calculation of the magnetization follows directly from the diagonalisation of the Hamiltonian, with which the energy eigenvalues are derived.

As can be seen from the definition, the magnetization has a vector nature in this case, depending directly on the magnetic field vector. In most experimental cases, however, such as the one considered in the next chapter, the sample analysed is in the form of a powder and not a perfectly aligned crystal, so the molecules will be found randomly oriented in space. The magnetization measured will therefore be a sum of all the possible contributions, and similarly it can be seen as

a sum of the magnetic fields acting in various directions on the molecule. This type of observable is called *Powder magnetization.*

Analytically, then, it will be nothing more than a mean value of all the magnetizations throughout the solid angle, and can be calculated as:

$$M_{Powder}(B,T) = \frac{\int_0^{2\pi} d\phi \int_0^\pi d\theta \mathbf{M}(\mathbf{B},T,\theta,\phi)\sin(\theta)}{\int_0^{2\pi} d\phi \int_0^\pi d\theta \sin(\theta)} \tag{2.25}$$

Numerically, the integral can be calculated as the sum of contributions in phase space, using, for example, the *Romberg* method [15]; in this case, the number of points required for integration will be:

$$N(\theta) = N(\phi) = 2^k + 1 = 1,3,9,17,33... \tag{2.26}$$

with k an integer number. Various tests have shown that optimal values for sufficiently accurate magnetization calculations are $N = 17$ or $N = 33$.

As an example, figure 2.5 shows some magnetization curves as a function of the magnetic field at different temperatures for an antiferromagnetic system. Given the possibility of seeing the magnetization as the thermodynamic expectation value of the total magnetic moment, is clear the asymptotic trend for high magnetic fields, in which all spins tend to align with the direction of the field. While higher temperatures will lead to less rapid increases in magnetization, leaving more opportunity for spin orientation given the higher energy of the system. More details will be described later in the next chapter.
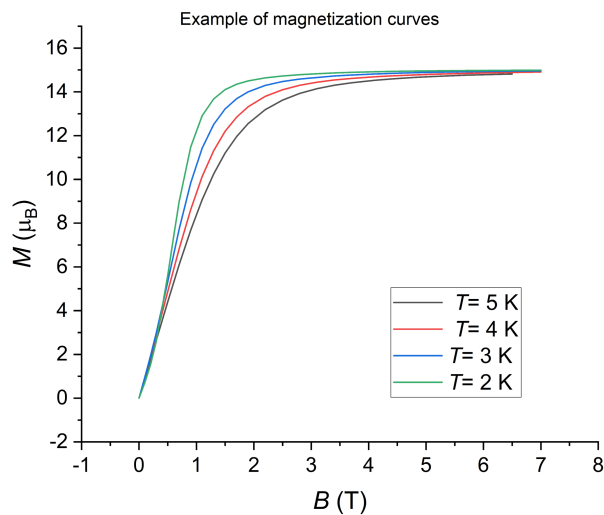

Figure 2.5: Example of magnetization curves as a function of the magnetic field for different temperatures in a antiferromagnetic system. In the asymptotic region, for high enough magnetic fields, all the spins tend to align to the external applied field. High temperatures lead to a lower increase of the magnetization, since more energy is present in the system and the spins have more freedom of motion.

Susceptibility

Similarly to the magnetization, the susceptibility can also be calculated from the diagonalisation result of the Hamiltonian, via the partition function Z and the free energy F. In fact, the

susceptibility quantifies the change in the magnetization for small changes of the magnetic field, and can thus be written as:

$$\chi_{i,j} = \frac{\partial \mathbf{M}_i}{\partial \mathbf{B}_j} = -\frac{\partial^2 F}{\partial B_i \partial B_j} = \frac{1}{\beta} \frac{\partial^2 \ln(Z)}{\partial B_i \partial B_j} \tag{2.27}$$

so χ is a second-rank tensor. Here too, experimentally it is often measured a powder susceptibility, and, consequently, it is required an average value of the quantity just described. By choosing the reference system appropriately, it is possible to diagonalise the susceptibility tensor, and thus calculate the mean value simply as $\chi = \frac{1}{3}(\chi_{xx} + \chi_{yy} + \chi_{zz})$.

Often, the susceptibility values are represented as a product with the temperature, thus in a $\chi T(T)$ graph, in order to show the behaviour of the susceptibility at low temperatures. Furthermore, in the case of a paramagnetic system, the *Curie law* applies, according to which the product of susceptibility and temperature results in a constant, called the *Curie constant*. In formulae:

$$\chi T = C \tag{2.28}$$

with $C = \frac{\mu_B g^2}{3k_B} S(S+1) = const.$

A similar relationship exists for systems that can only be described by means of Heisenberg couplings, without the presence of anisotropy, since the set of spins can ideally be replaced by a single effective spin that will obey Curie's relationship. By introducing an anisotropy term, however, the product of susceptibility and temperature will no longer be constant, and the behaviour will depend on the system considered. In the case of antiferromagnetic systems, for example, the presence of anisotropy will lead to a rapid decrease in susceptibility for low temperatures. An example of a susceptibility graph is shown in figure 2.6, where the temperature is varied from 0 to 300°C, and the same vertical scale allows to appreciate the scaling of the susceptibility when multiplied by the temperature.
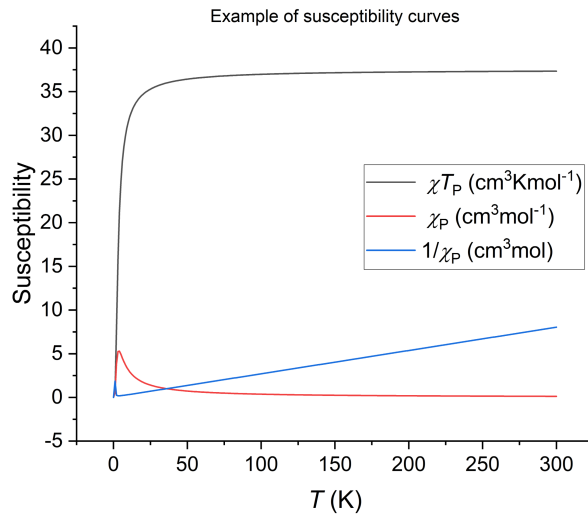

Figure 2.6: Example of susceptibility curves as a function of the temperature in a antiferromagnetic system.

In what follows, mainly χT graphs will be analysed, so without any risk of confusion, the term "susceptibility" will also be used to refer to the product between the usual susceptibility and temperature.

2.4 Toroidicity

The toroidicity of the molecule is an indication of how much the spins are oriented in a vortex way, but we need a quantitative way to describe it, so a variable that allows to quantify the toroidicity of the molecule itself. We can consider the definition proposed in [16], in which the observable that describes the toroidicity is called toroidal moment ($\boldsymbol{t}$), and it is given by the relation:

$$\hat{\boldsymbol{t}} = \frac{g\mu_B}{2} \sum_{i=1,2,3} \boldsymbol{r_i} \times \hat{\boldsymbol{S_i}} \tag{2.29a}$$

It is therefore a quantum operator, and to obtain some physical values, it is necessary to apply it to an eigenfunction to find, for example, its mean value. The toroidal moment is then position-dependent, so the coordinate system should be chosen in a proper way, and we will discuss this in the following.

Spin operators and their average value

Once the the parameter to quantitatively describe the toroidicity is defined, it is necessary to explicitly point out the calculation method used to obtain the numerical values. To do so we can use the possibility of the *owHc* program to evaluate the matrix elements of the spin operators $\hat{S}_+$, $\hat{S}_-$ and $\hat{S}_z$ computed as:

$$\langle m| \, \hat{S}_{+,-,z} \, |n\rangle \tag{2.30}$$

between two states $|m\rangle$ and $|n\rangle$.

The result is straightforward in the case of a non-degenerate subspace, i.e. of unitary dimension, where $E_n \neq E_m$ for each $m \neq n$, and the only matrix element present is the average value of each operator in the eigenspace considered, thus:

$$\langle m| \, \hat{S}_{+,-,z} \, |m\rangle$$

The situation is more complicated in the case of degeneracy, i.e. a sub-space composed of multiple eigenspaces corresponding to the same energy eigenvalue. In this case, the dimension of the sub-space is greater than 1, and a diagonalization of the matrix describing the sub-space is necessary in order to obtain the eigenvalues of the spin operators. In matrix notation, in the case of a subspace of degeneracy 2 and initial eigenvectors $|m'\rangle$ and $|n'\rangle$ for a generic spin operator $\hat{S}$, we have:

$$\begin{pmatrix} \langle m'| \, \hat{S} \, |m'\rangle & \langle m'| \, \hat{S} \, |n'\rangle \\ \langle n'| \, \hat{S} \, |m'\rangle & \langle n'| \, \hat{S} \, |n'\rangle \end{pmatrix} \xrightarrow[\text{Diagonalization}]{} \begin{pmatrix} \langle m| \, \hat{S} \, |m\rangle & 0 \\ 0 & \langle n| \, \hat{S} \, |n\rangle \end{pmatrix}$$

Once the mean values of the spin operators $\hat{S}_{z,+,-}$ in each of the states under analysis have been obtained, it is straightforward to find the mean values of the spin components, through the relations:

$$\hat{S}_x = \frac{1}{2} \left(\hat{S}_+ + \hat{S}_- \right) \tag{2.31a}$$

$$\hat{S}_y = \frac{1}{2i} \left(\hat{S}_+ - \hat{S}_- \right) \tag{2.31b}$$

Toroidal moment operator

Using the mean values of the coordinates of the spin vectors, it is then possible to calculate the toroidal moment directly by applying the definition shown in the equation 2.29. In fact, calling **t** the toroidal moment vector, this will be computed as the average value of the relative toroidal moment operator $\hat{\mathbf{t}}$ in a state $|n\rangle$; this reads:

$$
\begin{aligned}
\mathbf{t} = \langle n| \,\hat{\mathbf{t}}\, |n\rangle &= \frac{g\mu_B}{2} \sum_{\alpha=1}^{3} \mathbf{r}_\alpha \times \langle n| \,\hat{\mathbf{S}}_\alpha\, |n\rangle = \frac{g\mu_B}{2} \, \langle n| \, \mathbf{r}_1 \times \hat{\mathbf{S}}_1 + \mathbf{r}_2 \times \hat{\mathbf{S}}_2 + \mathbf{r}_3 \times \hat{\mathbf{S}}_3 \, |n\rangle = \\
&= \frac{g\mu_B}{2} (\mathbf{r}_1 \times \langle n| \,\hat{\mathbf{S}}_1\, |n\rangle + \mathbf{r}_2 \times \langle n| \,\hat{\mathbf{S}}_2\, |n\rangle + \mathbf{r}_3 \times \langle n| \,\hat{\mathbf{S}}_3\, |n\rangle)
\end{aligned}
\tag{2.32}
$$

We then ended up with a sum of vector products in which it appears the average value of the spin operator in the state $|n\rangle$ for each ion, namely:

$$
\langle n| \,\hat{\mathbf{S}}\, |n\rangle = \langle n| \begin{pmatrix} \hat{S}_x \\ \hat{S}_y \\ \hat{S}_z \end{pmatrix} |n\rangle
\tag{2.33}
$$

which are evaluated as discussed above.

2.5   Neutron scattering

[17][18][19]

Neutron scattering techniques are of fundamental importance in studying the properties of the materials at the atomic scale, and combined with x-ray scattering they allow to cover a big range of energies and momentum transfer for the experimental analysis. The usefulness of neutrons in scattering processes derives from their physical properties (shown in table 2.1). In particular there are several noteworthy advantages due to the fact that their electric charge is zero, so they are not affected by the charge of the orbital electrons. Neutrons can so interact with nuclei through the strong interaction, which occurs only at very low distances and so the resulting scattering effect is weak. On the contrary the interaction between the neutron magnetic moment and possible magnetic ions in the sample to analyze can give good scattering signals that allow to investigate the properties of the material.

mass	$m = 1.675 \times 10^{-27}\, kg$
charge	0
spin	$1/2$
magnetic dipole moment	$\mu_n = -1.913\, \mu_N$

Table 2.1: Neutron physical properties

2.5.1   Energy and velocity

The de Broglie wavelength of a neutron with a certain velocity v is given by

$$
\lambda = \frac{h}{mv}
\tag{2.34}
$$

and so for reasonable values of the velocity the wavelength is comparable to the interatomic distances of solid and liquid materials.

The velocity of the neutron is directly related to their energy, and so to their production. There are in fact two main ways of producing neutron: the first one uses the scattering between another neutron and a Uranium core, and during the fission process three other neutrons are released, one of which is used for another fission reaction while the other two can be collected and used for the scattering experiments. In this way a continuous flux of neutron can be produced, and this method is used for instance at the Institut Laue Langevin in Grenoble.

Otherwise it is possible to obtain neutrons using a spallation process, in which a proton is accelerated with a linear accelerator to energies up to $1\,GeV$ and collides with a heavy metal target (Hg, Pb, Tg...) that, because of the excitation of the nuclei, releases several neutron.

In both cases the neutrons carry energy of $MeVs$ while for condense matter purpose energies of the order of $meVs$ are needed, therefore different moderating materials (such as water, heavy water or graphite) at a different temperature are used to decrease the energy (temperature) of the neutrons to the desired value. The neutrons emerging from the reactor have so a velocity spectrum that follows a Maxwell distribution (figure 2.7) with the temperature T of the moderator, so the probability of having a neutron with velocity between v and $v + dv$ reads:

$$P(v)dv = 4\pi \left(\frac{m}{2\pi k_b T} \right)^{3/2} v^2 \cdot exp(-\frac{1}{2}\frac{mv^2}{k_b T})dv \tag{2.35}$$
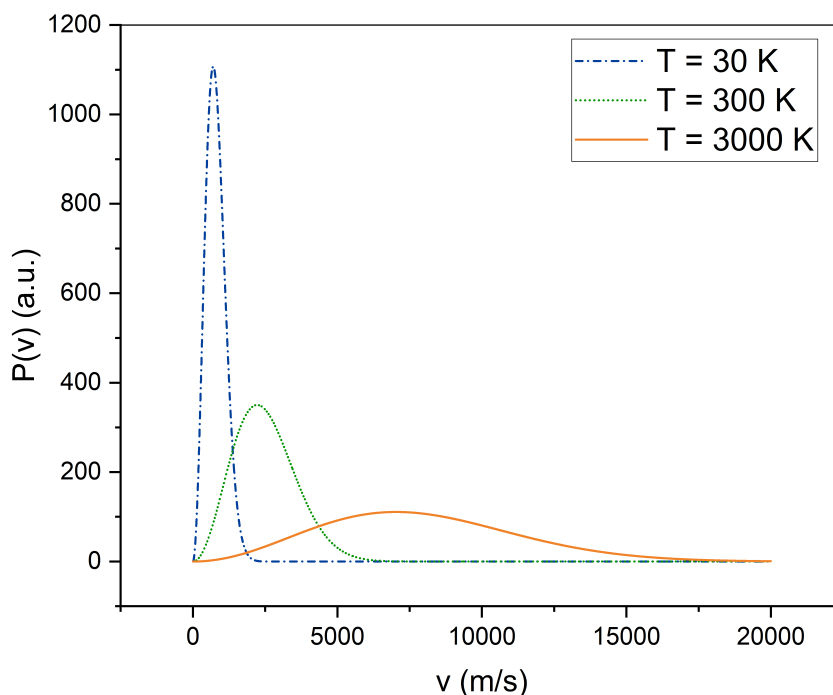
with a maximum for $v = \sqrt{2k_b T/m}$.

Figure 2.7: Maxwell distribution of neutrons for different temperatures.

Defining then the magnitude of the wave-vector $\mathbf{k}$ as:

$$k = \frac{2\pi}{\lambda} \tag{2.36}$$

and the momentum of the neutron as:

$$\mathbf{p} = \hbar\mathbf{k} \tag{2.37}$$

the maximum of the velocity probability corresponds to a kinetic energy of

$$E = \frac{1}{2}mv^2 = k_bT = \frac{\hbar^2 k^2}{2m} = h\upsilon \tag{2.38}$$

Based on these relationships, one can then classify neutrons according to their characteristics into cold, thermal and hot neutrons, as summarized in table 2.2.

	$E(meV)$	$T(K)$	$\lambda(10^{-10}m)$
Cold	0.1-10	1-120	30-3
Thermal	5-100	60-1000	4-1
Hot	100-500	1000-6000	1-0.4

Table 2.2: Neutron classification based on their energy, temperature or wavelength.

Therefore, in addition to having wavelengths comparable to the distances between atoms, also the energies turn out to be of the same order of elementary excitations in matter. So, during the scattering, the energy exchanged is comparable to the initial one, and accurate pieces of information can be obtained about not only about the "static" structure of the material, but also on the dynamic properties.

2.5.2   Interaction with matter

Because of the null charge of the neutrons, they weakly interact with matter and this leads to two main advantages: to reduce the damage due to radiations in the studied sample and to increase the penetration length, thus enabling investigation of bulk material properties.

We can distinguish three main modes of interaction between a neutron and a material, namely absorption, refraction and scattering.

- In the absorption process the beam of neutrons does not change in direction, but its intensity is decreased exponentially with the law $I(d) = I_0 e^{-\mu d}$, where I_0 is the initial intensity, d is the distance traveled in the sample and μ is a coefficient depending on the material. Some neutrons are so absorbed by the nucleus of the atoms of the material which can then emit radiations like α, β, etc.

- The refraction phenomenons can be explained in analogy to classical optics but with a proper refractive index which depends on the wavelength λ of the incident neutrons, on the mean value $\bar{b}$ of the scattering lengths of the nuclei and on the volumetric density ρ of nuclei in the sample: $n_r = 1 - \frac{1}{2\pi}\rho\bar{b}\lambda^2$.

- The operation of scattering is very similar to that of most radiation in materials and will be described in more details in the following subsections.

Scattering cross section

We are interested in the interaction between a beam of neutrons (considered for simplicity a as a white beam, so with neutrons of the same wavelength) and a *scattering system*, i.e. any sample made as a collection of atoms. In the hypothesis of a white incident beam we can describe it quantum-mechanically as a planar wave of wave-vector $\mathbf{k}_i$, while from diffraction theory it comes up that the wave description of diffracted beam will be spherically symmetric, and with a new wave-vector $\mathbf{k}_f$. So the incident and scattered neutrons will be in the states:

$$\psi_i = e^{ik_i z} \qquad \psi_f = -\frac{b}{r}e^{ik_i z} \tag{2.39}$$

where b is known as *scattering length*. We can call then λ_i and λ_f the initial and final states of the target system, made of nucleus N in positions $\mathbf{R}_1, ..., \mathbf{R}_N$.

The properties of the scattering are encapsulated in the *cross section*, quantity that describes the number of particles scattered in a certain region and it has the dimensions of an area. The cross section can be actually computed starting from another similar quantity called *partial differential cross section* which measures the number of neutrons scattered per second into a solid angle $d\Omega = sin\theta d\theta d\phi$ with final energies between E_f and $E_f + dE_f$ and looks like:

$$\frac{d^2\sigma}{d\Omega dE_f} \tag{2.40}$$

The differential cross section can so be thought as a sum over all the possible processes that ends with a state λ_f and a wave-vector $\mathbf{k}_f$ in the direction θ, ω; using then the *Fermi´s golden rule* to evaluate the transition rate from the state $\langle \lambda_i, \lambda_i |$ to the state $\langle \lambda_f, \lambda_f |$ and considering an energy conservation condition, it is possible to arrive to an explicit expression of the differential cross section like:

$$\frac{d^2\sigma}{d\Omega dE_f} = \frac{k_f}{k_i} \left(\frac{m}{2\pi\hbar} \right)^2 | \langle \mathbf{k}_f \lambda_f | V | \mathbf{k}_i \lambda_i \rangle | \delta(E_{\lambda_i} - E_{\lambda_f} + E_i - E_f) \tag{2.41}$$

where the matrix element deriving from the Fermi´s golden rule can be written as:

$$| \langle \mathbf{k}_f \lambda_f | V | \mathbf{k}_i \lambda_i \rangle | = \frac{\Phi m}{\hbar k} \int exp(-i\mathbf{k}_f \cdot \mathbf{r}) \zeta_{\lambda_f}^* V exp(i\mathbf{k}_i \cdot \mathbf{r}) \zeta_{\lambda_i} d\mathbf{R} d\mathbf{r} \tag{2.42}$$

with Φ the incident flux of neutron, ζ_{λ_i} and ζ_{λ_f} the initial and final states of the target system, $\mathbf{r}$ the vector position of the neutron and V the scattering potential. To obtain an explicit result it is necessary then to choose an expression for the scattering potential V, which can be thought as a sum of two main contributions: one that describes the scattering due to the strong nuclear force and one due to the magnetic interactions. The two cases will be treated in the following.

Strong nuclear force potential

The interactions governed by the strong nuclear force are significant only if the distance between the incoming neutron and one atom of the lattice is small, and we can therefore associate this effect with a *short range potential* which can be written as:

$$V(\mathbf{r}) = a\delta(\mathbf{r}) \tag{2.43}$$

where we considered the atom in the origin, therefore $\mathbf{R} = 0$. $\delta(\mathbf{r})$ is the Dirac delta, namely $\int_{space} \delta(\mathbf{r}) d\mathbf{r} = 1$, while a is a real constant that can be determined inserting equation 2.43 in 2.46 and 2.42 and comparing the result with the scattering cross section with a single nucleus computed from the flux and velocity of the neutrons. It is then possible to find that $a = \frac{2\pi\hbar^2}{m} b$ and therefore the scattering potential becomes:

$$V(\mathbf{r}) = \frac{2\pi\hbar^2}{m} b\delta(\mathbf{r}) \tag{2.44}$$

The potential thus obtained is an approximation of the interaction potential between neutron and nuclei, and it is called *Fermi pseudopotential*; calling $\mathbf{Q} = \mathbf{k}_f - \mathbf{k}_i$ the *scattering vector* (or *momentum transfer*) it is possible to write the Fourier transform of this potential as

$$V(\mathbf{Q}) = \frac{2\pi\hbar^2}{m} b e^{i\mathbf{Q} \cdot \mathbf{r}} \tag{2.45}$$

and this allows to find an expression for the differential cross section that looks like:

$$\frac{d^2\sigma}{d\Omega dE_f} = \frac{\sigma}{4\pi}\frac{k_f}{k_i}NS(\mathbf{Q},\omega) \tag{2.46}$$

where the function $S(\mathbf{Q},\omega)$ is called *scattering function*, and contains all the physics of the process and the characteristics of the material under study, and it´s simply given by the Fourier transform of the pair correlation function $G(\mathbf{r},t)$.

Magnetic potential

As said from the beginning, the magnetic properties of magnetic ions are mainly due to unpaired electrons, and therefore one can expect a considerable interaction between the neutrons (particle with spin 1/2) and the magnetic ions of the sample.

To investigate this effect we can start by defining the *magnetic dipole moment operator* of the neutron, given by:

$$\boldsymbol{\mu}_n = \gamma\mu_N\boldsymbol{\sigma} \tag{2.47}$$

where $\mu_N = \frac{e\hbar}{2m_p} \simeq 5.051 \cdot 10^{27} J/T$ is the *nuclear magneton*, $\gamma = -1.913$ is the gyromagnetic ratio, and $\boldsymbol{\sigma}$ is the Pauli spin operator.

The magnetic interactions of a neutron can thus be summarized as the interaction between its magnetic dipole moment and an external magnetic field $\boldsymbol{B}$, namely:

$$U_m = -\boldsymbol{\mu}_n \cdot \boldsymbol{B} = -\gamma\mu_N\boldsymbol{\sigma} \cdot \boldsymbol{B} \tag{2.48}$$

The magnetic field $\boldsymbol{B}$ will then be generated by the unpaired electron of the nucleus, and will be made of two contributions, one due to the magnetic moment (spin) of the electron itself ($\boldsymbol{B}_s$) and the other due to its orbital momentum ($\boldsymbol{B}_L$). The first one can be written as the curl of a vector potential $\boldsymbol{A}$ calculated with the magnetic moment $\boldsymbol{\mu}_e$ of the electron, while the second is derived directly from the law of Biot and Savart. The complete magnetic field can be written so as:

$$\mathbf{B} = \mathbf{B}_s + \mathbf{B}_L = \frac{\mu_0}{4\pi}\left[\boldsymbol{\nabla} \times \left(\frac{\boldsymbol{\mu_e} \times \mathbf{R}}{R^3}\right) - \frac{2\mu_B}{\hbar}\frac{\mathbf{p} \times \mathbf{R}}{R^3}\right] \tag{2.49}$$

Therefore, inserting the field just computed in relation 2.48, the magnetic interaction potential will look like:

$$U_m = -\frac{\mu_0}{2\pi}\gamma\mu_N\mu_B\boldsymbol{\sigma} \cdot \left[\boldsymbol{\nabla} \times \left(\frac{\boldsymbol{s} \times \mathbf{R}}{R^3}\right) + \frac{1}{\hbar}\frac{\mathbf{p} \times \mathbf{R}}{R^3}\right] \tag{2.50}$$

where we used the definition of the electron magnetic moment given by $\boldsymbol{\mu}_e = \gamma\mu_B\boldsymbol{s}$ with $\boldsymbol{s}$ the electron spin operator.

As we did in the previous section we can so take the Fourier transform of the magnetic potential, which will be a function of the scattering vector $\boldsymbol{Q}$ and can be written as:

$$U_m(\boldsymbol{Q}) = \frac{2\pi\hbar^2}{m}\sum_j p_j F_j(\boldsymbol{Q})\delta(\boldsymbol{r} - \boldsymbol{r}_j(t))) \tag{2.51}$$

where the sum is performed over all the atoms of the systems in positions $\boldsymbol{r}_j$ and the functions $F_j(\boldsymbol{Q})$ are the dimensionless magnetic form factor of the different atoms, so the Fourier transform of the electric charge distribution in space. Furthermore, the $p_j s$ are the magnetic scattering length of the electrons in the different atoms, and they have a analytical expression

more complicated than the nuclear scattering length b since we are dealing now with a non-central force. However the magnitude of p and b are comparable, so the magnetic and nuclear scattering make a similar contribution to the neutron-atom interaction.

Having a formula for the interaction potential, it is again possible to derive the differential cross section inserting equation 2.51 in equation 2.46 and this, indexing with α and β the Cartesian coordinates x, y and z, leads to the expression[2]:

$$\frac{d^2\sigma}{d\Omega d\omega} = \frac{\gamma e^2}{m_e c^2} \frac{k_f}{k_i} \sum_{m,n} \frac{e^{-\beta E_n}}{Z(T)} I_{m,n}(\mathbf{Q}) \delta\left(\omega - \frac{E_m - E_n}{\hbar}\right) \tag{2.52}$$

with

$$I_{m,n}(\mathbf{Q}) = \sum_{i,j} F_i(Q) F_j(Q) e^{i\mathbf{Q}\cdot\mathbf{R}_{i,j}} \sum_{\alpha,\beta} \left(\delta_{\alpha,\beta} - \frac{Q_\alpha Q_\beta}{Q^2}\right) \langle n| \widehat{S}_{i,\alpha} |m\rangle \langle m| \widehat{S}_{j,\beta} |n\rangle \tag{2.53}$$

where the sum is performed over the different magnetic ions and $I^{i,j}_{\lambda_i,\lambda_f}(Q)$ is a function constructed out of the Bessel functions.

The quantity $(\delta_{\alpha,\beta} - \frac{Q_\alpha Q_\beta}{Q^2})$ is called *polarization factor* and it allows the scattering only if the magnetic moment is perpendicular to the scattering vector $\boldsymbol{Q}$, otherwise no contribute is given to the differential cross section; this allows so to detect the direction of the magnetic moment by neutron scattering results. Moreover the dependency on the thermal population factor p, so the probability to observe a specific transition, is also related to the temperature of the system of ions, and so to the most probable energy eigenstates by which the system is described.

Even though it is not possible to directly observe it from this equation, it can be proven that the possible transition are characterized by a maximal spin difference between the initial and the final state of 1, which leads to the *selection rules*:

$$\Delta S = 0, \pm 1 \tag{2.54}$$
$$\Delta M = 0, \pm 1 \tag{2.55}$$

In general the result of the relation above is a complex number, in which the imaginary part should cancel out; in fact usually the imaginary part is related to the absorption of the particle in the scattering, but in this case this imaginary part come from just two sources, the exponential and the matrix elements, but in non of there is anything about neutron absorption. Only the result of interaction with the spin is included in the formula.

2.5.3 Powder and single crystal neutron scattering

Equation is the starting point for simulating neutron scattering experiments. It is therefore possible to obtain the peak intensity of a powder sample by integrating the equation over the entire solid angle $d\Omega$, eliminating the dependence on the orientation of the vector $\mathbf{Q}$. The derivation of the final formula is complicated, and the result has already been derived and implemented in a package of the code *owMag* called *owIns*. However, it is possible to obtain an analogous formula in the case of crystalline samples, and this will be derived, implemented and tested below in chapter 7.

---

[2]Computed in [20]

Chapter 3

Al_2Dy_3 molecule

3.1   Compound: description and structure

The molecule studied in this thesis is a new compound synthesised in the Institute of Inorganic Chemistry of the Karlsruhe Institute of Technology by dr. Thomas Ruppert, supervised by prof. Annie K. Powell.

It consists of a core formed by three dysprosium ions (Dy^{3+}) arranged in a triangular configuration and two aluminium ions positioned along the axis of this triangle. A multitude of other atoms, O, H, C, N, surrounds the central part of the molecule, forming what is called the *ligands structure*. This structure influences the magnetic properties of the central ions, in particular by introducing magnetic anisotropies, i.e. preferential directions in which the spins tend to align. The ligand structure is designed to give high anisotropy values, and directions of the anisotropy axes that can provide a good toroidicity to the molecule.

The scheme of the molecule, obtained through crystallographic measurements, is shown in figure 3.1, in which the complete structure of the ligands is shown (on the left) and a focus is made on the central core (on the right).

Crystallographic measurements make it possible to derive the position of the different ions of the molecule in a certain Cartesian reference system. For our purposes, however, we will only be interested in the triangle of Dy ions, so it will be convenient to rotate the reference system so that the three ions lie in the x-y plane, and one of the ions lies along the y axis. The z axis then passes approximately through the centre of the Dy triangle. A scheme of the coordinate frame and the position of the three Dy ions in it is shown in figure 3.2.

3.2   Magnetic properties

3.2.1 Dy^{3+} ions and Hilbert space dimension

As mentioned, the magnetic properties of the molecule are provided by the three triangularly arranged dysprosium ions. Each dysprosium ion makes a contribution to the total ground state magnetic moment of 15/2. A dysprosium atom can be represented in the notation:

$$[Xe]4f^{10}6s^2$$
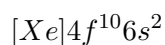
and so a Dy^{3+} ion will lose 3 of its electrons, 2 from the s orbital and 1 from the f orbital. 5 electrons will therefore remain unpaired, thus providing a spin contribution of $5 \cdot \frac{1}{2}$, i.e:
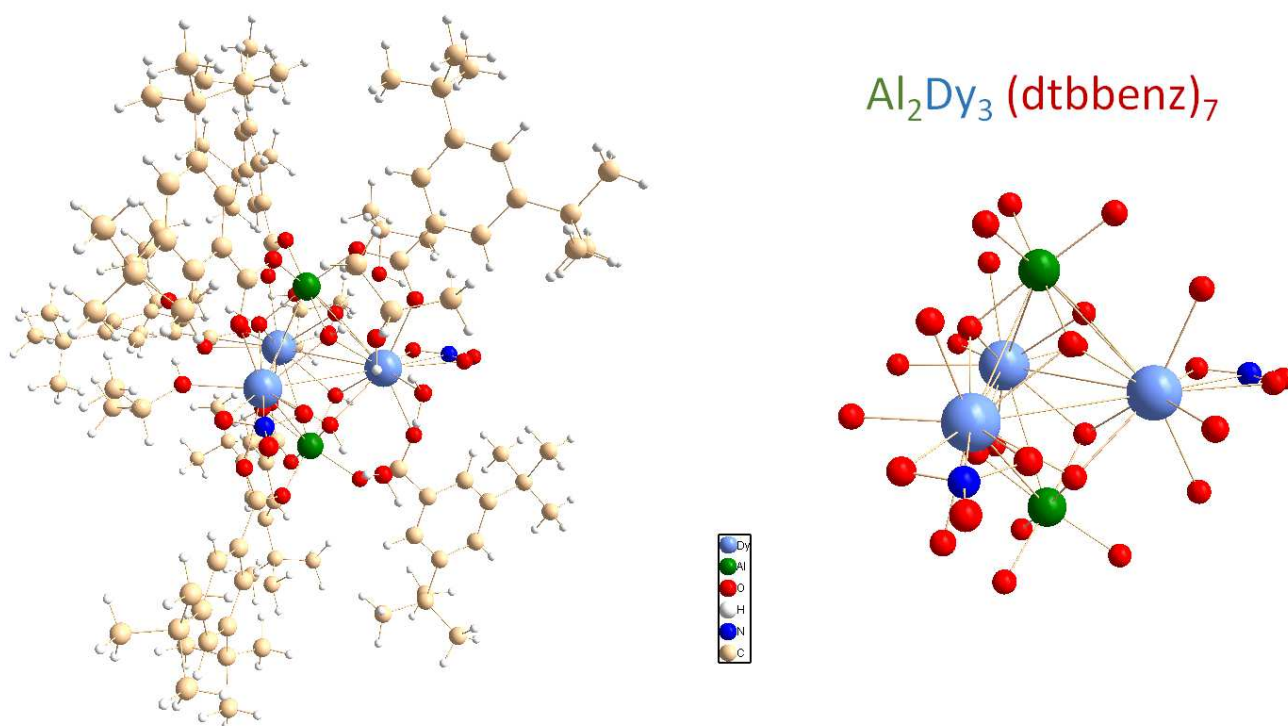
$$s_{Dy^{3+}} = \frac{5}{2}$$

Figure 3.1: Al_2Dy_3 chemical scheme of the molecule with all the surrounding ligands (on the left) and a zoom in the core of it (on the right). The main focus will be on the three Dy ions, since they are the ones that give the magnetic properties to the molecule.
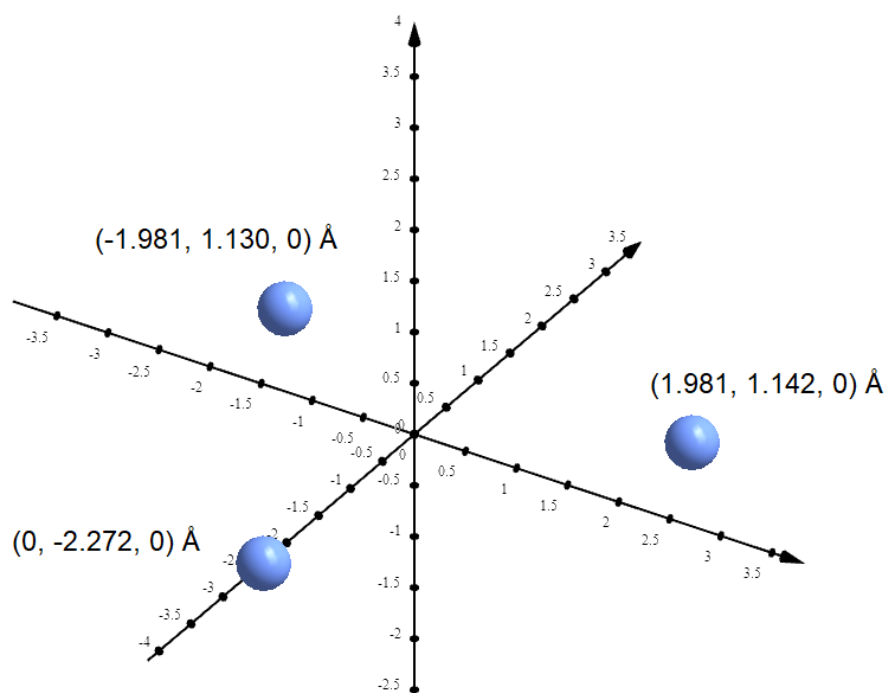

Figure 3.2: Chosen Cartesian coordinate frame for the molecule, focusing on the 3 Dy ions. The Dy triangle is lying on the $x - y$ plane, and the z axis then passes approximately through the centre of it. In the picture are shown the Cartesian coordinates of each ion obtained through crystallographic measurements and rotated within the choice of the frame of reference.

The ion´s orbital is then H type, so it will be characterised by an azimuthal quantum number equal to:

$$\ell_{Dy^{3+}} = 5$$

By the rules for the sum of angular moments, there will thus be for each dysprosium a total angular momentum equal to

$$j_{Dy^{3+}} = \frac{15}{2}$$

So the dimension of the Hilbert space for a single ion will be:

$$dim(H_{Dy^{3+}}) = 2j + 1 = 16$$

And, therefore, having 3 Dy ions, the total dimension of the Hilbert space of the molecule is:

$$dim(H_{3Dy^{3+}}) = 16^3 = 4096$$

The dimension found will also be the Hilbert space dimension of the entire molecule. In fact, the only magnetic properties are given by the Dy ions, as the two Al^{3+} ions are non-magnetic, as they do not have any unpaired electrons.

Since in our discussion we are interested in the total magnetic moment, a value that appears in the Hamiltonian described in section 2.1, we will refer to it simply by the term "spin" or "total spin".

3.2.2   Susceptibility and magnetization

After the synthesis of the molecule, some magnetic measurements were carried out. In particular, measurements of susceptibility as a function of temperature and of magnetization for different temperatures as a function of the applied external magnetic field. In particular a *superconducting quantum interference device* (SQUID) technique has been used, and the results have been plotted in figure 3.3.
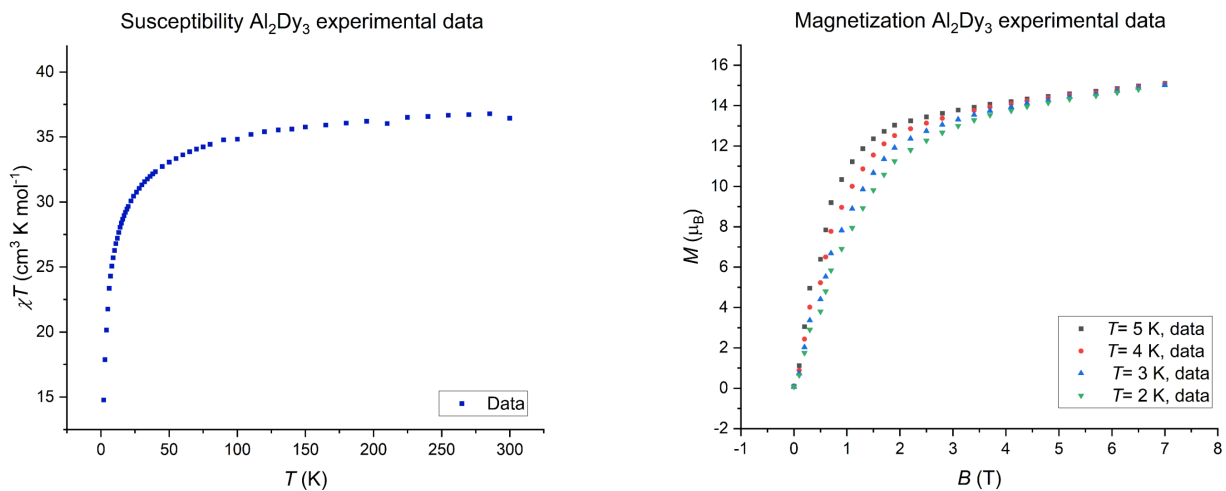

Figure 3.3: Acquired data of susceptibility χT as a function of the temperature (on the left) and magnetization M for different temperatures as a function of the magnetic field (on the right) for the Al_2Dy_3 molecule.

The room temperature susceptibility χT reaches a value of $35\, cm^3 K mol^{-1}$, but at low T, however, the susceptibility is rapidly decreasing but without vanishing completely, as it happens in [21].

The magnetization then shows an increasing trend starting with a zero value for zero magnetic field and then increasing rapidly without showing an initial transient of zero magnetization at low magnetic fields. For high magnetic fields, the sample is totally magnetised, given the asymptotic behaviour of the magnetization, which settles around a value of 15 μ_B, irrespective of the temperature at which the measurement is taken. The step in the magnetization that it is possible to see around $1\,T$ is explained by the energy level crossing, and so by a transition induced by the magnetic field between the first excited magnetic state and the ground state (see chapter 5).

The aim will then be to fit these experimental data to derive the magnetic properties of the molecule. In particular, we are interested in the orientation of the anisotropy axes of the three Dy ions, which could give direct information on the spin orientation and thus on the toroidal moment. The methodology and results of the fits will be shown in chapter 4.

Chapter 4

Fitting of experimental data

4.1 Algorithm and parameters

4.1.1 In-House program and fitting algorithm

The program used for analysing the experimental data and for the simulations that will be shown in the following chapters is a code written in C language, developed in-house and called *owMag*.

It requires a description of the molecular structure under analysis, specifying: the number of ions involved; the magnetic coupling value (J) between pairs of them; the total spin; the anisotropy values (D and E) and the orientation of the anisotropy axes via the angle triads (θ, ϕ, α); the Landé factor (g). Further details concerning the simulation can be then specified, e.g. the type of output files and their content, specific fit parameters etc. For using the effective model, then, some commands allow us to specify the angles of local rotation of the anisotropy axes, and the matrix elements to be considered and which ones to set to zero.

To simulate magnetization and susceptibility, the description of the molecule in the input file is sufficient, obviously specifying the temperature and magnetic field ranges in which to simulate the data. On the other hand, for what concerns the fits, the experimental data must also be considered and fed to the code. It is therefore possible to specify in the input file the type of data available, collected in an external text file, and its format and structure.

By populating and diagonalizing the Hamiltonian, the program can directly output the simulation results, or proceed with several simulations for different parameter values to find the one that best interpolates the data, thus performing a fit.

To perform those fits, *owMag* uses the *Levenberg–Marquardt* algorithm [15], which combines two minimisation algorithms: the gradient descent method, in which the fit parameters are updated following the steepest-descent direction, and the Gauss-Newton method, which aims at minimising the least squares function. In particular, the function to be minimised used in *owMag* is chosen to be the sum of the squares of the differences between the values to be fit (y_i^{data}) and the fit values (y_i^{sim}); in formulae:

$$\chi^2 = \sum_i^{data\,points} (y_i^{data} - y_i^{sim})^2 \tag{4.1}$$

Various choices can be made to normalise the differences shown in the equation in order to give different weights to different points on the curve. These include, for example, dividing by a

constant, by the experimental data or by the uncertainty on the experimental data. In *owMag*, the first possibility was therefore adopted, choosing this constant equal to 1, in order to assign the same weight to all the experimental points.

The standard method for the fit is therefore to proceed iteratively by minimising χ^2; hence the final result of the fit will be a configuration of values corresponding to a minimum of χ^2 in the parameter space. But, depending on the complexity of the landscape of χ^2, this minimum may be global, or only local. Therefore, the choice of the initial parameters may affect the final results, and only parameters sufficiently close to the minimum may lead to convergence to the global minimum.

To simulate susceptibility and magnetization in powder form, then, it is necessary to integrate over all possible sample orientations, as described in section 2.3. For this purpose, the *Romberg´s method*[15] for estimating definite integrals is used.

4.1.2   Choice of the fitting parameters

For the execution of the fits, it is necessary to weigh up the choice of the number and type of parameters one wants to leave free to vary. The model used to describe the physics of the system is in fact the Hamiltonian model shown in equation 2.1, in which a large number of degrees of freedom appear; these include the parameters shown in table 4.1.

$J_{1,2}$, $J_{2,3}$, $J_{3,1}$	Heisenberg couplings
D_1, D_2, D_3	Anisotropy parameters for each ion
E_1, E_2, E_3	
$theta_1$, phi_1, $alpha_1$	Anisotropy axis orientation first ion
$theta_2$, phi_2, $alpha_2$	Anisotropy axis orientation second ion
$theta_3$, phi_3, $alpha_3$	Anisotropy axis orientation third ion
g_1, g_2, g_3	Landé factor for each ion
m_{scale}	Molar mass correction
χ_0	Diamagnetic correction

Table 4.1: Possible fit parameters of the Hamiltonian model for a 3 ions system

Most of the parameters have already been described above, so particular attention can be paid to the last two parameters.

Molar mass correction m_{scale}

The crystal ((3,5-ditertbutylbenzoic acid)) synthesised containing the *3Dy* molecules and used for data collection, is unfortunately a system that allows for low accuracy regarding the purity of the crystal, and consequently on its molar mass. This is due to the crystallisation process, in which the amount of solvent (Isopropanol/Water C_3H_7OH) influences the final mass of the compound due to the possibility of exchange of some of these molecules with those constituting the sample. The normal correction of the molar mass of the system, by subtracting the molar mass of the solvent, therefore, results in values that are not extremely accurate, and this may affect the final values of the (molar) susceptibility and (molar) magnetization to be studied. To take this deviation into account, it is therefore possible to use a corrective parameter m_{scale} in the fits, with a value around 1 for corrections that are not too large, which acts by rescaling susceptibility and magnetization as:

$$\chi T = \chi T m_{scale}$$
$$M = M m_{scale}$$

(4.2)

Diamagnetic correction χ_0

Similarly, another factor that may affect the goodness of the data collected is purely related to an experimental aspect. By construction, the instrument used in the measurements can in fact introduce diamagnetic contributions into the final data, connected, for example, to the material from which the sample holder is made. This correction (called χ_0) will act on susceptibility and magnetization as a linear contribution in temperature or magnetic field respectively; one has in fact:

$$\chi T \rightarrow \chi T + \chi_0 T$$
$$M \rightarrow M + \chi_0 B \tag{4.3}$$

Given this linear dependence, it is expected that the correction is more influential at high magnetic fields and high temperatures. However, the measurements performed are obtained with relatively low magnetic fields (order of T) and consequently no great variations in magnetization are expected. On the other hand, temperatures reach values in the order of 100° C, around which the diamagnetic correction will be more important.

Parameters number reduction

The number of parameters listed in table 4.1 exceeds 20, so it is clear that the complexity of the parameter space is extremely high. The aim is therefore to try to reduce the number of these parameters by adopting different reasoning:

- Given the $C3$ symmetry of the molecule, with the dysprosium ions positioned approximately on the vertices of an equilateral triangle, it can be assumed that the parameters related to the type of an ion are the same for all three of them. Accordingly, it is assumed that

$$D_1 = D_2 = D_3 \stackrel{\text{def}}{=} D,$$
$$E_1 = E_2 = E_3 \stackrel{\text{def}}{=} E,$$
$$g_1 = g_2 = g_3 \stackrel{\text{def}}{=} g$$

- In the high anisotropy approximation, thus allowing the effective model to be used, the value of D will be irrelevant as long as it assumes sufficiently high values. It may therefore be disregarded in the fit phase. Furthermore, considering the contribution of the anisotropy as purely axial, the value of E is also irrelevant in the eigenvalues of energy, susceptibility and magnetization, and can therefore also be set equal to 0 and neglected. Similarly, with axial anisotropy, the *alpha* angle, which describes a rotation of the anisotropy tensor around the principal axis, will make no contribution, and can be set at 0 for ease.

- For the same symmetry reasoning done before, the coupling value between ion pairs can also be assumed constant, therefore:

$$J_{1,2} = J_{2,3} = J_{3,1} \stackrel{\text{def}}{=} J$$

- A further simplification can be achieved by reducing the number of parameters for describing the anisotropy axes. In particular, since the physics of the problem is independent of the reference system, it is possible to choose an appropriate one in which one of the axes (x axis) is parallel to the anisotropy axis of the first ion ($theta1 = 90°, phi1 = 0°$). In this way it is possible to fix the anisotropy angles of the first ion and leave only those of the other two free to vary.

With these simplifications, we have therefore reduced the dimension of the parameter space to 8 degrees of freedom, namely:

$$J,\ theta2,\ phi2,\ theta3,\ phi3,\ g,\ m_{scale},\ \chi_0 \tag{4.4}$$

However, the number of parameters is still very high when looking again at the experimental curves in figure 3.3. The absence of particular features in the points leads to greater difficulty in achieving an ideal fit and a case of overparametrization will have to be dealt with. One can therefore expect the presence of several sets of parameters leading to the same simulated curve, leaving aside the additional difficulty due to the possibility of the fit converging at a relative minimum of the χ^2 landscape.

4.2 Fitting the data in the effective model

4.2.1 Starting point: ideal configuration

As a first indication, from crystallographic measurements, we know that the dysprosium ions are positioned approximately at the vertices of an equilateral triangle, and the molecule is synthesised with the aim of having a good toroidicity (see chapter 6). In particular, we can choose the orientation of the anisotropy axes so that they lie in the plane of the $3Dy$ triangle, with azimuthal angles 120° apart. Under the assumption of high anisotropy, the Heisenberg coupling J can then be chosen to be of low intensity and antiferromagnetic ($J < 0$), while the diamagnetic and molar mass corrections can be initialised to 0 and 1 respectively, so that they make no contribution. Moreover the Landé factor can be chosen as the theoretical one for Dy ions, namely $g = 4/3$. Summarising what has been said so far, the choice of initial parameters therefore results (see table 4.2):

J	$theta2$	$phi2$	$theta3$	$phi3$	g	m_{scale}	χ_0
-0.05 K	90°	120°	90°	240°	1.33333	1	$0\ cm^3Kmol^{-1}$

Table 4.2: Choice of the initial parameters supposing the 3Dy ions in an ideal configuration to maximize the toroidicity.

A further simplification that can be initially adopted is to fix the position of the azimuthal angles phi (0°, 120° and 240°) and to leave the polar angles theta free to vary at the same time, thus imposing $theta1 = theta2 = theta3 \overset{\text{def}}{=} theta$. In the following we will refer to this configuration as "*umbrella configuration*". The parameters to fit, with their initial values, will reduce therefore to (table 4.3):

J	$theta$	g	m_{scale}	χ_0
-0.05 K	90°	1.33333	1	$0\ cm^3Kmol^{-1}$

Table 4.3: Choice of the initial parameters in the *umbrella configuration*, thus fixing the *phi* angles to 0°, 120° and 240° and using the same polar angle *theta* for all the three ions.

Before going into the fit procedure, it is possible to compare the experimental curves with those simulated using the parameters of the ideal configuration described above. The result can be seen in figure 4.1, where, as conventionally adopted in the following, the experimental data are shown as points in the graph, while the simulated (or fit) curves are shown as solid lines.
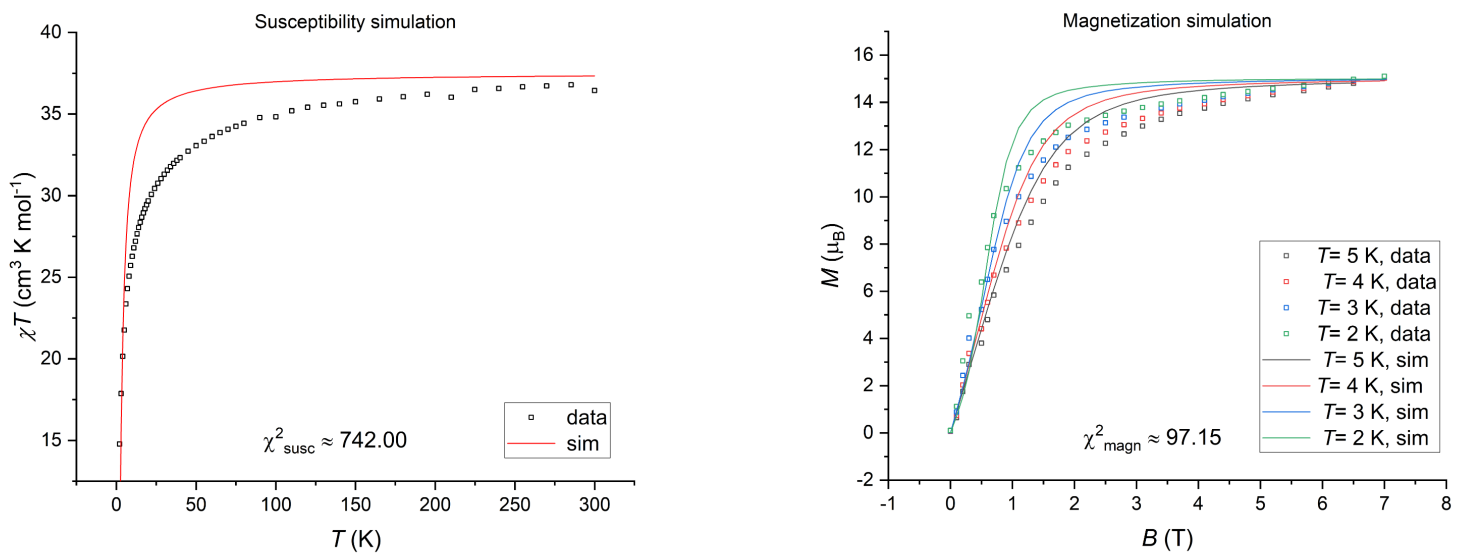
Figure 4.1: Susceptibility and magnetization simulation (lines) for the ideal configuration, so with the parameters of table 4.3, superimposed to the experimental data (points).

The simulated curves for the ideal configuration thus show a similar trend to the experimental data, but they only overlap them in the extreme regions of the independent coordinate, while in the majority of the graph the description of the system is clearly ineffective, which is also confirmed by the high χ^2 values shown inside the plots.

4.2.2   Role of each parameter in the simulated curves

As seen before, the ideal configuration does not lead to an acceptable representation of the data, so an optimisation of the parameters is necessary. Before proceeding with the actual fits, it is useful to gain a feeling for how larger or smaller variations in the parameters lead to larger or smaller changes in the susceptibility and magnetization graphs. This will also make it possible to assess how far the initial configuration is from the ideal fit, and to possibly adjust the initial fit parameters in order to increase the probability of converging to the absolute minimum of the χ^2. We then vary one parameter at a time by values around those of the ideal configuration. And we show then the corresponding simulated susceptibility and magnetization curves superimposed to the usual experimental curve. The result is shown in the figures 4.2 and 4.3.
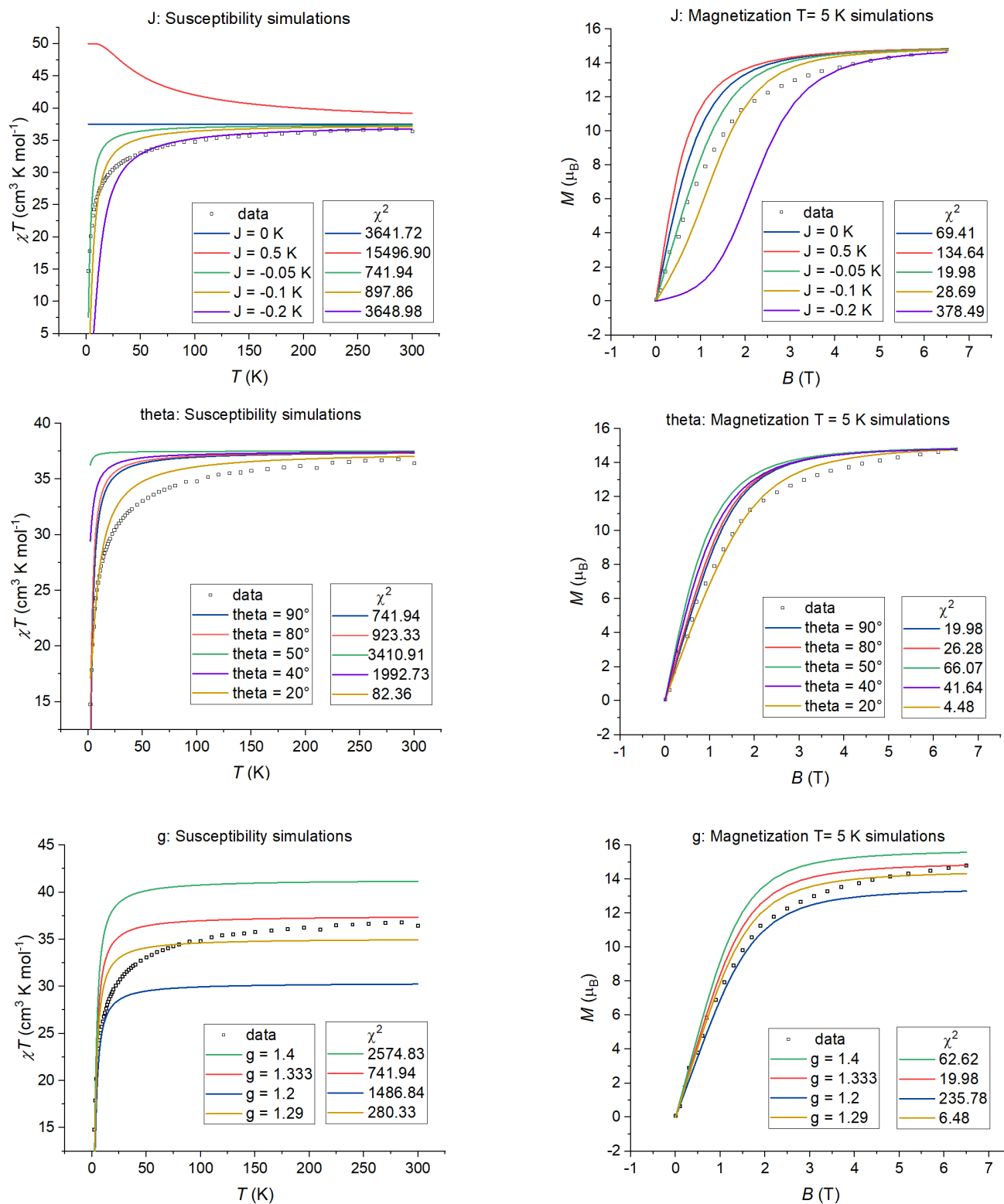
Figure 4.2: Comparison between different simulated susceptibility and magnetization curves for different values of the parameters: J coupling, polar angle *theta* and Landé factor g. Experimental data represented by points.
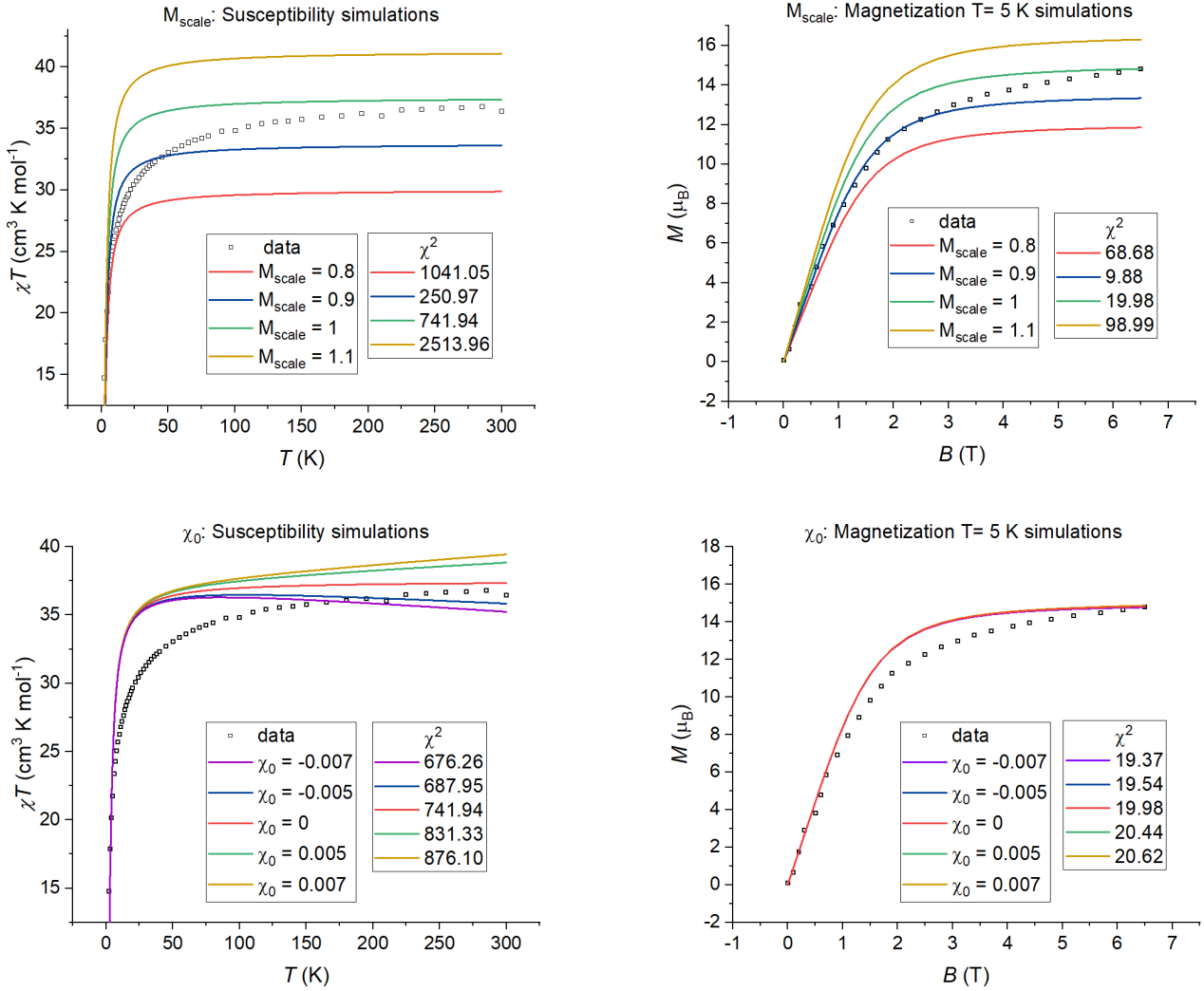
Figure 4.3: Comparison between different simulated susceptibility and magnetization curves for different values of the parameters: diamagnetic correction χ_0 and molar mass correction m_{scale}. Experimental data represented by points.

It can be seen from the graphs that the parameters of the ideal configuration are close to the representation of the experimental data, but some adjustments are necessary. In particular, one can expect a decrease in the polar angles $theta$ with respect to the value $theta = 90°$ in which the anisotropy axes are arranged in the plane of the ions, as well as a value < 1 for the molar mass correction and a reduction also in the Landé factor g. Nevertheless the parameters of the ideal configuration seem to be a good starting point for fits, which will be discussed in more detail in the next section.

4.2.3 Fit of 5 parameters: coupling, polar angle and corrections

One can then start the fit procedure by directly considering the five parameters shown in table 4.3, and simultaneously fit the magnetization and susceptibility data. The same table also shows the initial fit values, which, as explained above, contribute to the goodness of the final results and to the convergence of the algorithm in the global minimum or in a local minimum. The fit converged to a minimum value of χ^2 after 30 iterations, and the results are shown in picture 4.4 and table 4.4.
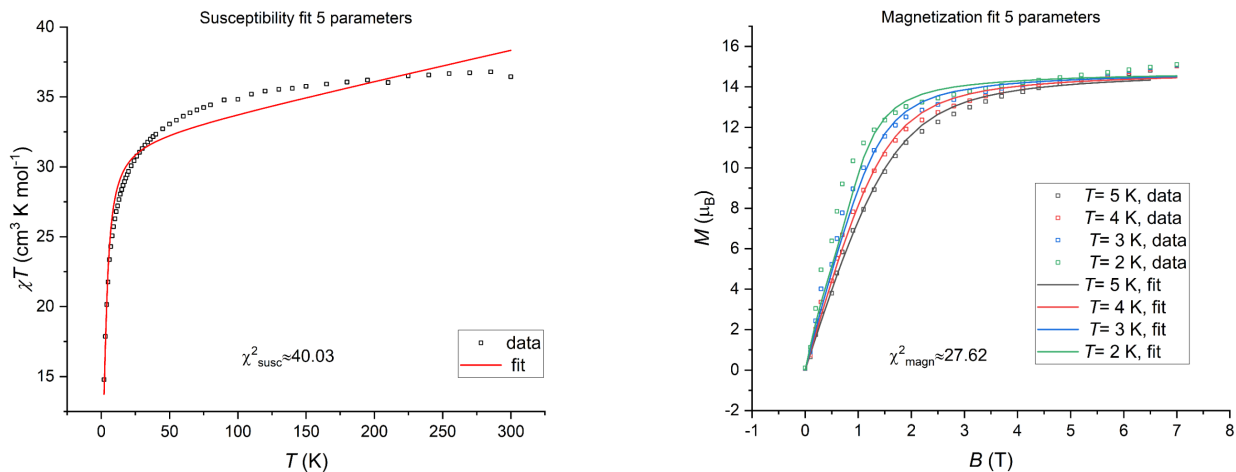
Figure 4.4: Direct fit of both susceptibility and magnetization with 5 degrees of freedom with initial parameters of table 4.3, so in the ideal configuration.

J	$-0.108(8)$ K
$theta$	$80.0(7)°$
g	$1.178(11)$
m_{scale}	$1.091(17)$
χ_0	$0.0200(12)$ $cm^3 K mol^{-1}$

Table 4.4: Fit parameters with initial parameters in the ideal configuration.

The results obtained show good agreement of the magnetization with the experimental data, while a particularly different trend is seen with regard to the susceptibility. A quantitative measure of the goodness of the two fits can be seen in the χ^2s values, directly shown in the plots.

With suspected convergence in a local minimum, therefore, one can attempt to improve the fit result by changing the values of the initial parameters. In particular, as seen in figures 4.2 and 4.3, better trends are obtained by reducing the value of the *theta* angles, and the value of the Landé factor g. We therefore repeat the fit using as initial parameters the values that provided the smaller χ^2 results in those simulations.

Moreover, the linear trend of the susceptibility for temperatures above $50°$, with a slope that does not respect the experimental data, suggests a too high value of the diamagnetic correction χ_0, which, remembering what was said before, gives a contribution of type $\chi_0 T$, therefore linear in temperature. In the following fits, it was therefore decided to initially set the value of χ_0 to 0.005, as it can be seen in figure 4.3 that it only varies at temperatures $> 50°$, and this curve is the closest to the slope of the experimental data. After performing the fit with the value of χ_0 fixed, a second fit is performed, leaving only χ_0 free to vary, and fixing all the other parameters according to the results of the first fit.

The initial parameters are shown in table 4.5 and the results in figure 4.5 and table 4.6.

J	theta	g	m_{scale}
-0.05 K	20°	1.29	0.9

Table 4.5: Initial parameters choosing the one that gave the smallest χ^2 values in the simulations of figures 4.2 and 4.3.
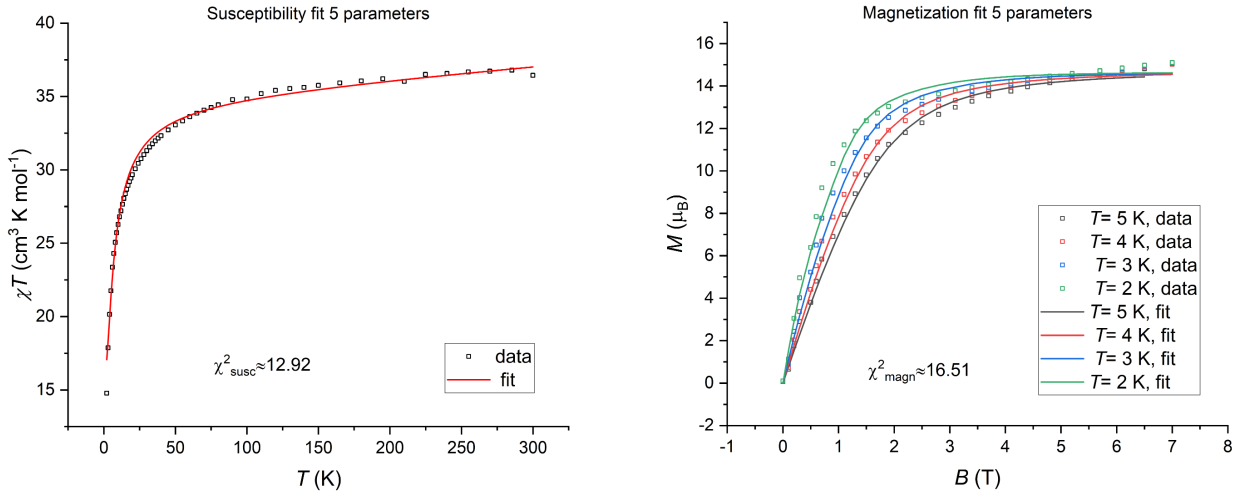

Figure 4.5: Direct fit of both susceptibility and magnetization with 5 degrees of freedom with initial parameters of table 4.5.

J	$-0.044(2)\ K$
$theta$	$22.0(9)°$
g	$1.278(7)$
m_{scale}	$1.015(1)$
χ_0	$0.0078(5)\ cm^3 K mol^{-1}$

Table 4.6: Fit parameters with initial parameters of table 4.5.

The fit converged after 41 iterations, reducing the χ^2s of susceptibility and magnetization respectively by a factor of 3 and a factor of 1.5.

The fit parameters obtained allow a good description of the physical model, but once again it is possible that the global minimum was not reached. To check whether this is the case, it is possible to directly observe the landscape of the χ^2 as a function of two parameters at a time. We then choose the pairs $J - theta$ and $m_{scale} - g$, and proceed to simulate the susceptibility and magnetization curves for each pair of values by deriving a value for χ^2. In figure 4.6, the two landscapes for susceptibility and magnetization are shown separately (figures 4.6a and 4.6b) and then superimposed in figure 4.6c. The plot in figure 4.6d then shows the total chi square calculated as the sum of χ^2_{susc} and χ^2_{magn}. For each plot, it is then highlighted the point that minimises the χ^2 in the different cases considered.
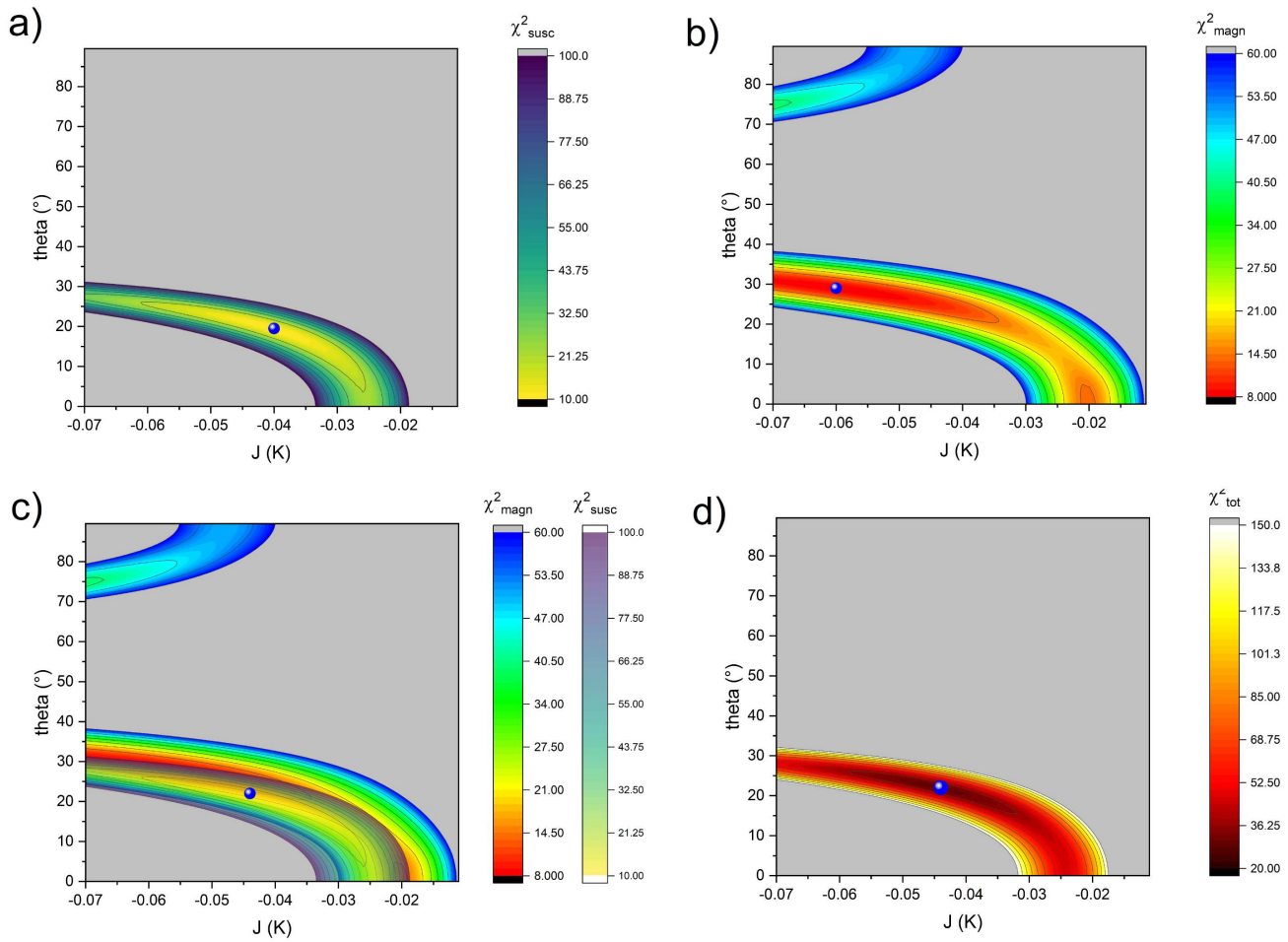
Figure 4.6: χ^2 landscapes for the couple of parameters $J - theta$ relative to susceptibility (a) and magnetization (b). In plot (d) we superimposed the landscapes shown in (a) and (b), while in (d) one can see the sum of the two χ^2s. The blue points show in each case the couple of parameters that minimizes the χ^2.
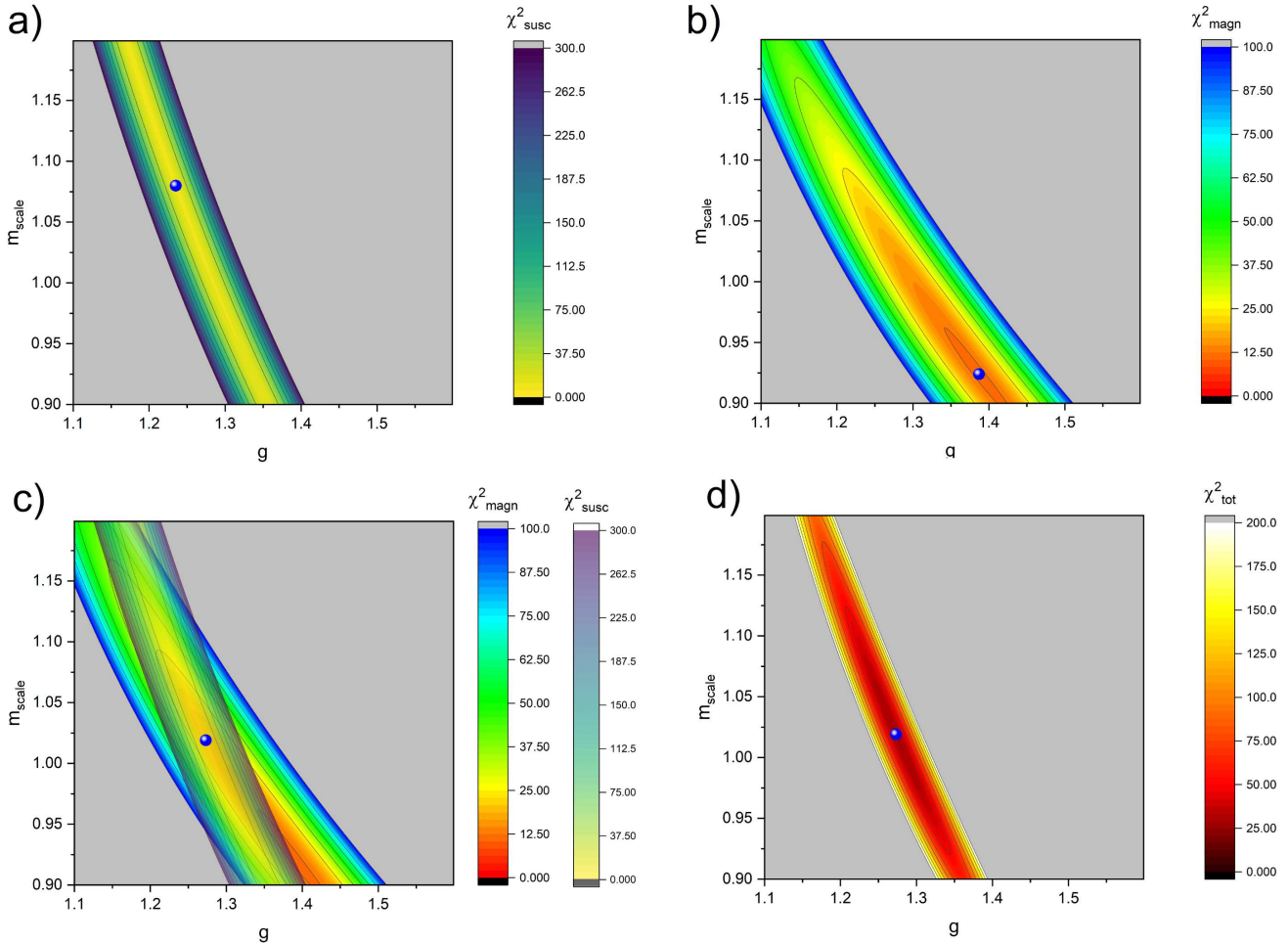
Figure 4.7: See figure 4.6 for parameters $m_{scale} - g$.

The landscapes shown do not appear to have overly complicated elements, so it is possible to ascertain that the configuration found is a global minimum of χ^2 both visually and by comparing the point of minimum of the landscapes with that obtained by fit of table 4.4. From the graph in figure 1, it can also be seen that the m_{scale} and g parameters are linked to each other, but the m_{scale} parameter does not affect the fit in a extremely significant way. It does, however, allow the fit to be corrected and improved, taking into account the experimental difficulties in measuring the molar mass of the molecule, so it will still be considered as a fit parameter.

4.2.4 Fit including other parameters

In the fits performed so far, we have reduced the number of parameters to a minimum, looking for the simplest model close to the ideal configuration that could give a good interpretation of the experimental data. The result obtained is satisfactory, but the question arises as to whether the addition of further parameters can significantly improve the result of the fit.

In the following three subsections we will therefore add some fit parameters, in particular: considering the ideal configuration but with three different *theta* angles free to vary, one for each ion; ideal configuration with the same *theta* angle for each ion, but leaving the *phi* angles free to vary, setting the ideal angles 0°, 120° and 240° as initial parameters; complete fit with three different *theta* angles and three different *phi* angles.

For each case, a table is shown with the initial fit parameters, the corresponding graphs with

the susceptibility and magnetization curves, and a table with the values resulting from the fit. As before, the value of χ^2 is shown within the graphs.

Different three theta angles, ideal phi angles

J	$theta1$	$theta2$	$theta3$	g	m_{scale}
-0.05 K	20°	20°	20°	1.29	0.9

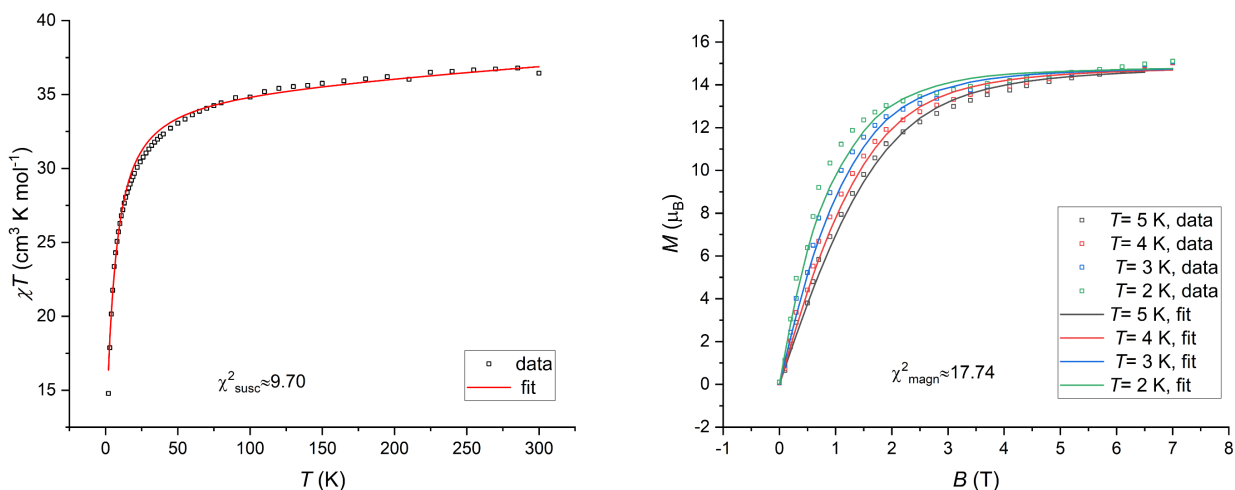Table 4.7: Initial parameters of the fit letting change all the three theta angles individually.
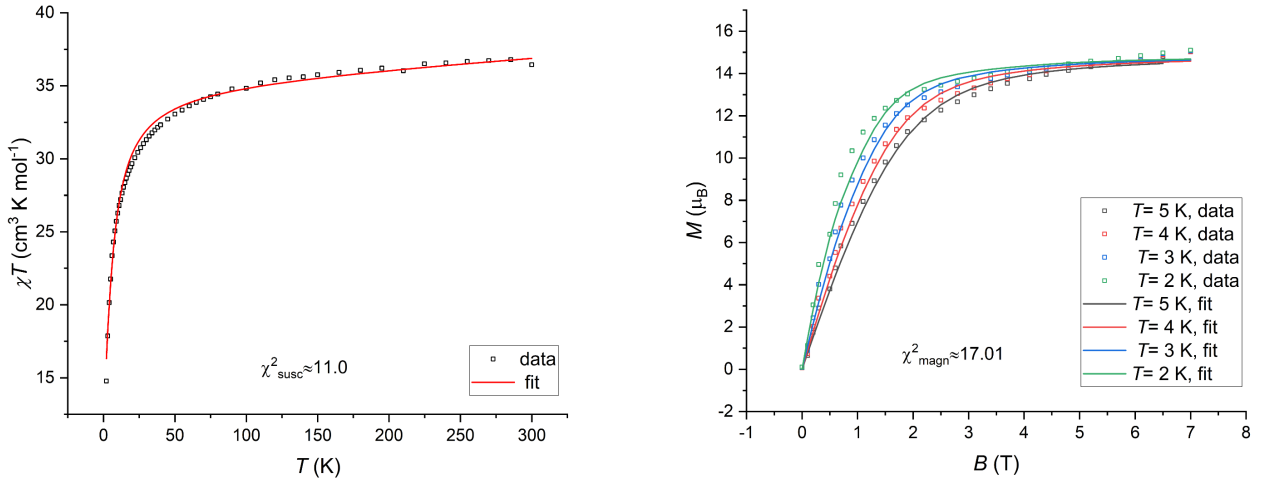

Figure 4.8: Direct fit of both susceptibility and magnetization with initial parameters shown in table 4.7, and adjusting the χ_0 value with a second individual fit.

J	$-0.088(11)\ K$	$theta1$	$11.5(1.7)°$
g	$1.264(8)$	$theta2$	$41(88)°$
m_{scale}	$1.046(12)$	$theta3$	$41(88)°$
	χ_0	$0.0063(5)\ cm^3Kmol^{-1}$	

Table 4.8: Fit results with initial parameters of table 4.5.

Different three phi angles free to vary

J	$theta$	$phi1$	$phi2$	$phi3$	g	m_{scale}
-0.05 K	20°	0°	120°	240°	1.29	0.9

Table 4.9: Initial parameters of the fit letting change also the phi angles individually.
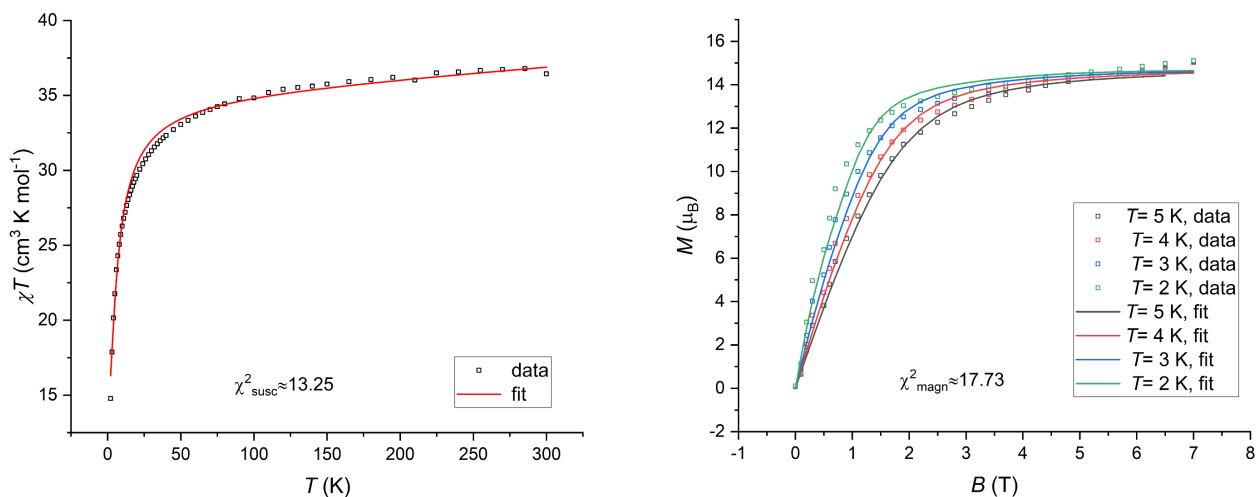
Figure 4.9: Direct fit of both susceptibility and magnetization with initial parameters shown in table 4.9, and adjusting the χ_0 value with a second individual fit.

J	$-0.043(8)\ K$	$phi1$	$-19(77)°$
g	$1.23(11)$	$phi2$	$175(86)°$
m_{scale}	$1.012(17)$	$phi3$	$259(138)°$
$theta$	$25(7)°$	χ_0	$0.0067(5)\ cm^3Kmol^{-1}$

Table 4.10: Fit results with initial parameters of table 4.9.

Different three phi and three theta angles free to vary

J	$theta1$	$theta2$	$theta3$	$phi1$	$phi2$	$phi3$	g	m_{scale}
-0.05 K	20°	20°	20°	0°	120°	240°	1.29	0.9

Table 4.11: Initial parameters of the fit letting change both the phi and the theta angles individually.

Figure 4.10: Direct fit of both susceptibility and magnetization with initial parameters shown in table 4.11, and adjusting the χ_0 value with a second individual fit.

J	$-0.065(17)\ K$	m_{scale}	$1.030(17)$
$theta1$	$32(52)°$	$phi1$	$295(79)°$
$theta2$	$51(67)°$	$phi2$	$37(55)°$
$theta$	$-10(55)°$	$phi3$	$251(120)°$
g	$1.273(11)$	χ_0	$0.0065(5)\ cm^3Kmol^{-1}$

Table 4.12: Fit results with initial parameters of table 4.11.

4.2.5   Final considerations on the models: role of the azimuthal phi angles

The previous fitting attempts show that the addition of further parameters does not lead to any improvement in the magnetization, but only slightly in the susceptibility (see the case of three different theta angles).

The fit results show that the parameters also considered previously (J, m_{scale}, $theta$, g, χ_0) always assume similar values and with acceptable accuracies. However, the results of the $theta$ and/or phi angles show extremely high uncertainties, comparable with the values themselves, a sign of a low influence in the final curves of the fits.

We can empirically verify the non-dependence of the powder magnetization and susceptibility on the phi angles. To do this in figure 4.11 are shown the graphs of susceptibility and magnetization for different phi angle configurations of the anisotropy axes. All phi angles were increased by the same Δphi value, or the phi angle of a single ion was changed, or all angles were changed independently. In particular are shown the configurations of phi angles (0°, 120°, 240°) and (90°, 210°, 330°), i.e. those which will then provide the maximum and minimum toroidal moment.
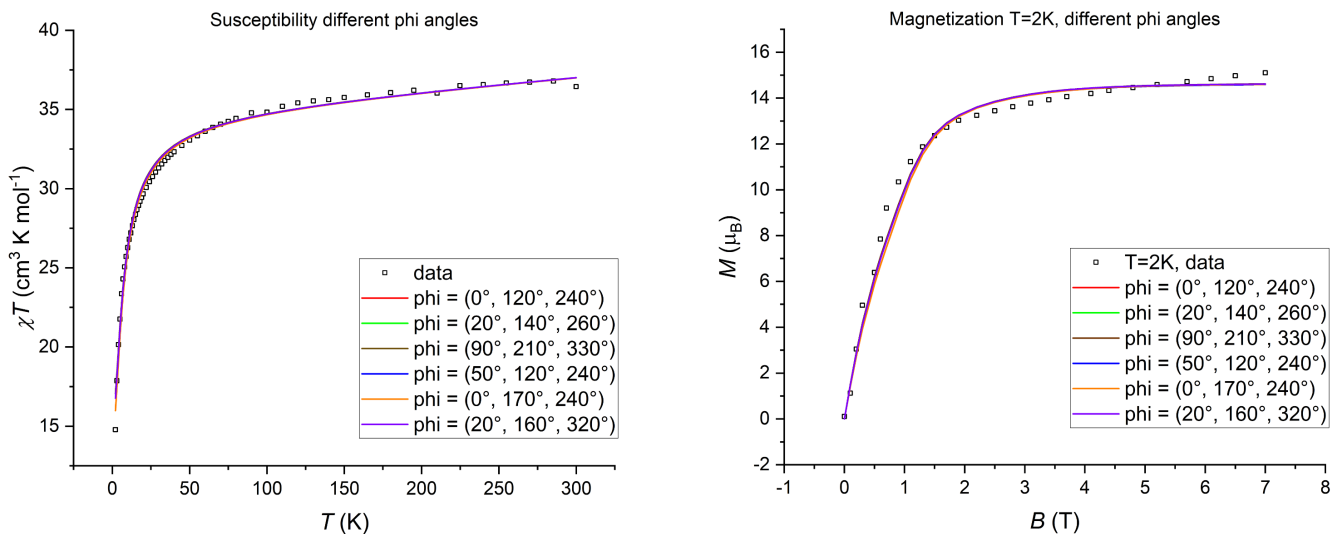
Figure 4.11: Simulations of susceptibility and magnetization for different configurations of phi angles and for the other parameters obtained from the fit relative to table 4.6. The simulations (solid lines) are superimposed to the experimental data (points).

The figure thus clearly shows a negligible dependence of the simulated curves on the choice of phi angles. This therefore has a fundamental consequence on the toroidicity of the molecule. In fact, it has been possible to derive the tilting of *theta* angles with respect to the plane in which the ions lie, but no information can be derived on the *phi* angles. As mentioned earlier, therefore, the configurations exhibiting the highest and lowest toroidicity (choosing the same *theta* angles) have the same powder magnetization and susceptibility values.

Thus, no complete information on the toroidicity can be derived from the common measurements in a powder sample of magnetization and susceptibility, and different experimental techniques has to be investigated (Inelastic Neutron Scattering).

4.3 Simulation with the full model

Given the results obtained, we can therefore follow the principle of Occam's razor and consider the simplest model to describe the experimental data, having thus shown how the ideal configuration with polar angles theta slightly inclined with respect to the axis perpendicular to the plane provides a satisfactory result. Therefore, as mentioned above, the fits performed so far have been carried out using the effective Hamiltonian model in order to reduce the computational time. We have already shown that the effective model and the full model provide results that are extremely close to each other.

However, it is good practice to check that the fit parameters obtained with the effective model also describe the experimental data with the same accuracy as with the full model. Since the simulations (without fit) can also be performed in a reasonable time in the full model, we proceed to simulate the susceptibility and magnetization curves using the fit parameters shown in table 4.4.
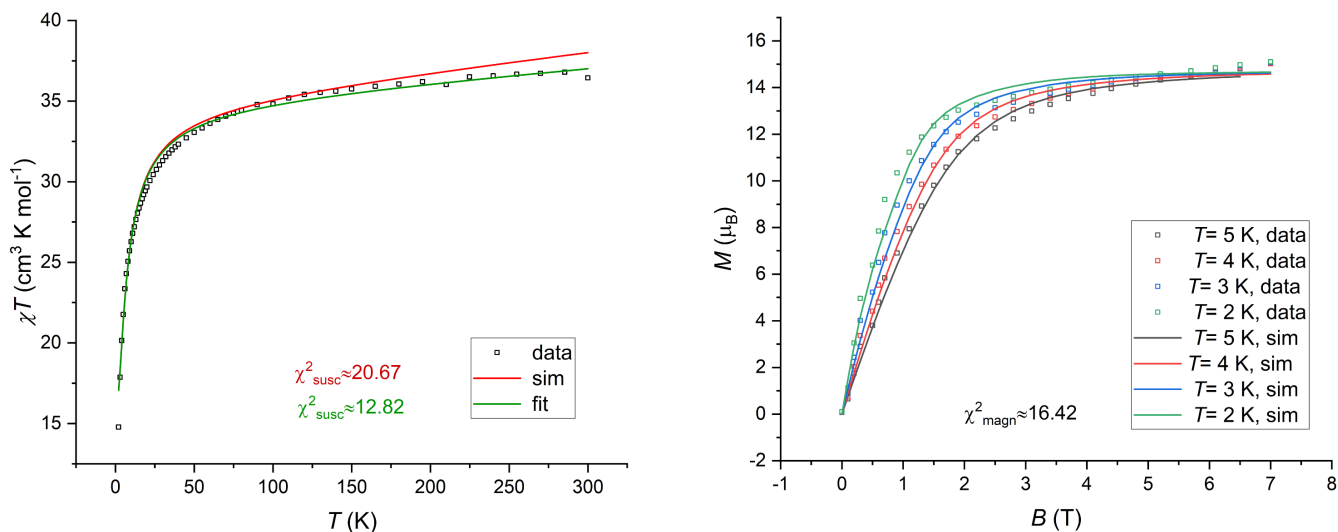
Figure 4.12: Simulation in the full model using the parameters found through the fit and shown in table 4.4. The green curve of the susceptibility is obtained fitting only the diamagnetic correction χ_0.

The simulation performed with the full model gives practically the same results for the magnetization, while the susceptibility (red curve in the left graph) shows a trend that diverges from the data for temperatures higher than about $50\ K$. As explained previously, the effective model focuses on the ground state, i.e. to the low temperatures range, and neglects possible state mixing with high lying states.

However, at high temperatures, the contribution of the diamagnetic correction χ_0 becomes important. Maintaining the same parameters used for the simulation, we have therefore allowed χ_0 to vary and fitted this parameter. The result of the fit is therefore a diamagnetic correction of $\chi_0 = 0.0046(6)\ cm^3Kmol^{-1}$, and the susceptibility curve (plot in green) returns to correctly overlay the experimental data.

We can therefore once again confirm the reliability of the effective model, barring any corrections at high temperatures, and validate the parameter values obtained by fit.

Chapter 5

Energy eigenvalues: exploration in the parameter range

5.1 C3-fold symmetry and relation with the energy eigenvalues

As described previously (chapter 3), the molecule under study shows a particular geometrical structure made up of the three Dy ions and of the surrounding ligands. One can therefore expect this structure to present a symmetric behaviour, and in particular, due to the triangular arrangement of the Dy ions, a C3-fold rotation symmetry can be investigated. The geometrical shape of the molecule and its properties should remain so unchanged under rotations of $\frac{2}{3}\pi$ around its principal axis, that in this case, due to the choice of the reference system described in section 3.1, correspons to the z axis, which is approximately the perpendicular to the Dy triangle plane passing through the central point.

In this instance we will focus on the energy response of the molecule if an external magnetic field is applied, and, in particular, on how the direction of this field affects the energy spectrum of the system. Using the standard configuration of the molecule and the same frame of reference described in section 3.1, we can apply an external unitary magnetic field $B = 1\,T$ changing its orientation with respect to the xy plane (ϕ_B angle) and the yz (θ_B angle) and looking at the lowest energy eigenvalue $E0$ of the molecule. The result is plotted in figure 5.1.

For clarity of exposition, one can also see the same behaviour in plots in figure 5.2, in which the same data have been plotted fixing the angles θ_B and then ϕ_B respectively to 90 and 120.

From these graphs it is straightforward to recognize a 3-fold periodicity of 120°, which come from the C3-fold symmetry, when the B field is spanned around the Dys plane. But in addition to this, one can also notice a periodicity of 60°, so a duplication into 6 folds. This is caused by the fact that a rotation of the anisotropy axes of 180° leads to the same results, since that the anisotropy is described by an axes and not by a vector. This behaviour is a confirm of the symmetry under study, and can be analytically proven looking at the anisotropy tensors D of each ion. In table 5.1, are shown these tensors, obtained rotating the initial diagonal matrix $D_{unrotated}$ accordingly to the angles of the standard configuration.

It is so possible to verify the validity of the following relations:

$$\begin{aligned}
\mathbf{D2} &= \mathbf{R}_{\varphi=120}\mathbf{D1R}^T_{\varphi=120} & \mathbf{D3} &= \mathbf{R}_{\varphi=60}\mathbf{D1R}^T_{\varphi=60} \\
\mathbf{D3} &= \mathbf{R}_{\varphi=120}\mathbf{D2R}^T_{\varphi=120} & \mathbf{D1} &= \mathbf{R}_{\varphi=60}\mathbf{D2R}^T_{\varphi=60} \\
\mathbf{D1} &= \mathbf{R}_{\varphi=120}\mathbf{D3R}^T_{\varphi=120} & \mathbf{D2} &= \mathbf{R}_{\varphi=60}\mathbf{D3R}^T_{\varphi=60}
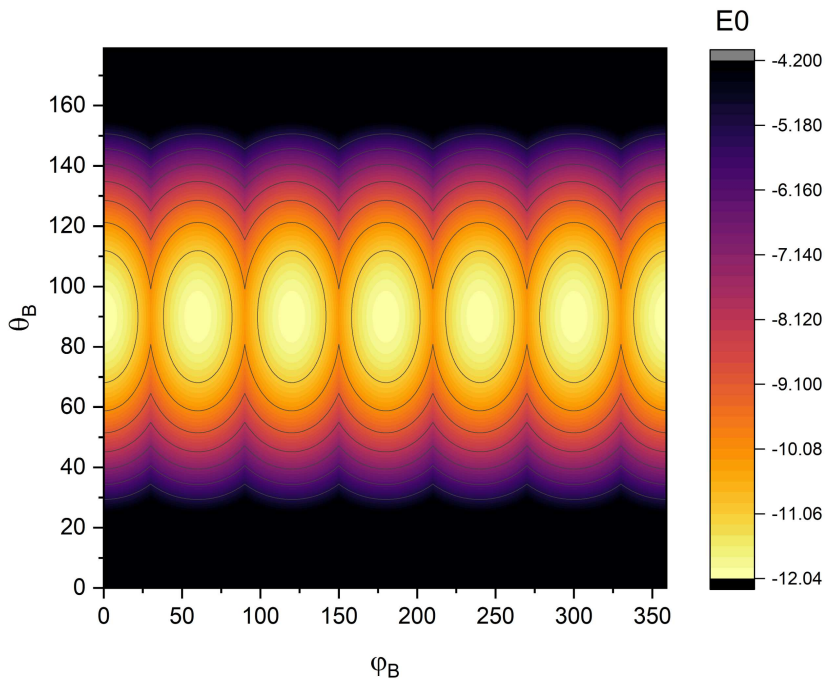\end{aligned} \tag{5.1}$$

Figure 5.1: Lowest energy eigenvalue changing the orientation of the magnetic field acting on the 3Dy molecule in the ideal configuration.
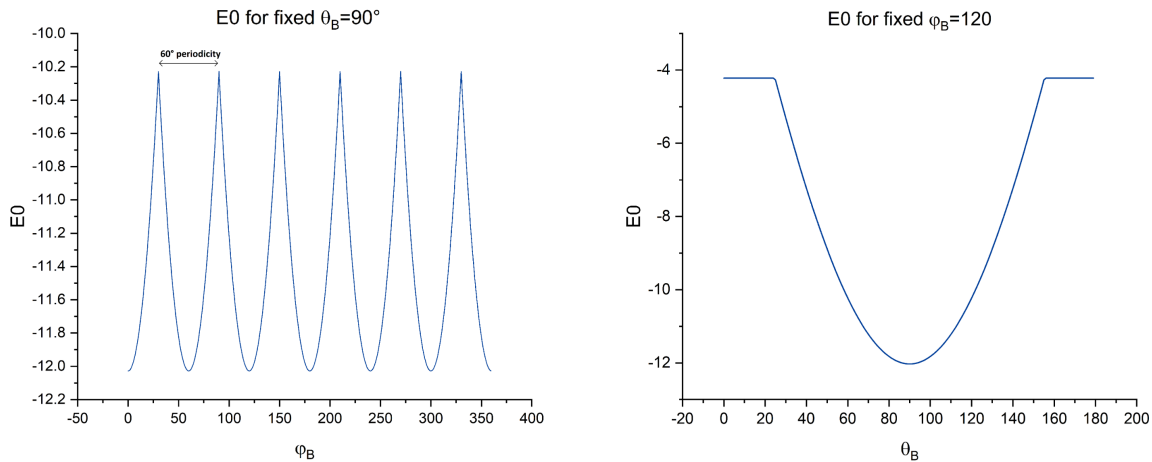

Figure 5.2: Lowest energy eigenvalue changing the rotating the magnetic field along the xy plane (on the left) or perpendicular that (on the right).

$D_{unrotated}$			$D1_{(90,0,0)}$			$D2_{(90,120,0)}$			$D3_{(90,240,0)}$		
100	0	0	-200	0	0	25	129.9	0	25	-129.9	0
0	100	0	0	100	0	129.9	-125	0	-129.9	-125	0
0	0	-200	0	0	100	0	0	-100	0	0	100

Table 5.1: Anisotropy tensors of the three ions rotating the initial matrix built with $D = -200$ and $E = 0$.

where R_φ is the rotational matrix of a certain angle φ around the z axis. These relations confirm so that the anisotropy axes are C3 fold symmetric, since the same matrices are obtained starting from one of the three ion and rotating it of 60° or of 240°, thus obtaining the same anisotropy

axis in the positive or negative direction.

5.2   Effects of anisotropy and exchange coupling individually

Isolated ions: only Zeeman effect

To deeply understand the energetic behaviour of the molecule, we can analyze the first energy eigenvalues when an external magnetic field of different intensities is applied. Starting from the case of $J = 0$ and $D = 0$, we are here neglecting completely the coupling between the spins and the interaction with the ligands, considering only the one with an external magnetic field. The Hamiltonian will therefore be reduced to a single contribution made by the Zeeman term:

$$H = \mu_B g_L S B \tag{5.2}$$

and this leads to the lowest energy values when all spins are aligned with the magnetic field, while any misalignment increases the energy of the system to that of a state in which all spins have the opposite direction to the field. This behaviour is present independently on the direction of the magnetic field, since no couplings or ansiotropies are considered.

The resulting energy levels with their degeneracies are shown in figure 5.3.
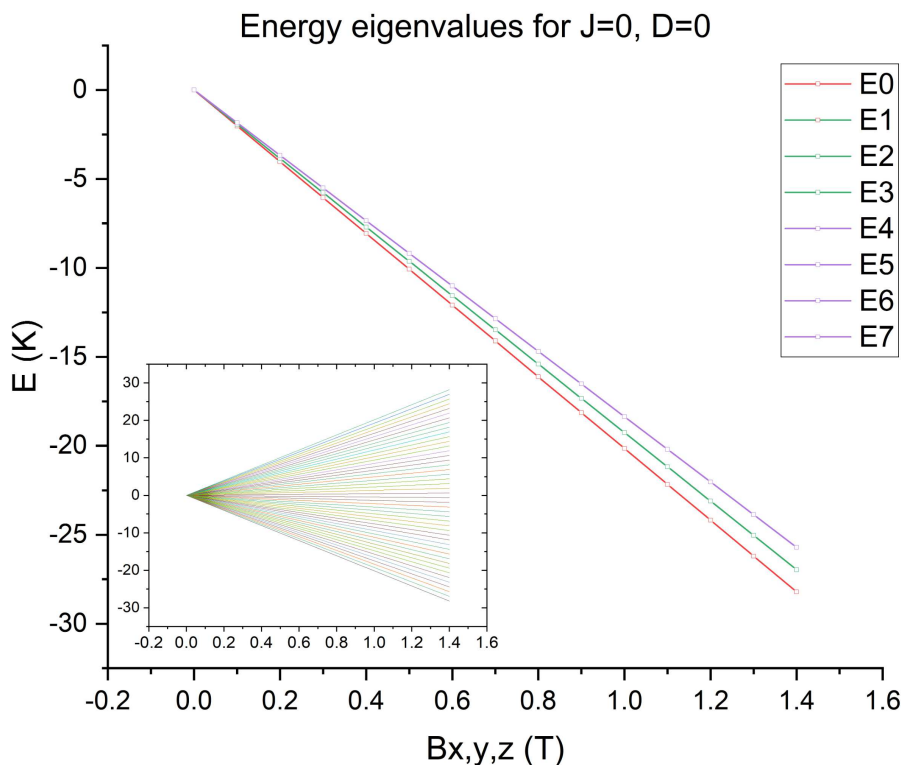
Figure 5.3: First 8 energy eigenvalues (complete calculation in the inset plots) as a function of the magnetic field oriented along the 3 axes for zero values of J and D.

From the inset plot of figure 5.3, one can see that there is no longer a clear separation between the first eight energy levels and the remaining excited states, and the spectrum will therefore be free of large energy gaps.

The slopes of the straight lines of the $E(B)$ plot will be simply given by $\delta E = \mu_B g S$, where S is the total spin of the state. The latter assumes the values $\frac{15}{2} \cdot 3$ in the ground state, with all the three spins equal to $\frac{15}{2}$, the value $\frac{15}{2} \cdot 2 + \frac{13}{2}$ when one ion is in the first excited state, and so on.

In table 5.2 it is so possible to compare the theoretical value computed as discussed above, considering a value of the Bohr magneton equal to $\mu_B = 0.671714 \ KT^{-1}$, with the slope of the simulated energies for the $3Dy^{3+}$ molecule obtained with a linear fit.

Simulation slope	Theoretical calculation	Spin state(s)
-20.15138	-20.15141	$\left\| \frac{15}{2}, \frac{15}{2}, \frac{15}{2} \right\rangle$
-19.25577	-19.25580	$\left\| \frac{13}{2}, \frac{15}{2}, \frac{15}{2} \right\rangle, \left\| \frac{15}{2}, \frac{13}{2}, \frac{15}{2} \right\rangle, \left\| \frac{15}{2}, \frac{15}{2}, \frac{13}{2} \right\rangle$
-18.36016	-18.36018	$\left\| \frac{11}{2}, \frac{15}{2}, \frac{15}{2} \right\rangle, \left\| \frac{15}{2}, \frac{11}{2}, \frac{15}{2} \right\rangle, \left\| \frac{15}{2}, \frac{15}{2}, \frac{11}{2} \right\rangle,$ $\left\| \frac{15}{2}, \frac{13}{2}, \frac{13}{2} \right\rangle, \left\| \frac{13}{2}, \frac{15}{2}, \frac{13}{2} \right\rangle, \left\| \frac{13}{2}, \frac{13}{2}, \frac{15}{2} \right\rangle$

Table 5.2: Energy eigenvalues of the first 8 states applying a magnetic field to the 3Dy molecule neglecting possible Heisenberg coupling J or local anisotropies D.

Note that the state with degeneration 4 in the figure would also include two further states (shown instead in the table) that have been excluded from the first 8 energy levels of the ground state.

With a similar reasoning it is straightforward also to explain the degeneracy values of each energy state, simply considering that the total energy must be the sum of the energies of each of the three ions. The spin of the the the Dy ion is 15/2, so it leads to 2s+1=16 different states, and, in particular, the ground state is given only by the combination of the three groundstates of the three ions, so only the $\frac{15}{2} \cdot 3$ combination is possible.

The first excited state is then given by the combination of two ions in the ground state and one in the excited state, which leads to 3 possible configurations. The third excited state is then given by two ions in the first excited state and one in the ground state, or by two ions in the ground state and one in the second excited state, leading to 6 different configurations since the energy difference between two consecutive states is the same and the energy states are equidistant.

Including an anisotropy D term

Introducing now an anisotropy term D the molecule will decrease its energy when the spins are aligned with the relative anisotropy axis. And, in the case of the high-anisotropy regime, a considerable energy gap will open between the lower 8 energy states and the higher lying states. The value of this gap will be comparable with the chosen anisotropy value. See figure 5.4.

In the ground state, one will therefore no longer find a spin of value 13/2, but combinations of spin +15/2 and -15/2 (in the local frame of reference in which the z axes is aligned to the anisotropy axes). This is due to the strong tendency of the spins to align with the axes of anisotropy, in absence of other interactions. Any misalignment leads to higher energy levels, while the presence of the magnetic field leads to a further contribution of energy that divides the energy levels themselves.

In figures 5.5, 5.6 and 5.7 it is possible to observe the behaviour of the energy eigenvalues as a function of an external magnetic field for different values of anisotropy. The first 32 energy eigenvalues were considered, 8 of which correspond, including the anisotropy term, to the low lying states and the remaining 24 to the excited states.

Applying now a magnetic field, in both directions x and y the progressive increase in the anisotropy leads to a splitting of the eigenvalues, creating a gap between the first 8 eigenvalues and the excited ones. There is so a separation, as mentioned above, between the eigenstates
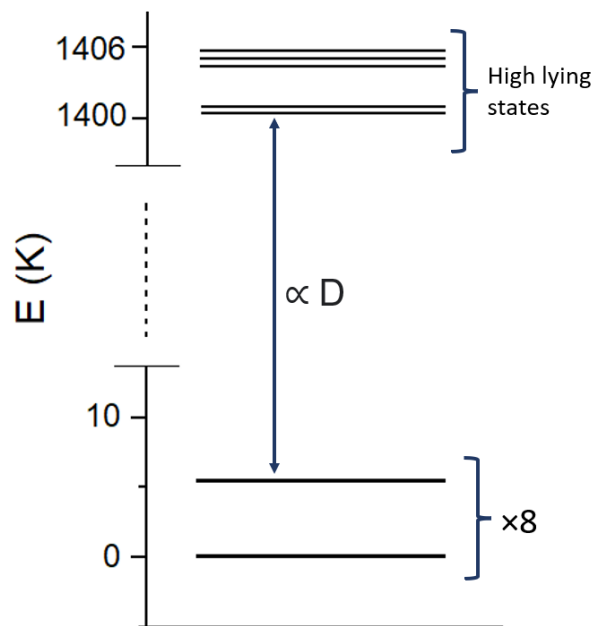
Figure 5.4: Energy eigenvalues of the $3Dy$ molecule with an anisotropy term $D = -100\ K$ and in absence of external magnetic fields..
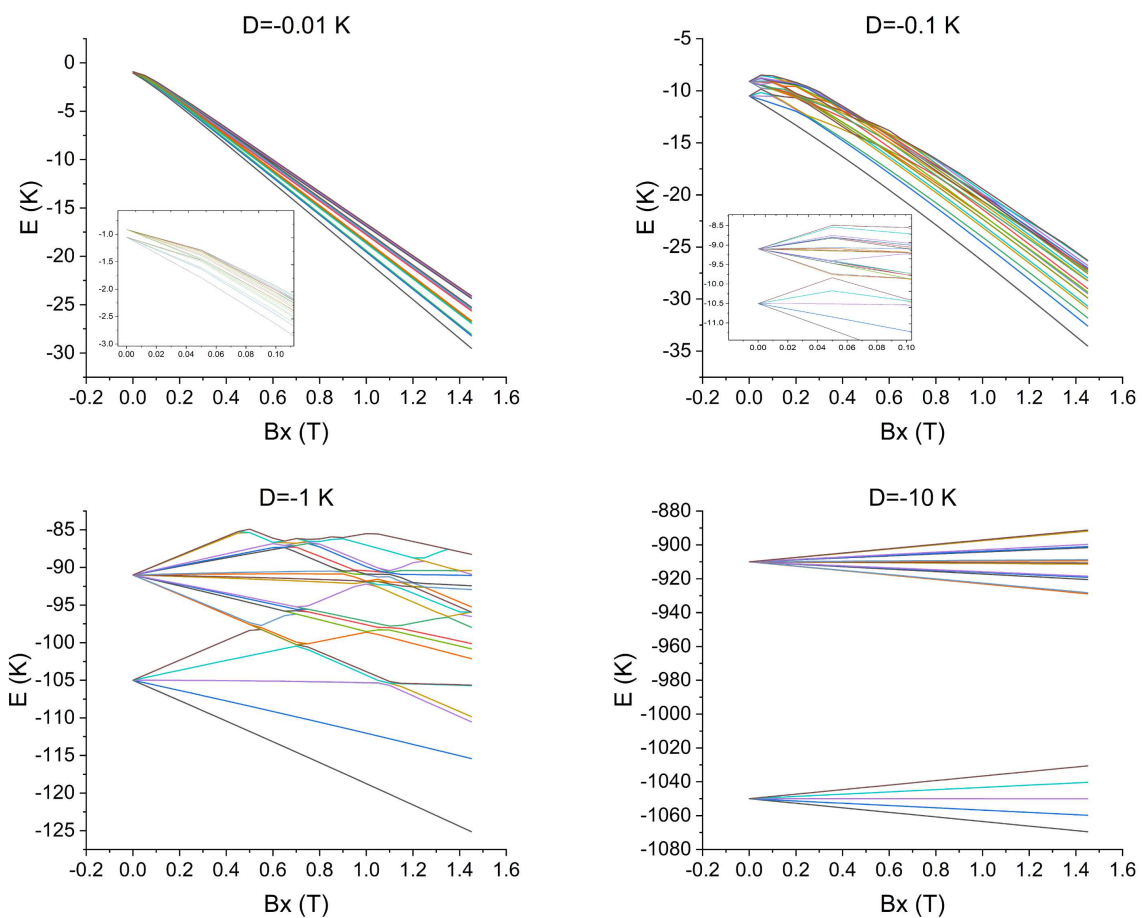

Figure 5.5: Eigenvalues as a function of the magnetic field applied in the x direction for different values of anisotropy.
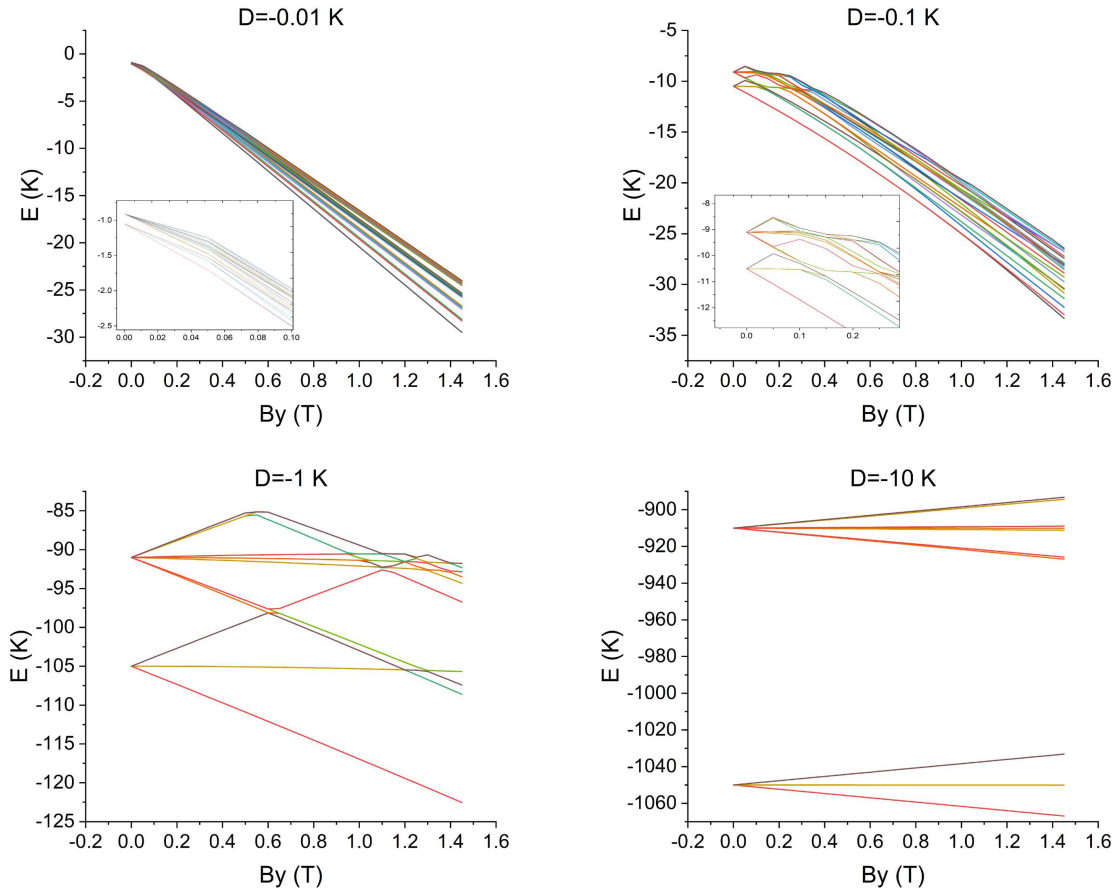
Figure 5.6: Eigenvalues as a function of the magnetic field applied in the y direction for different values of anisotropy.

formed by spin $\pm 15/2$ and those formed by other possible combinations. For very low values of anisotropy, the magnetic field appears to have the main impact on the energy structure, finding a similar trend to that shown for $D = 0$ in figure 5.3.

When, on the other hand, the anisotropy term assumes high values, the spins of the ions tend to align with these axes, thus, by construction, parallel to the plane in which the Dy triangle lies. This explains why the magnetic field turns out to have a negligible effect when it is perpendicular to the ions plane (fig. 5.7). In fact, the energy contribution depends on the scalar product between the magnetic field and the spin vector, a product that is zero when the two vectors are perpendicular to each other. If, on the other hand, the field lies on the plane, it leads to a splitting effect of the energies, visible both in the low lying states and in the high lying states. It is then clear how the magnetic field leads to different energy values depending on its orientation in the plane, as mentioned in the figure 5.1.

We can see then in the plots an horizontal energy line that presents a degeneracy 2. These lines can be traced back to the states $\left|\frac{+15}{2}, \frac{+15}{2}, \frac{+15}{2}\right\rangle$ and $\left|\frac{-15}{2}, \frac{-15}{2}, \frac{-15}{2}\right\rangle$ (see figure in the central raw of table 5.3) in which there is a cancellation of the Zeeman contribution, since the sum of the scalar products between the spins and magnetic field is zero. In this configuration, the increase in the modulus of the magnetic field has no influence on the energy eigenvalues, which are therefore constant.

The other lines of the 8 low lying states spectra are symmetrical to the horizontal one just described. These describe the states in which the spins take mixed $+15/2$ and $-15/2$ values,
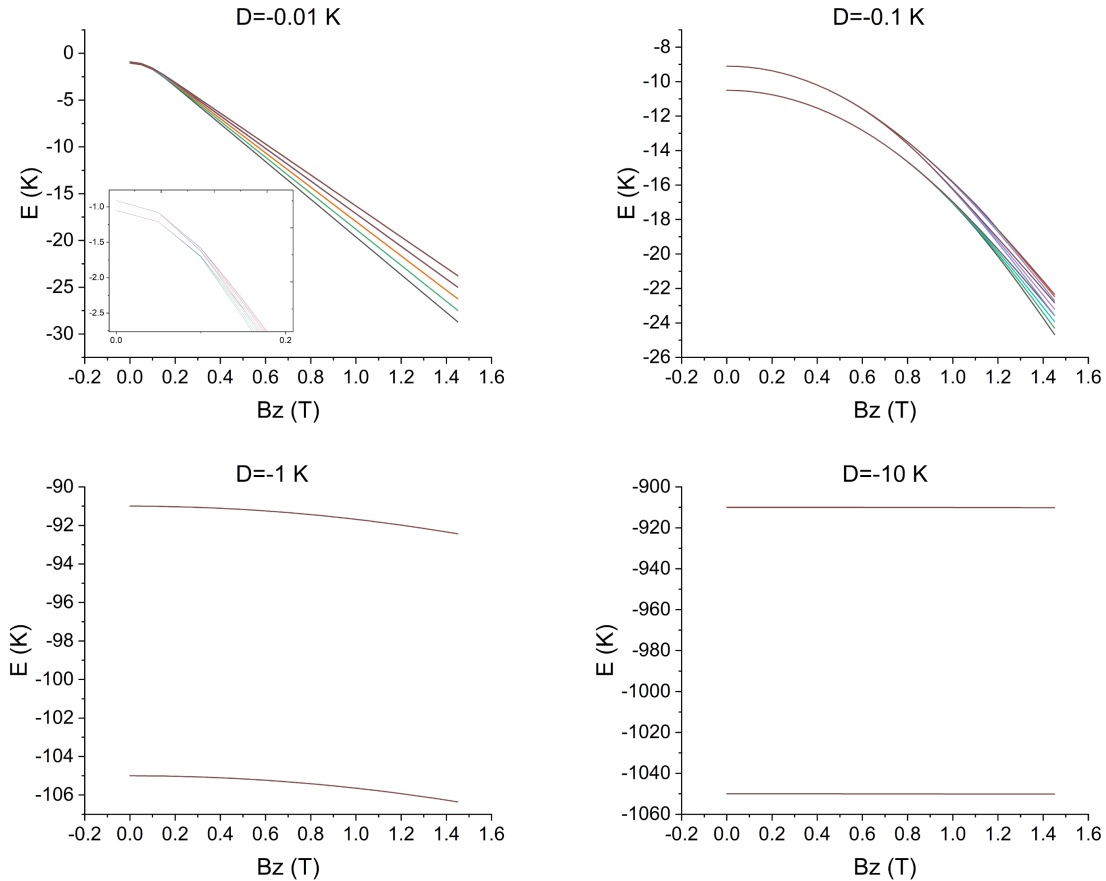
Figure 5.7: Eigenvalues as a function of the magnetic field applied in the z direction for different values of anisotropy.

thus leading to a non-zero Zeeman contribution. To numerically clarify what has been said, in table 5.3 are shown the 8 possible low lying states with the relative slopes of the line in the $E(Bx)$ plane. These values has been appropriately compared with the relative theoretical one obtained in a similar manner to that of relation 5.2.

Similar results could be found rotating the magnetic field in the y direction, with 4 degenerate configurations in which the Zeeman contribution is cancelled out (horizontal line with degeneracy 4 in the figure 5.6 for D=-10 K). Two other states with degeneracy 2 each will then split with respectively higher and lower energy than the central state just mentioned. It is therefore clear how different directions of the magnetic field lead to different energy eigenvalues.

Including Heisenberg coupling J

As mentioned in the theoretical introduction chapter, the Heisenberg coupling term, described by the Hamiltonian $-\sum_{i,j} J_{i,j}\mathbf{S}_i \cdot \mathbf{S}_j$, tends to align the different spins between each other, reducing the energy of the system when they are parallel to each other. Excluding anisotropy terms, it is therefore clear that the direction of a possible external magnetic field has no influence on the energy structure, since the spins will tend to align with each other and with the magnetic field itself. In figure 5.8 it is shown the energy spectrum as a function of an external magnetic field for different values of the Heisenberg J coupling.

Given the low coupling values considered, the magnetic field will have a greater influence on the energy structure; indeed, the same pattern can be recognised as found above in the absence of
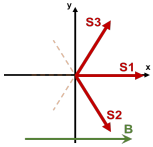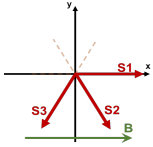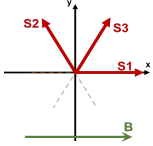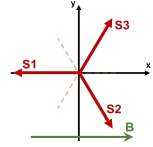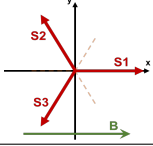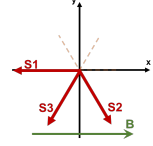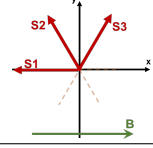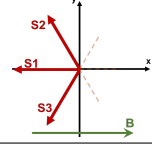
Spin scheme	Spin state	Slope (KT^{-1})
	$\left\lvert \frac{+15}{2}, \frac{-15}{2}, \frac{-15}{2} \right\rangle$	13.434
	$\left\lvert \frac{+15}{2}, \frac{-15}{2}, \frac{+15}{2} \right\rangle$	6.717
	$\left\lvert \frac{+15}{2}, \frac{+15}{2}, \frac{-15}{2} \right\rangle$	6.717
	$\left\lvert \frac{-15}{2}, \frac{-15}{2}, \frac{-15}{2} \right\rangle$	0
	$\left\lvert \frac{+15}{2}, \frac{+15}{2}, \frac{+15}{2} \right\rangle$	0
	$\left\lvert \frac{-15}{2}, \frac{-15}{2}, \frac{+15}{2} \right\rangle$	-6.717
	$\left\lvert \frac{-15}{2}, \frac{+15}{2}, \frac{-15}{2} \right\rangle$	-6.717
	$\left\lvert \frac{-15}{2}, \frac{+15}{2}, \frac{+15}{2} \right\rangle$	-13.434

Table 5.3: Spin ground states of the 3Dy system with an anisotropy value of D=-10 K and an external magnetic field pointing in the x direction.

interactions for sufficiently large magnetic fields. When, on the other hand, the coupling and Zeeman effects are comparable, i.e. at low values of the B field, a splitting in energy creates small gaps between the eigenvalues, as can be seen in the inset plots of figure 5.8.

5.3   Ground state and low lying energy behaviour

In the low exchange coupling approximation, i.e. strong anisotropy, the spins of the ions will then be forced to position themselves parallel to the anisotropy axes, thus at 120° from each other, separating the first octet of states from the remaining high-energy states. As explained in Chapter 2.2, this circumstance makes it possible to apply an effective Hamiltonian model, neglecting the high-energy states and considering only the first octet, thus considerably reducing the computation time and facilitating the interpretation of the results obtained.
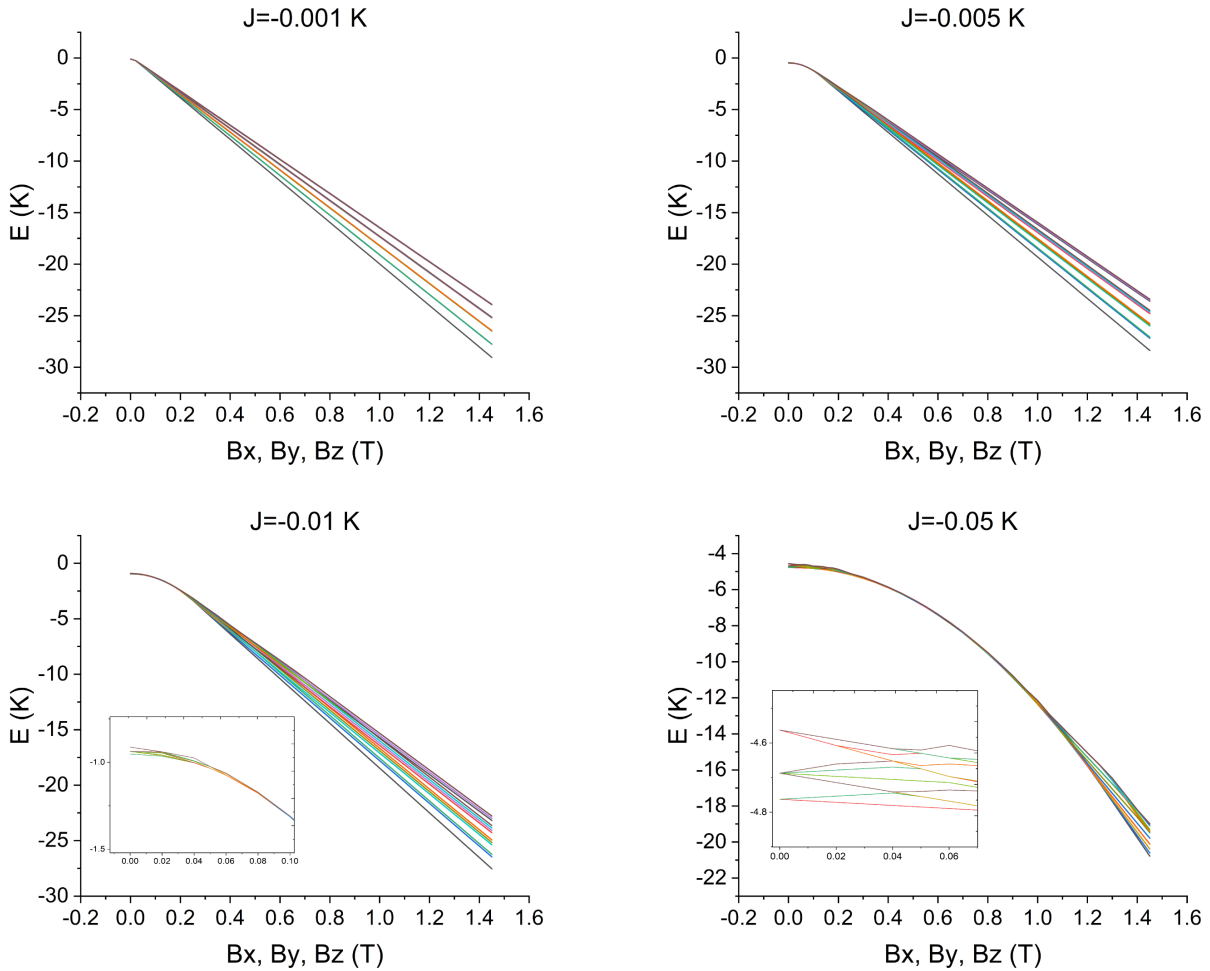
Figure 5.8: 3Dy energy spectrum as a function of an external magnetic field for different values of the Heisenberg coupling J. Enlargements of the initial region of low fields in the inset plots.

In this case, the anisotropy value will no longer contribute to the energy values, but only to the selection of the octet ground states and its separation from the other states. The Hamiltonian will therefore consist of only two contributions: the Heisenberg coupling and the Zeeman terms.

Heisenberg coupling J

In the case of zero magnetic field, the energy term given by the Heisenberg coupling will tend, in the case of the antiferromagnetic interactions under consideration, to maximise the angles between the spin pairs in order to reduce the energy of the system. Thus, in the low exchange coupling approximation, a ground state formed by the $\left|\frac{+15}{2}, \frac{+15}{2}, \frac{+15}{2}\right\rangle$ and $\left|\frac{-15}{2}, \frac{-15}{2}, \frac{-15}{2}\right\rangle$ configurations can be expected, while the other 6 spin configurations, with mixed signs, will be at higher energy levels in a degenerate state.

In figure 5.9, one can see what is described by observing the behaviour of the energy as a function of the modulus of the J term.

As done above, it is possible to calculate the slope in the straight lines in the graph 5.9 using the Heisenberg Hamiltonian term, thus simply calculating the scalar product between the spin vectors $\pm\frac{15}{2}$ and separated from each other by angles of 120 and 240°. The results are shown in table 5.4.
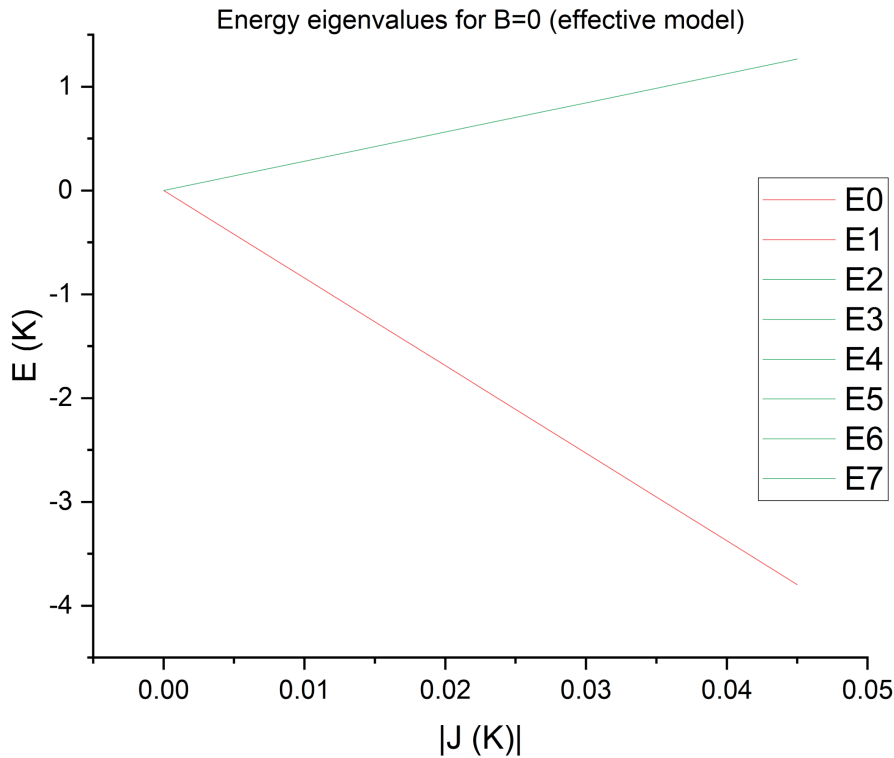
Figure 5.9: 3Dy energy spectrum as a function of an external magnetic field for different values of the Heisenberg coupling J. Enlargements of the initial region of low fields in the inset plots.

In addition, it is possible to calculate the energy splitting introduced by the J term for $J = -0.05\ K$ simply by calculating the difference between the eigenvalues of two states with different energy. One can obtain the value:

$$\Delta E(J = -0.05\ K) = 5.625\ K \tag{5.3}$$

Spin state			Slope (KT^{-1})
$\left|\frac{+15}{2}, \frac{+15}{2}, \frac{+15}{2}\right\rangle, \left|\frac{-15}{2}, \frac{-15}{2}, \frac{-15}{2}\right\rangle$			-84.375
$\left|\frac{+15}{2}, \frac{-15}{2}, \frac{+15}{2}\right\rangle, \left|\frac{-15}{2}, \frac{-15}{2}, \frac{+15}{2}\right\rangle,$	$\left|\frac{+15}{2}, \frac{+15}{2}, \frac{-15}{2}\right\rangle, \left|\frac{-15}{2}, \frac{+15}{2}, \frac{-15}{2}\right\rangle,$	$\left|\frac{+15}{2}, \frac{-15}{2}, \frac{-15}{2}\right\rangle, \left|\frac{-15}{2}, \frac{+15}{2}, \frac{+15}{2}\right\rangle$	28.125

Table 5.4: Spin ground states of the 3Dy system as a function of an increasing Heisenberg coupling within the effective model.

Heisenberg coupling and magnetic field

Now including a strong anisotropy term and an external magnetic field, it is possible to plot the energy eigenvalues by applying B along the three Cartesian axes, as done in figure 5.10.

The trends are similar to those seen in figures 5.5, 5.6 and 5.7 for anisotropy value of $D = -10\ K$, in the three directions of the field, but now a further contribution, given by the coupling between the spins, leads to a splitting of the $\left|\frac{+15}{2}, \frac{+15}{2}, \frac{+15}{2}\right\rangle$ and $\left|\frac{-15}{2}, \frac{-15}{2}, \frac{-15}{2}\right\rangle$ states, degenerates, with respect to the other energy states, opening a gap of the same value as shown in the equation 5.3.
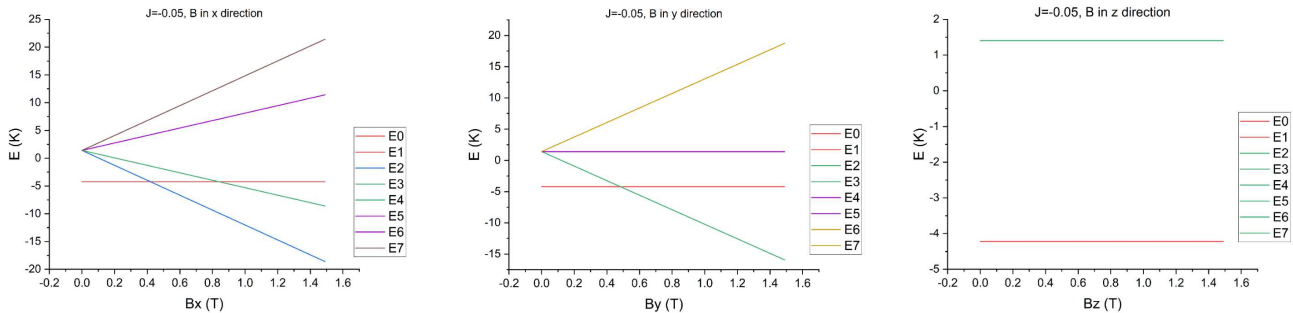
Figure 5.10: First 8 eigenvalues as a function of the intensity of the magnetic field oriented in three directions along the three axes, showing the degeneracy of each state.

So for sufficiently low field values, spin $\left|\pm\frac{15}{2}, \pm\frac{15}{2}, \pm\frac{15}{2}\right\rangle$ configurations will be found in the lower energy levels. However, the situation is changed by increasing the value of the magnetic field, leading to a level crossing and thus a variation of the lower energy states. Taking the case in which B is directed along x as an example, state $\left|\pm\frac{15}{2}, \pm\frac{15}{2}, \pm\frac{15}{2}\right\rangle$ will be in the ground state up to values of B approximately equal to $0.4\ T$, and then prefer state $\left|\frac{-15}{2}, \frac{+15}{2}, \frac{+15}{2}\right\rangle$, in which the spins will tend to point more in the direction of the magnetic field itself, as far as allowed by the anisotropy (see last row of table 5.3).

A similar behaviour can be observed if the field is directed along the y axis, following the same arguments as above. If, on the other hand, B is perpendicular to the plane of the ions, i.e. in the z direction, it will have no effect on the energy eigenvalues, which will be constant as B varies and divided by the Heisenberg term into two energy levels with degeneracy 2 and 6. Note, however, the difference between the right-hand graph in figure 5.10, and the graph for $D = -10\ K$ in figure 5.7. In the first case there is a splitting due to the J term, as just described, while in the second case the 8 eigenvalues are degenerate in the ground state, and the gap visible in the graph relates to the difference in energy between the degenerate low-energy octet and the excited states, separated by an energy value proportional to the constant D.

General B field on xy plane

For the sake of completeness, we also present the results obtained by applying a magnetic field in the xy plane, containing the three dysprosium ions, but with different orientations to those discussed above, i.e. along the x and y axes. Calling ϕ_B the azimuthal coordinate of the magnetic field in the plane, the energy spectra obtained for some different angles are shown in the figure 5.11. The angles chosen range from 0 to 180°, since for higher values, the magnetic field lies along the same directions but with opposite sign, so the same energy patterns are found, where however the different lines refer to spin states with opposite sign. In addition, as anticipated in figure 5.1, the C3 symmetry of the molecule makes it possible to study the eigenvalues for angles of B between 0 and 60°, then finding the same energy pattern for higher rotations.

Given again the symmetry of the molecule, the spin arrangement in states $\left|\pm\frac{15}{2}, \pm\frac{15}{2}, \pm\frac{15}{2}\right\rangle$ leads to a zero total magnetic moment, so interaction with the magnetic field will not produce any Zeeman term. This happens regardless of the direction of the field, thus resulting in two horizontal energy lines with degeneracy 2. Mathematically, this can be shown by explicitly calculating the Zeeman term as the sum of the scalar products between magnetic field and spin vectors. For spin orientations of 0°, 120° and 240° and for a magnetic field of modulus B and azimuthal coordinate φ_B, and neglecting the constants, one can write:
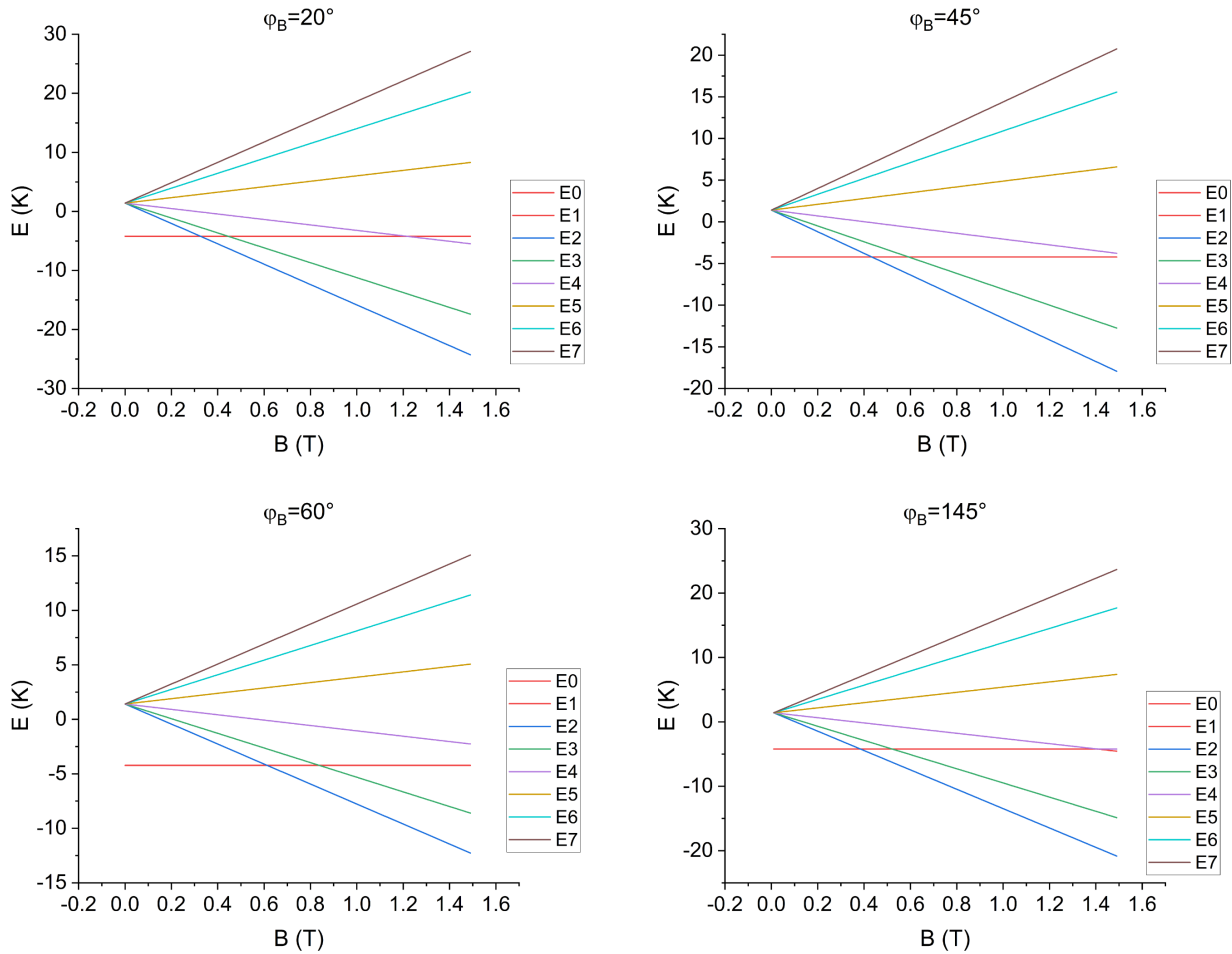
Figure 5.11: Eigenvalues of the 3Dy molecule applying a magnetic field of different intensities for different azimuthal directions in the xy plane.

$$\sum_{i=1,2,3} \boldsymbol{B} \boldsymbol{S}_i = \begin{pmatrix} Bcos(\varphi_B) \\ Bsin(\varphi_B) \end{pmatrix} \cdot S_1 \begin{pmatrix} 1 \\ 0 \end{pmatrix} + \begin{pmatrix} Bcos(\varphi_B) \\ Bsin(\varphi_B) \end{pmatrix} \cdot S_2 \begin{pmatrix} -1/2 \\ \sqrt{3}/2 \end{pmatrix} + \begin{pmatrix} Bcos(\varphi_B) \\ Bsin(\varphi_B) \end{pmatrix} \cdot S_3 \begin{pmatrix} -1/2 \\ -\sqrt{3}/2 \end{pmatrix}$$

$$= S_1 cos(\varphi_B) - \frac{S_2}{2} cos(\varphi_B) + S_1 \frac{\sqrt{3}}{2} sin(\varphi_B) - \frac{S_2}{2} cos(\varphi_B) - S_3 \frac{\sqrt{3}}{2} sin(\varphi_B)$$

$$= 0$$

Where the result is zero for $S_1 = S_2 = S_3$ and regardless of the choice of φ_B.

5.4 Tilting polar and azimuthal angles

Having understood how to interpret the spectrum of the eigenvalues by including the different terms of the Hamiltonian, it is possible to take a step further by moving slightly away from the ideal configuration and observe the behaviour of the system for a more general first case. In particular, as seen in chapter 4, the experimental data of the 3Dy molecule can be described by a model in which the spin vectors remain separated from each other by 120° along the *phi* component, while being tilted with respect to the ions´ plane by the same angle *theta* $\neq$ 90°.

To approach the experimental case, therefore, one can plot the set of eigenvalues as done so far

by considering different *umbrella angles* for the spin inclinations. The results for a field along the x and y components are shown in figure 5.12.
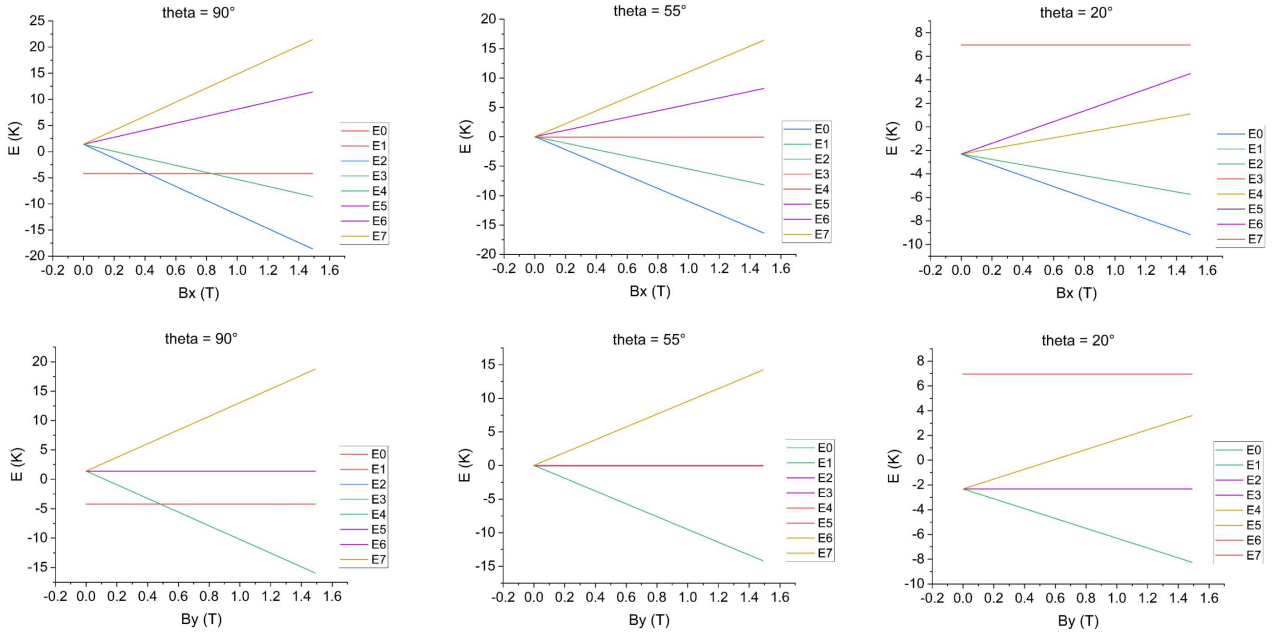

Figure 5.12: First 8 eigenvalues as a function of the intensity of the magnetic field oriented along x and y for different theta angles configurations.

In both directions of the magnetic field, it can be seen that the structure of the eigenvalues corresponding to states with mixed signs (inclined lines) is similar to the one obtained in the case of the ideal configuration. There is then a slight decrease in the slopes of the lines as *theta* angle decreases, due to the reduction of the cosine between the (fixed) magnetic field vector and the spin vectors. The most noteworthy variation, however, is related to the states $\left| \pm\frac{15}{2}, \pm\frac{15}{2}, \pm\frac{15}{2} \right\rangle$, whose energy level, given by the horizontal line in the graph, increases in energy as the theta angle decreases, crossing the other rows of eigenvalues from bottom to top.

As one may recall, the splitting between states $\left| \pm\frac{15}{2}, \pm\frac{15}{2}, \pm\frac{15}{2} \right\rangle$ and the other mixed-sign states is related to the Heisenberg coupling term, given by the relation $- \sum_{i,j} J_{i,j} \mathbf{S}_i \cdot \mathbf{S}_j$. From the graphs, it is clear how this term decreases as *theta* decreases until it reaches a value of about $55°$, where it is zero, and then increases again as *theta* decreases. This phenomenon, depending on the coupling term, is linked to the value of the scalar product between the spin vectors, and thus in particular to the angle formed between them. With this in mind, it is possible to analytically calculate the value of *theta* for which state $\left| \pm\frac{15}{2}, \pm\frac{15}{2}, \pm\frac{15}{2} \right\rangle$ starts to be at a higher energy than the other states of the octet. To do this we can consider two spin vectors, which can be written in Cartesian coordinates as a function of theta and phi angles as:

$$\mathbf{s}_1 = s_1 \begin{pmatrix} cos(\varphi_1)sin(\theta_1) \\ sin(\varphi_1)sin(\theta_1) \\ cos(\theta_1) \end{pmatrix} \qquad \mathbf{s}_2 = s_2 \begin{pmatrix} cos(\varphi_2)sin(\theta_2) \\ sin(\varphi_2)sin(\theta_2) \\ cos(\theta_2) \end{pmatrix} \qquad (5.4)$$

and so, taking the scalar product between the two vectors, choosing $(\theta_1, \phi_1) = (\theta, 0)$ and $(\theta_2, \phi_2) = (\theta, 120)$ and neglecting the modulus of the vectors, one can find:

$$\mathbf{s}_1 \cdot \mathbf{s}_2 = \begin{pmatrix} sin(\theta) & 0 & cos(\theta) \end{pmatrix} \cdot \begin{pmatrix} -\frac{1}{2}sin(\theta) \\ \frac{\sqrt{3}}{2}sin(\theta) \\ cos(\theta) \end{pmatrix} = cos^2(\theta) - \frac{1}{2}sin^2(\theta) \qquad (5.5)$$

which assumes a null value for $\theta = 54.7356°$. This value is well known in the literature, and usually referred as *magic angle*.

By multiplying the function obtained by the appropriate constants, its behaviour can be graphed, as done in the left figure of 5.13. The figure on the right shows the energies of the eigenvalues of the six states in the absence of a magnetic field; the difference in energy between the two states can then be compared with the function derived above, and with the graph on the left of the same figure.
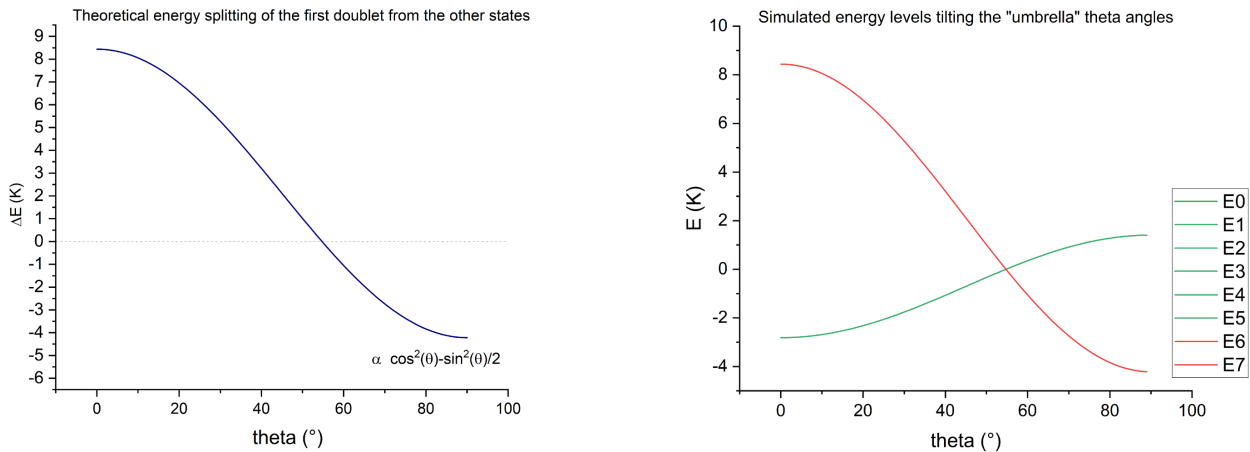
Figure 5.13: Energy splitting between the doublet ground state and the other six states (on the left) and energy eigenvalues (on the right) as a function of the theta angle of tilting of the spin vectors with respect to the ions´plane.

In the graphs just shown, it can be seen that for angles above 54.7° there is a crossing and exchange of the eigenvalues between the doublet and the remaining 6 energy levels, leading the $\left|\pm\frac{15}{2},\pm\frac{15}{2},\pm\frac{15}{2}\right\rangle$ configurations to higher energy. A similar behaviour is also found in the energy eigenvalues when applying a magnetic field along the z direction, and, in figure 5.14, it can be verified how the energy lines of states $\left|\pm\frac{15}{2},\pm\frac{15}{2},\pm\frac{15}{2}\right\rangle$ translate vertically, overlapping with the eigenvalues of the other octet states.

But the vertical application of the magnetic field leads to another interesting phenomenon. In fact, in the ideal configuration, the field would be perfectly perpendicular to the spin vectors, making no contribution to the Hamiltonian; but in this case, with umbrella angles slightly different from 90°, there is a non-zero interaction with the magnetic field, which will therefore give some Zeeman contribution. In particular then, the lowest-energy state will be split into two different states, just as the highest-energy line will go from degeneracy 6 to two split states of degeneracy 3.

The splitting of the lowest-energy state into the two states $\left|+\frac{15}{2},+\frac{15}{2},+\frac{15}{2}\right\rangle$ and $\left|-\frac{15}{2},-\frac{15}{2},-\frac{15}{2}\right\rangle$ thus has an important consequence; in fact in the degenerate case it would be feasible to derive from the result of a possible transition within the energy in the octet only information about the alignment of the spins and thus about the presence or absence of toroidicity. But with the introduction of a magnetic field, and thus splitting between the energy lines, it would hypothetically be possible to derive also the direction of a potential toroidal moment, thus knowing whether the vortex configuration of the spins is directed clockwise or counterclockwise with respect to a given chosen reference.
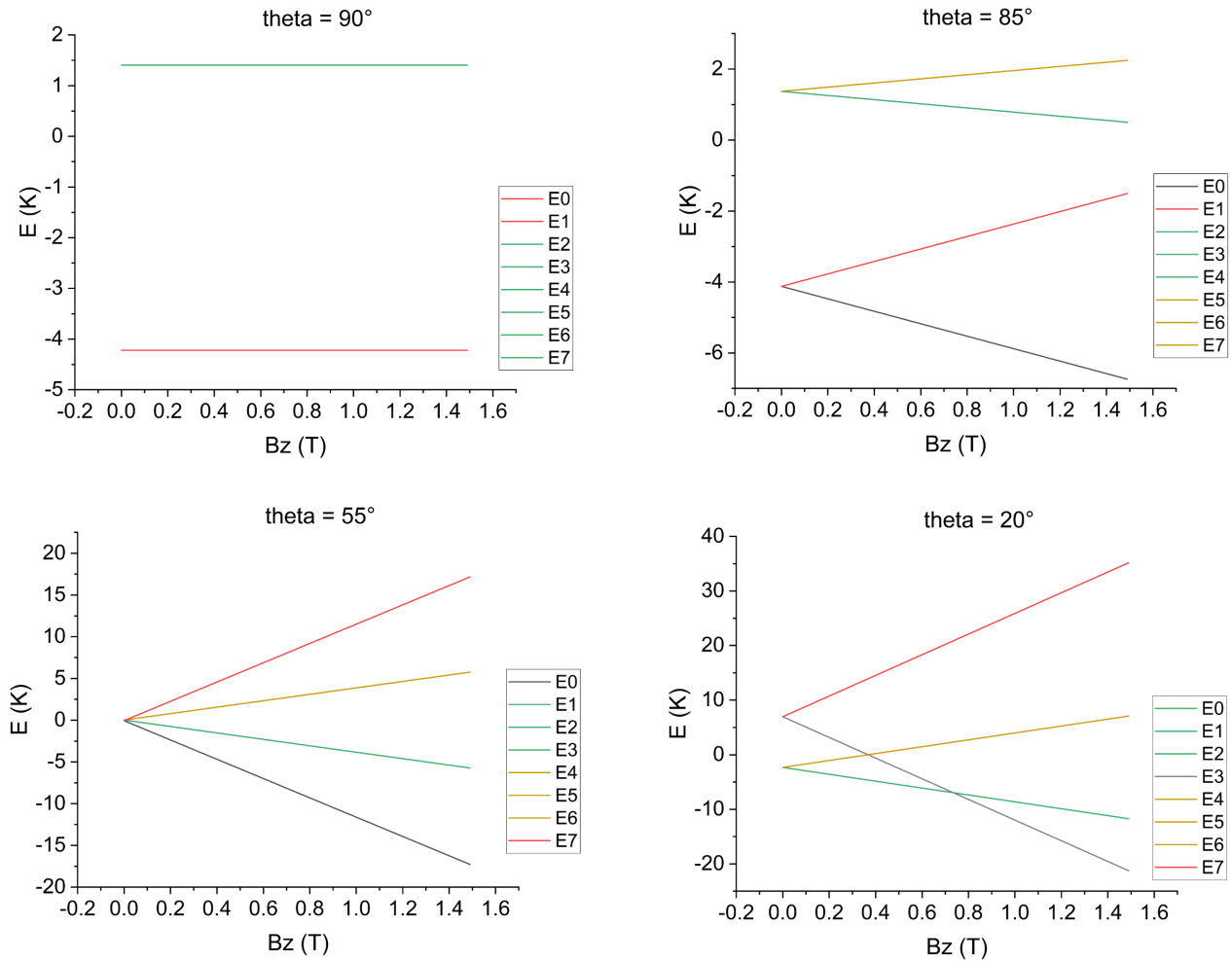
Figure 5.14: First 8 eigenvalues as a function of the intensity of the magnetic field oriented along z for different theta angles configurations.

5.5 Ferromagnetic coupling

The crossing and the exchange of eigenvalues between the doublet and the sextet suggests the possibility of inverting the sign of the Heisenberg coupling from an antiferromagnetic system ($J = -0.05\ K$) to a ferromagnetic one ($J = +0.05\ K$), resulting in the same energy configurations for pairs of angles that are 'symmetrical' with respect to the value at which splitting is null, i.e. 54.7°.

In order to further investigate this property, the low lying energy states are shown in figures 5.15, 5.16 and 5.17 by applying a magnetic field in the x, y and z direction, respectively. For each direction we consider 6 different cases: ferromagnetic coupling with $J = +0.05\ K$ or antiferromagnetic coupling with $J = -0.05\ K$, and polar angles theta equal to $theta \simeq 37.0777°, 54.73°, 80°$. These were chosen to have zero energy difference between doublet and sextet (for $theta = 54.73°$), and to have the same non-zero difference at $B = 0$ for the other cases; angles $theta = 37.0777°$ and $theta = 80°$ thus lead to the same separation between doublet and sextet at $B = 0$ in the ferromagnetic and antiferromagnetic cases.

The first thing that can be easily observed is how for $theta = 54.73°$ the ferromagnetic and antiferromagnetic configurations are perfectly superimposable, a sign that the system in this

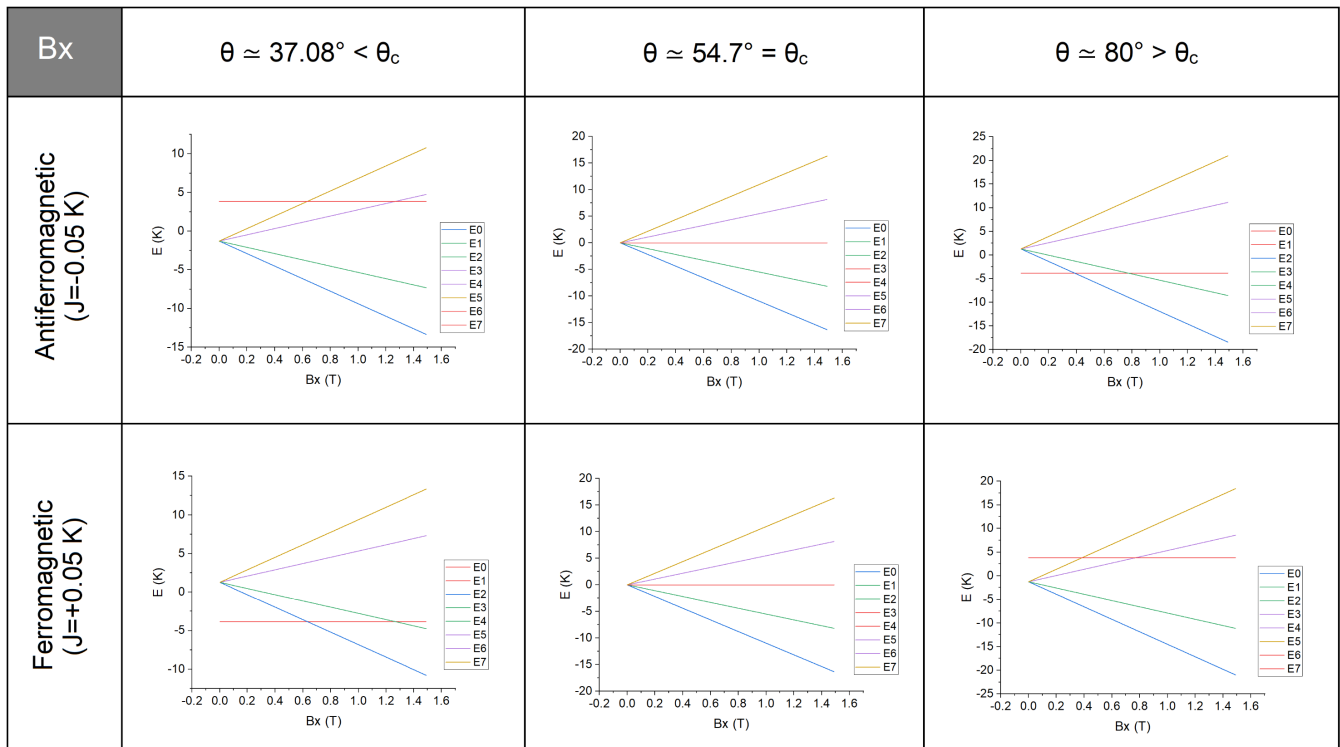Figure 5.15: Comparison of the energy spectra for different umbrella *theta* angles using a ferromagnetic and a antiferromagnetic coupling. Magnetic field applied on the x direction.

configuration has no preference in arranging the spins in a parallel or antiparallel manner.

On the other hand, for each magnetic field analyzed, the angles *theta* $\simeq 37.08°$ and $80°$ lead to two similar but not perfectly superimposable energy trends. In fact, in the case of the absence of a magnetic field, the splitting between the energy levels is identical in construction, but by increasing the value of B in a certain direction, the effect of the Heisenberg coupling, ferromagnetic or antiferromagnetic, leads to a slight difference in the splitting of the energy levels, a sign that the two configurations are not perfectly substitutable. This can also be seen by simulating the susceptibility and magnetization curves for such magnetic angles and couplings, which do not turn out to provide the same values.

Nevertheless, the sign of the Heisenberg coupling will have no influence on the value of the groundstate's toroidal moment (for a chosen *theta* configuration), thus allowing considerable toroidicity even in the ferromagnetic case. More details will be provided in Chapter 6.
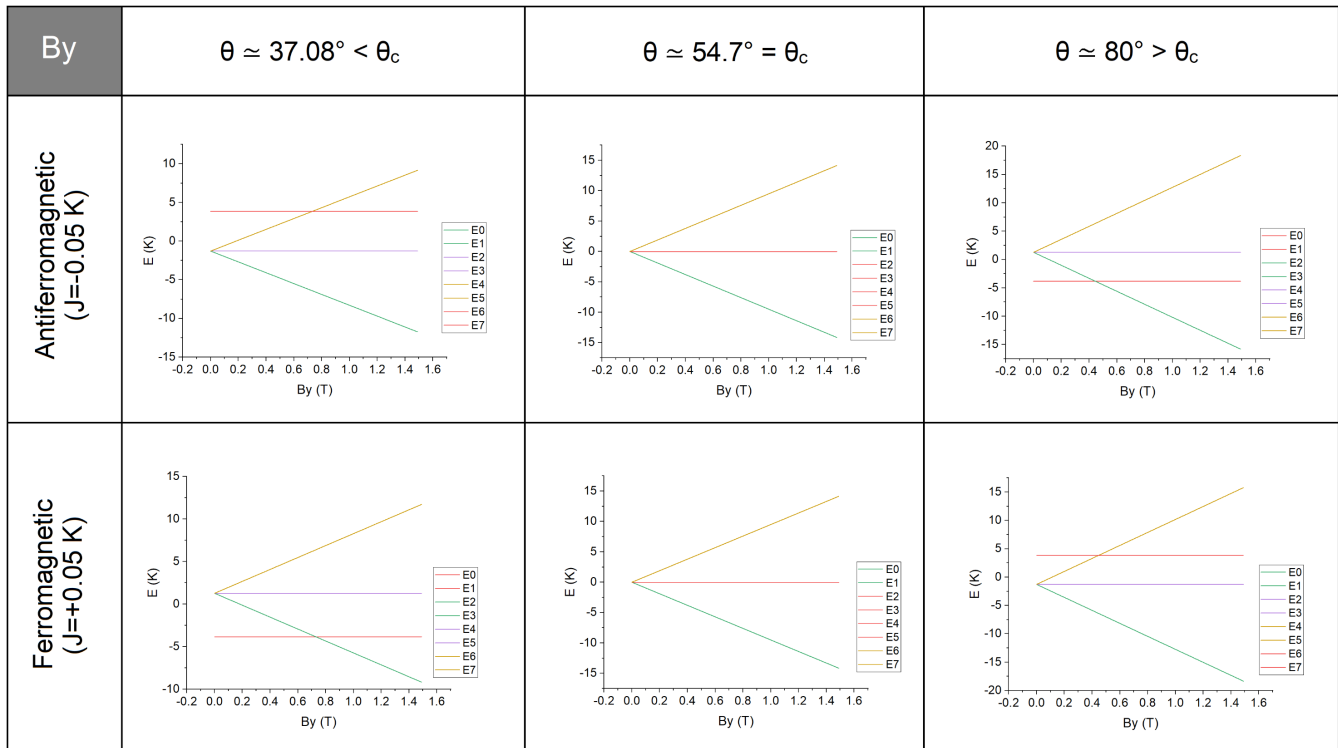
Figure 5.16: Comparison of the energy spectra for different umbrella *theta* angles using a ferromagnetic and a antiferromagnetic coupling. Magnetic field applied on the y direction.
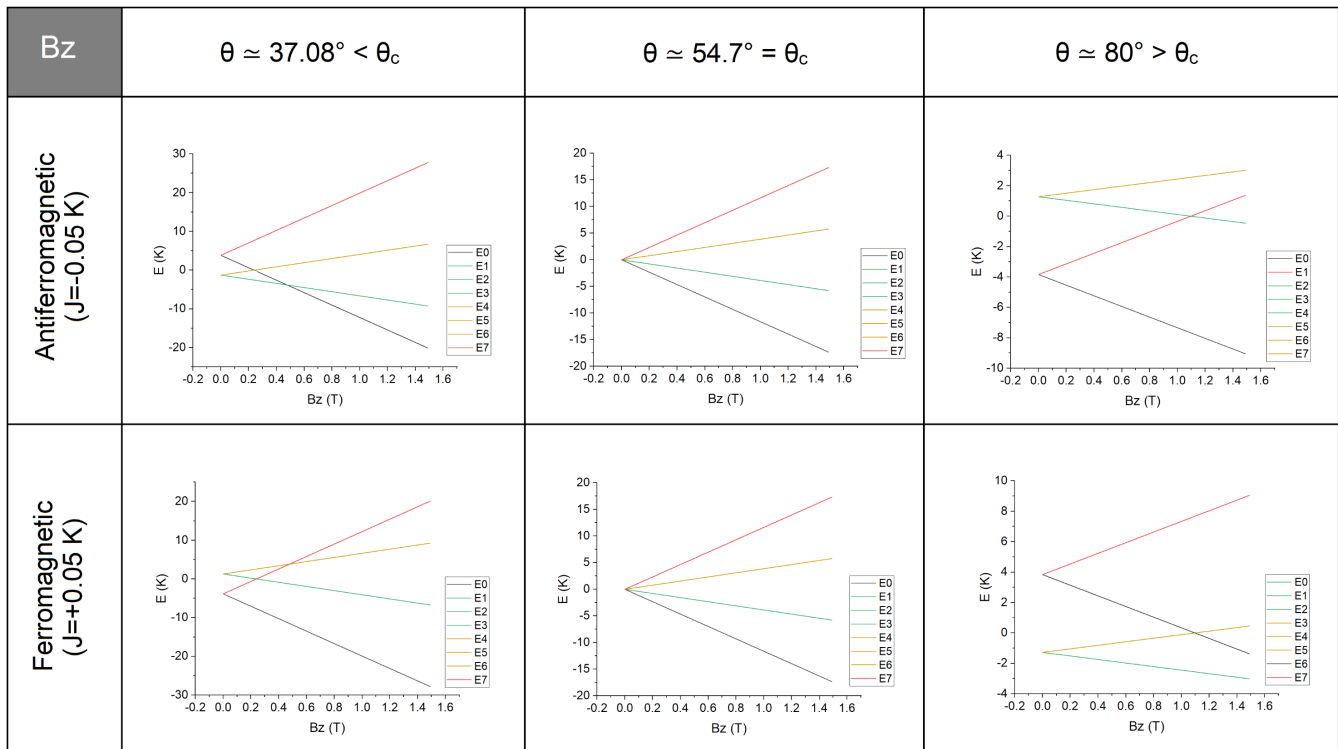

Figure 5.17: Comparison of the energy spectra for different umbrella *theta* angles using a ferromagnetic and a antiferromagnetic coupling. Magnetic field applied on the z direction.

Chapter 6

Toroidicity: quantitative description

6.1 Ideal configuration and choice of the coordinate frame

In the previous chapters, we explored the properties of the *3Dy* molecule in an ideal configuration. The ions are arranged at the vertices of an equilateral triangle and the axes of anisotropy are rotated by an angle of 120° to each other in the ions´plane, so as to fully respect a *C3* symmetry. Of these properties, only the orientation of the anisotropy axes had an influence on the energy spectrum, as the used Hamiltonian model has no dependence on the position of the ions, considering only spin interactions. Conversely, the position vectors of the ions appear in the definition of the toroidal moment, and thus a variation of the toroidal moment vector is expected for different reference systems or ion configurations. It was therefore decided to start the analysis with the ideal configuration, arranging the triangle of ions in such a way that its axis coincides with the z axis of the reference system, and thus the origin coincides with the centre of the triangle. In addition, for convenience, one of the ions is placed along the y axis, at zero x coordinate, while the other two are positioned at the other vertices of the equilateral triangle. The geometrical scheme can be seen in figure 6.1.
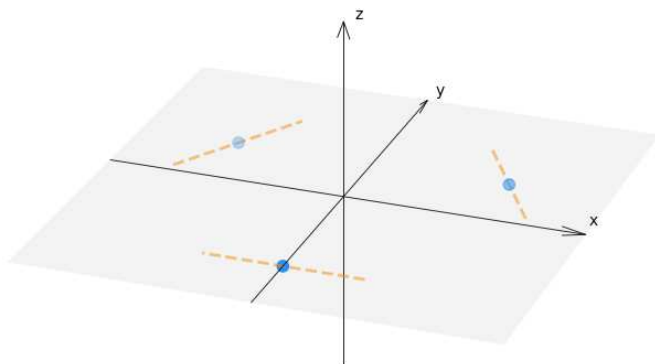
Spin	Coord. ($\mathring{A}$)	phi
S1	(0, -2.5, 0)	0°
S2	(2.16507, 1.25, 0)	120°
S3	(-2.16507, 1.25, 0)	140°

Table 6.1: Scheme of Dy ions positioning within the choice of the coordinate frame and representation of the anisotropy axes.

From this configuration, it is then possible to calculate the toroidal moment using the equation seen in section 2.4. Particular attention is paid, as usual, to the ground state, where the spins, in the high anisotropy approximation, are aligned with the anisotropy axes. In the previous chapter (chap. 5), in fact, it was seen how a semiclassical description of the system, considering the spins as vectors of modulus 15/2 directed along the anisotropy axes, allows a sufficiently accurate interpretation of the energy levels. Another confirmation of the goodness of this simplification

can also be found in the calculation of the toroidal moment, comparing the result of the quantum computation obtained by simulation, with its analytical counterpart obtained by semiclassical calculation.

Thus, for the ideal configuration with anisotropy axes having the same polar angle theta, the semiclassical analytical calculation of the toroidal moment for the ground state $\left|+\frac{15}{2}, +\frac{15}{2}, +\frac{15}{2}\right\rangle$ returns:

$$\boldsymbol{t} = \begin{pmatrix} 0 \\ 0 \\ 7.5 \cdot g \cdot \frac{15}{2} sin(theta) \end{pmatrix} \tag{6.1}$$

Which is thus a vector directed vertically, parallel to the z axis, and with a direction consistent with the orientation of the spin vectors. For $theta = 90°$, then, the z component will have value $+37.5\ \mu_B \mathring{A}$ ($-37.5\ \mu_B \mathring{A}$) for anticlockwise (clockwise) winding of the spins, looking at the coordinate frame having the feet on the origin of the reference system and the head along positive z.

Moreover, it follows from the definition that the toroidal moment is given by the sum of the three contributions relative to each of the three ions. And these contributions are equal in intensity, given the particular symmetrical configuration. Moving from the doublet $\left|\pm\frac{15}{2}, \pm\frac{15}{2}, \pm\frac{15}{2}\right\rangle$ to a state of the sextet, however, the flipping of one of the spins leads to a sign change in the contribution to the toroidal moment, perfectly cancelling out the equal contribution of one of the other two ions. It is therefore expected that the toroidal moment magnitude of the sextet will be $1/3$ of its value in the doublet, maintaining the same direction, namely a z component of $\pm 12.5\ \mu_B \mathring{A}$.

In this respect, one can then proceed to a quantum calculation by simulation, the results of which are shown in figure 6.1. The first line shows the two states that make up the doublet and maximise the toroidal moment, while the next two lines present the states of the sextet. The anisotropy axes, represented with an orange dotted line, are fixed and given as input to the simulation program, while the red arrows represent the average values of the spin vector operators.

It is clear that even in this case, the semiclassical model provides an effective explanation of the physics of the system, being able to neglect quantum interactions that appear not to contribute up to the 5th decimal place of the calculated quantities. In addition, the spin directions also overlap almost perfectly with the anisotropy axes, lending credence to the hypothesis made in the previous chapter.

Coordinate frame

In the semi-classical approach, it is therefore easy to obtain some results to understand the behaviour of the toroidal moment in specific cases. As emphasised above, the dependence of the toroidal moment on the coordinates of the ions necessitates a conscious choice of reference system. In particular, considering the ions arranged in the vertices of an equilateral triangle, their positions can be described by generic vectors:

$$\boldsymbol{r_1} = (0, -a, d) \quad \boldsymbol{r_2} = (b, c, d) \quad \boldsymbol{r_2} = (-b, c, d) \tag{6.2}$$

On the one hand, it is clear that a rotation of the system around the z axis does not produce any change in the value of the toroidal moment, since both position vectors and anisotropy axes follow the same transformation. However a translation of the system only leads to a change in the position vectors with a consequent change in the toroidal moment. Mathematically, one can then add a translation vector to each of the position vectors, obtaining the final coordinates:

$$\boldsymbol{r_1} = (0+\delta x, -a+\delta y, d+\delta z) \quad \boldsymbol{r_2} = (b+\delta x, c+\delta y, d+\delta z) \quad \boldsymbol{r_2} = (-b+\delta x, c+\delta y, d+\delta z) \tag{6.3}$$
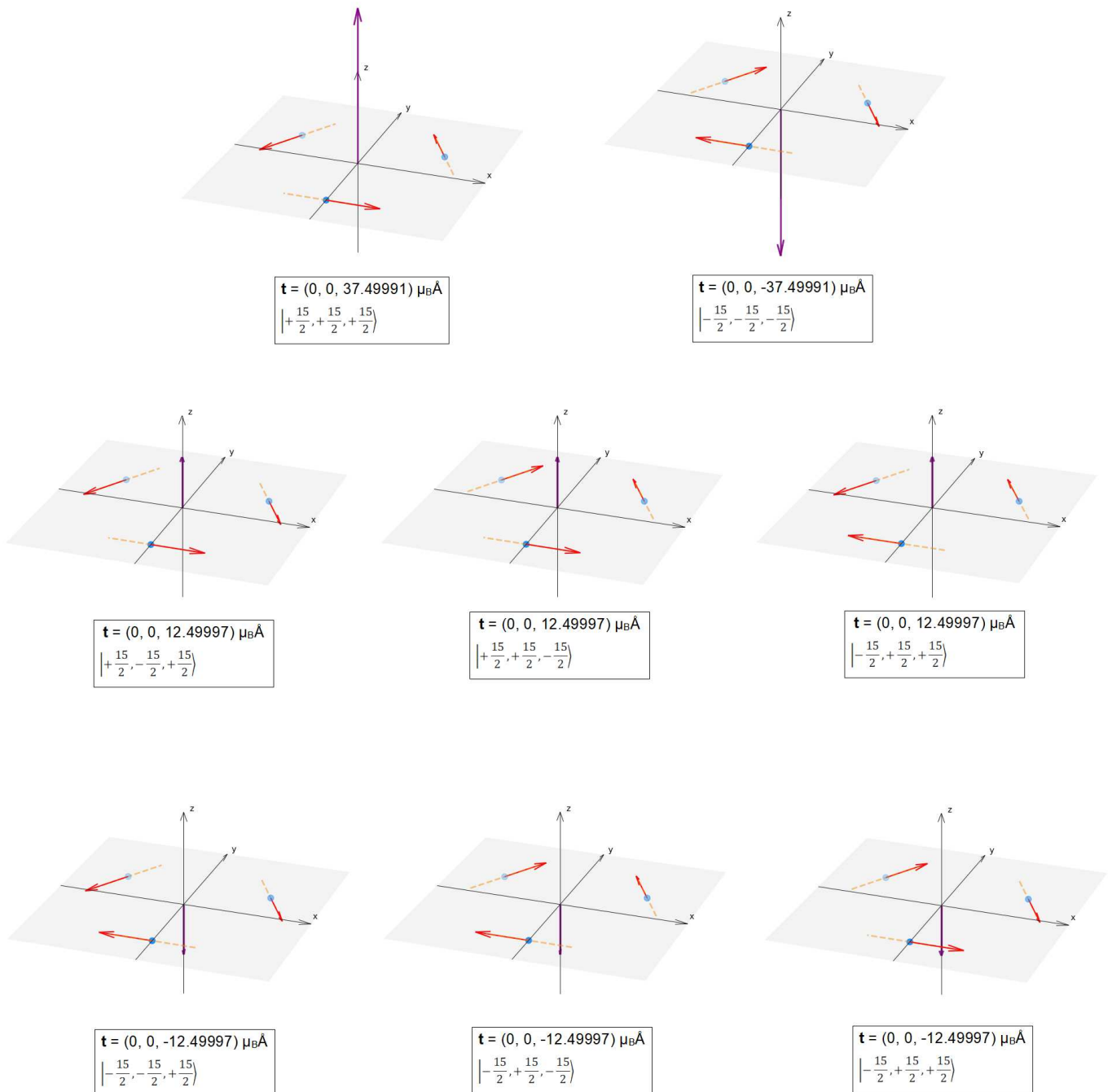
Figure 6.1: 3Dy low lying states toroidal moments for the ideal configuration. The anisotropy axes (dashed orange lines) are fixed and given as input to the simulation, while the red spin arrows are the result of the average spin operator in the considered state.

and from these follow the (positive) values of toroidal moment[1]:

$$
\begin{aligned}
\boldsymbol{t}_{|+,+,+\rangle} &\propto (0, 0, a + \sqrt{3}b + c) \\
\boldsymbol{t}_{|-,+,+\rangle} &\propto (0, -2d - 2\Delta z, -a + \sqrt{3}b + c + 2\Delta y) \\
\boldsymbol{t}_{|+,-,+\rangle} &\propto (\sqrt{3}d + \sqrt{3}\Delta z, d + \Delta z, a - \sqrt{3}\Delta x - \Delta y) \\
\boldsymbol{t}_{|+,+,-\rangle} &\propto (-\sqrt{3}d - \sqrt{3}\Delta z, d + \Delta z, a + \sqrt{3}\Delta x - \Delta y)
\end{aligned}
$$

As can be seen for doublet configurations, the toroidal moment is independent of the choice of reference system, hence of any translations, due to the particular symmetry of the system. However, by introducing an element of asymmetry, such as a flipping of a spin (or a variation of polar theta angles, discussed later) the toroidal moment can take on three different values that have dependence on the choice of reference system. The choice of the latter must therefore be considered, and it is reasonable to position the origin at the central point of the triangle in order to guarantee the rotational symmetry of the system.

6.2 Tilting polar *theta* angles

In section 5.4 we have shown the behaviour of the energy spectrum in the 8 low lying states by changing the tilting of the anisotropy axes (and consequently in the semiclassical model also the orientation of the spins) by varying each of the polar angles *theta*, in which was also called the "umbrella configuration".

The sextet and the doublet reduce then their energetic distance as the angle of theta decreases, until they overlap for $theta = 54.7°$, and then reverse their position at lower angles. Given the dependence of the toroidal moment on the spin vectors, a similar peculiar behaviour can be expected in this case as well.

Let us therefore consider the triangle of ions positioned in the ideal configuration (whose coordinates can be thought of as those expressed in equation 6.2 with $d = 0$). Let us then proceed to tilt the anisotropy axes (spin) by an angle theta with respect to the z axis. Proceeding analytically, the semiclassical calculation of the toroidal moment in this particular configuration gives the result:

$$
\begin{aligned}
\boldsymbol{t}_{|+,+,+\rangle} &\propto ((2c - a)\cos(theta), 0, (a + \sqrt{3}b + c)\sin(theta)) \\
\boldsymbol{t}_{|-,+,+\rangle} &\propto ((2c + a)\cos(theta), 0, (-a + \sqrt{3}b + c)\sin(theta)) \\
\boldsymbol{t}_{|+,-,+\rangle} &\propto (-a\cos(theta), 2b\cos(theta), a\sin(theta)) \\
\boldsymbol{t}_{|+,+,-\rangle} &\propto (-a\cos(theta), -2b\cos(theta), a\sin(theta))
\end{aligned}
$$

The first thing that can be noticed is the subdivision of the toroidal moments of the sextet into three different vectors. They have the same modulus, but are directed in different directions, separated by 120° from each other, and they assume the same coordinates again for $theta = 90°$. The toroidal moment of the doublet, on the other hand, remains unchanged in the direction, which always turns out to be parallel to the z axis (since in the particular triangular configuration assumed the term $(2c - a)$ is null). The modulus of the vector, on the other hand, decreases as *theta* decreases, following a sinusoidal function, and completely annihilates when the spins are perpendicular to the ions´ plane.

---

[1]Clarification on the notation: we are now focusing on the semiclassically describable case in which the spins are oriented along the axes of anisotropy. We therefore adopt the same notation used in the study of energy eigenvalues, in which each spin can take on the values $\pm 15/2$ (along its own axis of anisotropy). Therefore, the states of the doublet will be written as $\left|+\frac{15}{2}, +\frac{15}{2}, +\frac{15}{2}\right\rangle$ and $\left|-\frac{15}{2}, -\frac{15}{2}, -\frac{15}{2}\right\rangle$, depending on whether the spins are arranged anticlockwise or clockwise. In the states of the sextet, on the other hand, we have a flipping of one of the spins, hence a change of one of the signs in the notation. In order not to make the writing more cumbersome, sometimes the value 15/2 is omitted, and only the sign for the orientation of the spins are shown

As theta decreases, therefore, the modulus of the toroidal moment of the doublet decreases, while that of the sextet increases. Consequently for a given angle, there will be three possible toroidal moments of equal intensity. In the coordinates shown above, equating the moduli of the vectors, we can obtain that this angle is equal to:

$$\tilde{\theta} \simeq 35.2644° \simeq 90° - 54.7356°$$

The system has so three different toroidal moments of equal intensity when the *theta* angle is complementary to the analogous *theta* $= 54.7°$ in which the energy spacing between the sextet and doublet is zero.

In figure 6.2, some significant configurations are shown in a similar manner as before, showing the four different toroidal moment vectors for the four different spin states. For simplicity of representation only 4 of the 8 possible vectors are represented, while the other 4 will be aligned but in the opposite direction to those shown.

As can be seen, the toroidal moments of the sextet are "flattened" from parallel to the z axis for *theta* $= 90°$ to coplanar to the ion triangle for *theta* $= 0°$, and gradually increasing their modulus. The trend of this variation is summarised in figure 6.3, in which the coordinates of the toroidal moments of the sextet are plotted for different thetas (each point corresponds to a different value of theta) and in which the dimensions of the points in the graph are proportional to the modulus of the vectors.

The values of the moduli of the two vectors (sextet and doublet) are then plotted in the figure 6.4 by varying the value of *theta*; this curve is described, as mentioned above, by a sinusoidal function. We then highlight the angle for which all four toroidal moments assume the same intensity.

6.3 Ferromagnetic coupling

The toroidal moment is a geometric property that depends only on the position of the ions and the orientation of the spins (along the axes of anisotropy in the semiclassical view). There is so no dependence on the other parameters that make up the Hamiltonian, in particular a small external magnetic field and the Heisenberg coupling. In principle, therefore, both an antiferromagnetic coupling (as assumed so far) and a ferromagnetic coupling can lead to the same values of toroidal moment, as long as the approximation of strong anisotropy is valid and the model can be described in a semiclassical way. As explained in chapter 5, however, the choice of a ferromagnetic coupling leads to an inversion of the doublet and sextet of eigenvalues, thus having the eigenvalue with degeneracy 6 in the lowest energy state. The latter energy, however, corresponds to a maximum toroidal moment that is lower than that of the $|+, +, +\rangle$ or $|-, -, -\rangle$ states, so that in the case of ferromagnetic coupling, greater experimental difficulties would arise in the attempt to maximise the toroidal moment.

For the same reason of dependence only on the coordinates and on the spin orientations, even the presence of a small external magnetic field does not influence the toroidal properties of the molecule. In fact, an external magnetic field has been seen to remove the degeneracy of the energy levels, subdividing them in a "radial pattern" and thus assigning each spin configuration a different energy value.

But we have seen how different spin configurations lead to different toroidal moments, especially in the case of varying polar *theta* angles. So in the absence of a magnetic field the states are all degenerate, so it is equally probable to be in one or another spin configuration and therefore to have one or another value of toroidal moment. The presence of a magnetic field, however, with values of *theta* not equal to $90°$, divides the energy levels and therefore different will be
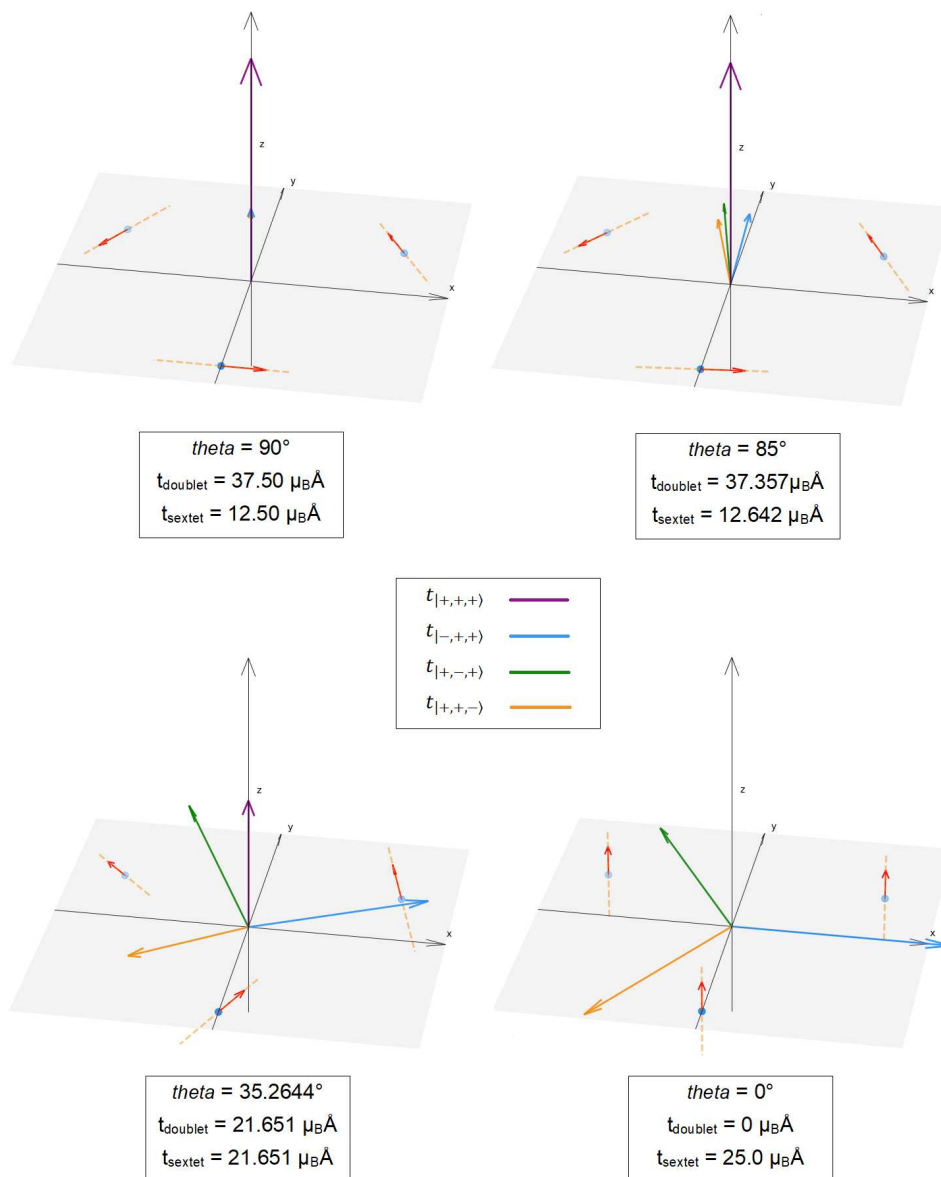
Figure 6.2: 3Dy low lying states toroidal moments for the ideal configuration tilting the "umbrella" polar *theta* angles of different values. The orientation of the spins along the anisotropy axes is purely indicative for ease of visualisation and refers to the case of one of the groundstate doublet states.

the probabilities of obtaining the different toroidal moments, where this probability can be interpreted as related to the Boltzmann factor. Qualitatively one can think of this phenomenon in a semiclassical manner noticing that the presence of the magnetic field will tend to align the greatest number of spins accordingly to its direction, but consistently with the strong anisotropy. Thus at low energies one will find configurations in which a greater number of spins "follow" the magnetic field, while at high energies the other configurations will remain.

6.4   High lying energy levels

The $3Dy$ molecule has 4096 different energy states, but so far we have focused on the low lying ones consisting of the first 8 energy levels. In these levels, in fact, the strong anisotropy allows the system to be analysed by considering spins of value $\pm 15/2$ oriented according to the angles of anisotropy, leading, precisely, to these 8 different configurations. However, going to higher
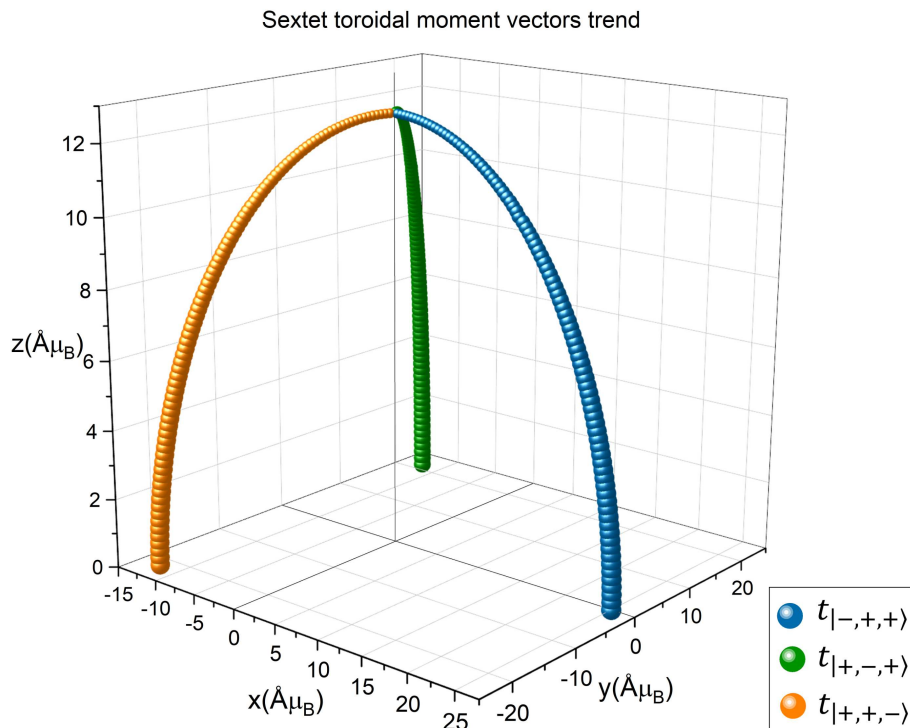
Figure 6.3: Coordinates of the three toroidal moment vectors of the sextet changing the *theta* angle from 90° to 0°. The size of the dots is proportional to the modulus of the vectors. (Values obtained by quantum simulation)
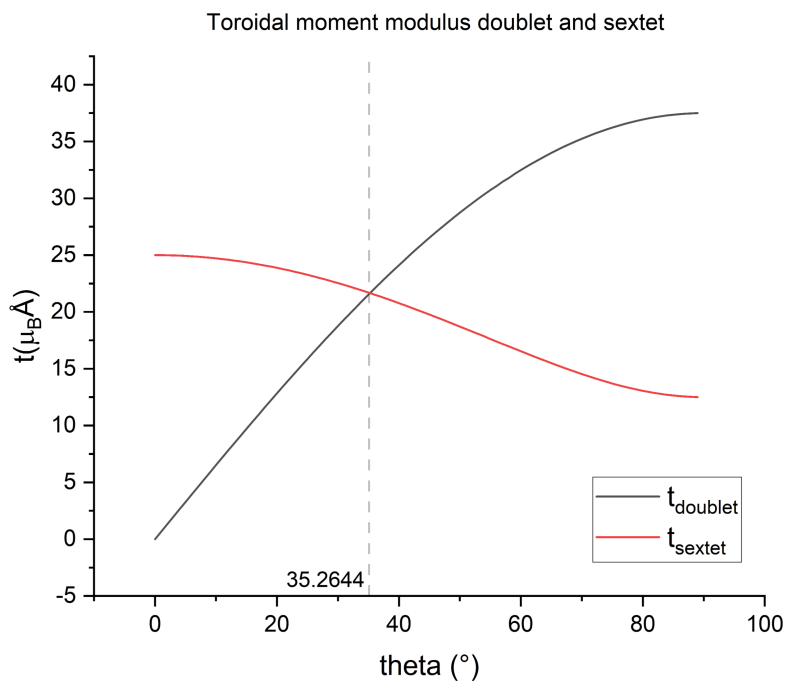

Figure 6.4: Modulus of the toroidal moment vectors of the doublet and of the sextet, with crossing between the two curves for the angle $\tilde{\theta} \simeq 35.2644°$. (Values obtained by quantum simulation)

energy levels, spin projections on the anisotropy axis other than $\pm 15/2$ are also admitted, and

thus mixed states that can only be described quantistically appear. It becomes clear, however, how the symmetry of the system is reduced due to the different possible spin orientations, so one can expect the toroidal moment to be reduced in modulus.

This is confirmed by the calculations shown in figure 6.5, in which the value of the toroidal moment of all the spin configurations related to the 4096 energy levels of the 3Dy molecule has been reported. The ideal configuration in the absence of external magnetic fields was used for the calculation.
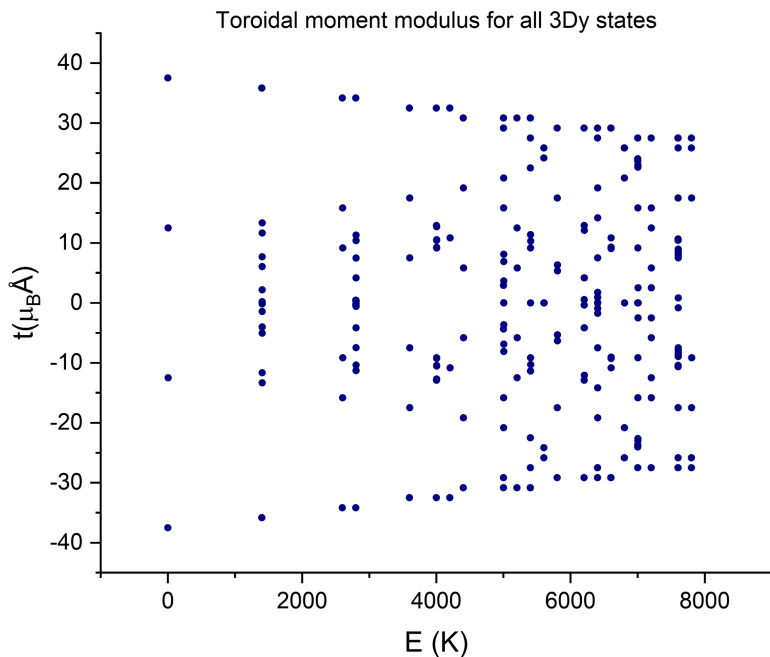
Figure 6.5: Modulus of the toroidal moment vectors for all the states of the 3Dy molecule as a function of the relative energy of the state.

As can be seen, the maximum values of the toroidal moment occur in the state at lower energies, while as the energy levels rise, there is a decrease in toroidicity, providing more "freedom of movement" for the spin.

6.5   Toroidicity of Al_2Dy_3

We have so far explored the properties of the toroidal moment by evaluating its dependence on various parameters. We can therefore now calculate its value for the molecule presented in chapter 3, i.e. the Al_2Dy_3. From the magnetization and susceptibility fits, we could only obtain the value of the parameter *theta*, but no information was obtained for the *phi* angles of the anisotropy axes. We can therefore assess the toroidal moment only by assuming some values for the *phi* angles, which are chosen as examples as those that maximise the toroidal moment, i.e. 0°, 120° and 240° in the usual frame of reference.

Figure 6.6 then shows the toroidal moment vectors for the doublet configuration (left) and for the sextet (right). As before, only one toroidal moment vector is represented, and its symmetrical is omitted for ease of visualisation.

The impossibility of determining *phi* angles from experimental data on magnetization and susceptibility therefore only allows us to analyse hypothetical cases, and we have no precise infor-
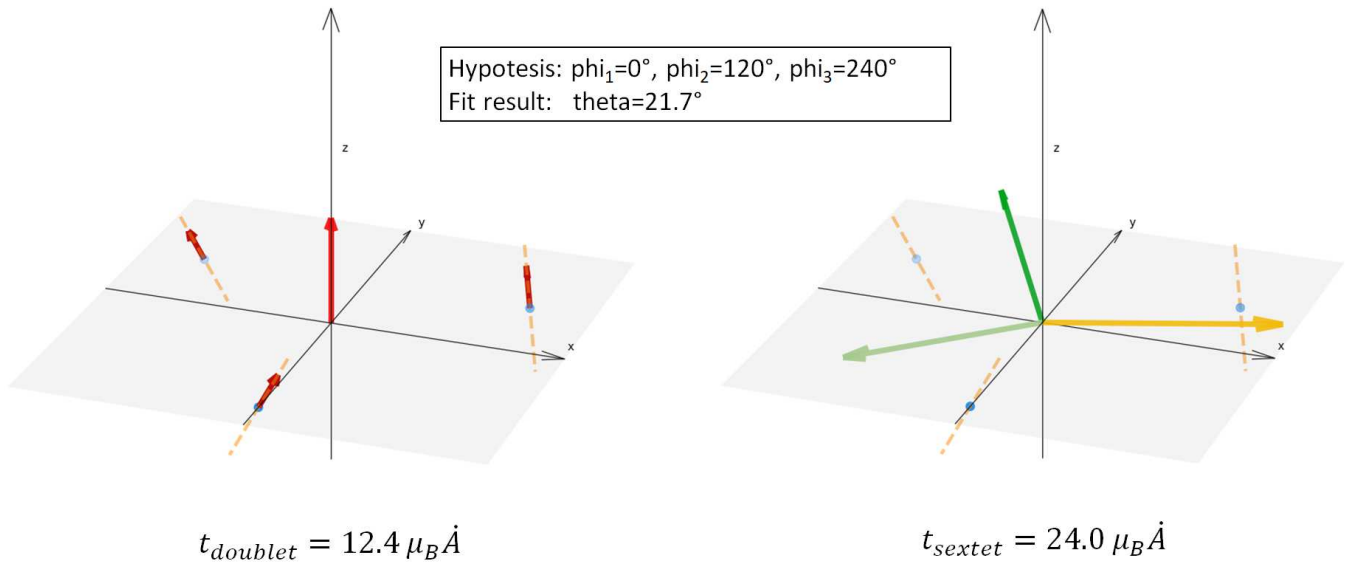
Hypotesis: phi$_1$=0°, phi$_2$=120°, phi$_3$=240°
Fit result: theta=21.7°

$$t_{doublet} = 12.4 \, \mu_B \dot{A}$$

$$t_{sextet} = 24.0 \, \mu_B \dot{A}$$

Figure 6.6: Toroidal moment vectors for the Al_2Dy_3, considering the *theta* angle found through the fit and in the hypothesis of ideal *phi* angles. On the left is shown the toroidal moment of the doublet, while on the right the ones of the sextet.

mation on the molecule being studied. In the case of different *phi* angles, in fact, the toroidal moment may decrease in magnitude, even to zero.

Different experimental techniques are therefore needed to obtain the full direction of the anisotropy axes, and thus also of the *phi* angles. The possibility of applying neutron scattering experiments will be investigated, and this will be shown in the following chapter.

Chapter 7

Inelastic Neutron scattering and toroidal moment

As discussed earlier, we would like to experimentally verify the orientation of the anisotropy axes of the three Dy ions, and, in particular, the values of the azimuthal angles *phi*, which cannot be obtained from the powder magnetization or susceptibility curves. The experiment considered is an inelastic neutron scattering, which has a dependence on the spatial coordinates of the ions, as can be seen in the exponential term of equation 2.5.3.

In the following, we will therefore show the results obtained by considering the Al_2Dy_3 molecule, first with a powder sample and then moving, out of necessity, to a single crystal sample.

7.1   INS on powder sample

8 low lying states: no transitions

We now want to simulate a neutron scattering experiment on a powder sample at $T = 0\ K$. By focusing on the 8 lowest energy states, we can verify the complete absence of transitions between any pair of states. This can be explained by resuming the arguments shown in section 5.2.

In a high anisotropy approximation, one can visualise the 8 low lying states as clockwise or counterclockwise spin configurations (doublet) and with the flipping of one of the spins (sextet), see figure 7.1. To have a transition between any two of these states requires a complete flipping of at least one of the spins, i.e. going from $+15/2$ to $-15/2$ (or vice versa). There would then be a change in the magnetic quantum number equal to $\Delta M = 15$, well above the limit imposed by the neutron scattering selection rules shown in equation 2.54, where $\Delta M = 0, \pm 1$.

So no information can be obtained by limiting oneself to the lowest energy levels.

For the sake of completeness, it should be pointed out that it was also possible to observe peaks of non-zero intensity among the 8 low lying states by significantly increasing the value of the anisotropy term E. In this way, however, the anisotropy contribution can no longer be thought of as axial, but three-dimensional components begin to appear. Consequently, it is no longer possible to describe the spin with only a $\pm 15/2$ value, but linear combinations of several states will be required, including the $\pm 13/2$ state with which a transition is possible. In any case, the intensities of the peaks obtained are extremely low, 10^7 times lower than those obtainable between the ground state and one of the high-energy states (see next paragraph). However, once again no useful information can be derived from such small peaks.
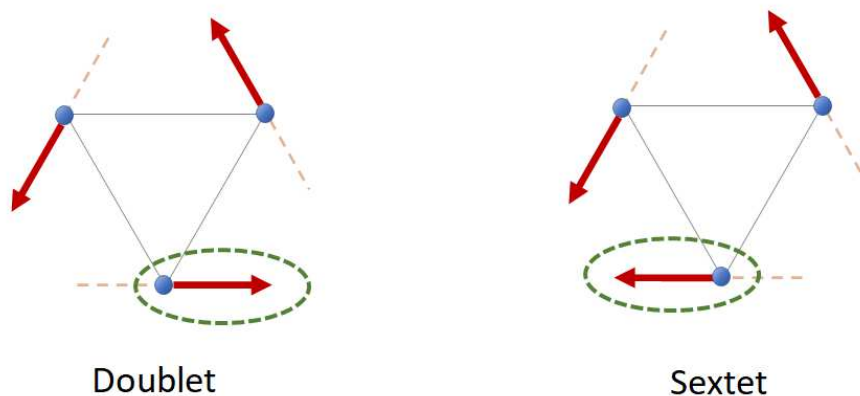
Figure 7.1: 3Dy spin configuration examples, one for the doublet state and one for the sextet state.

High lying states: no information on phi

Since no intensity peaks are visible within the 8 low lying states, one can extend the energy range and check for peaks of higher energy levels.

Considering a temperature $T = 0$ K, we can obtain two transitions from the ground state to the first and second of the high lying states. The observed transitions are highlighted in the spectrum of figure 7.2, on the left; while the same figure on the right shows the intensity peaks as a function of energy in the abscissa.
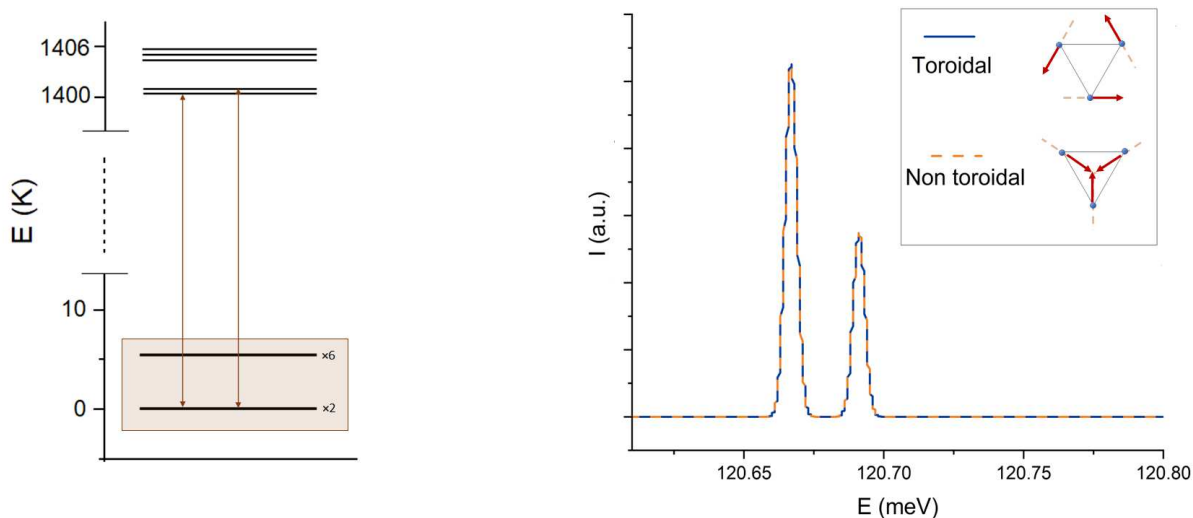

Figure 7.2: 3Dy Energy levels with the two observed transitions, on the left. Powder sample INS peaks of the observed transitions for two configurations of phi angles, for $T = 0$ K.

The same figure on the right actually shows the peaks for two different configurations of the molecule, in which the *phi* angles are varied. In particular, the configurations with the highest toroidicity and the one with zero toroidicity have been chosen.
It can be seen, however, that the intensity peaks are perfectly superimposable, an indication that no useful information on the *phi* angles, which we are interested in for the determination of the toroidal moment, can be derived from the INS powder sample.

But the powder sample analysed is a mixture of all possible orientations, so, in order to obtain information on the *phi* angles, it might be the case to perform an experiment in which orientations play a more important role. In the next section, we will therefore look more closely at the

inelastic neutron scattering on a single crystal sample.

7.2   INS on Single crystal

Let us now consider the inelastic neutron scattering on a crystalline sample. We will first derive a relation to calculate the intensity of the peaks, and then implement and test it in the *owIns* program. Finally, we will apply the new code to the Al_2Dy_3 molecule, in particular to the two intensity peaks seen in the powder sample.

7.2.1   Derivation of the intensity equation and implementation in owMag

In chapter 2, we examined and derived the relationship describing the intensity of scattering with a neutron as a function of the scattering vector $\mathbf{Q}$ and the m and n states between which the transition occurs. We also mentioned the possibility of integrating the relation in the $d\Omega$ parameter space to obtain the peak intensity for a powder sample.

However, we now need a similar relation to calculate the intensity in the case of a crystalline sample, which can be implemented in the *owIns* code. We can therefore rework equation 2.5.3 as follows:

$$
\begin{aligned}
I_{nm}(\mathbf{Q}) &= \frac{1}{4} \sum_{i,j} e^{i\mathbf{Q}\mathbf{R}_{i,j}} \sum_{\alpha,\beta} \left(\delta_{\alpha,\beta} - \frac{Q_\alpha Q_\beta}{Q^2} \right) \langle n| \left(\widehat{S}_i^\dagger \mathbf{F}_i(Q)\mathbf{g}_i \right)_\alpha |m\rangle \langle m| \left(\mathbf{g}_j \mathbf{F}_j(Q)\widehat{S}_j \right)_\beta |n\rangle \\
&\simeq \frac{1}{4} \sum_{i,j} F_i^{(0)}(Q) F_j^{(0)}(Q) e^{i\mathbf{Q}\mathbf{R}_{i,j}} \sum_{\alpha,\beta} \left(\delta_{\alpha,\beta} - \frac{Q_\alpha Q_\beta}{Q^2} \right) \langle n| \left(\widehat{S}_i^\dagger \mathbf{g}_i \right)_\alpha |m\rangle \langle m| \left(\mathbf{g}_j \widehat{S}_j \right)_\beta |n\rangle \\
&= \frac{1}{4} \sum_{i,j} F_i^{(0)}(Q) F_j^{(0)}(Q) e^{i\mathbf{Q}\mathbf{R}_{i,j}} \sum_{\alpha,\beta} \left(\delta_{\alpha,\beta} - \frac{Q_\alpha Q_\beta}{Q^2} \right) M_{i,\alpha}^\dagger M_{j,\beta} \\
&= \frac{1}{4} \sum_{i,j} F_i^{(0)}(Q) F_j^{(0)}(Q) e^{i\mathbf{Q}\mathbf{R}_{i,j}} \left[\sum_\alpha M_{i,\alpha}^\dagger M_{j,\alpha} - \left(\sum_\alpha \frac{Q_\alpha}{Q} M_{i,\alpha}^\dagger \right) \left(\sum_\beta \frac{Q_\beta}{Q} M_{j,\beta} \right) \right] \\
&= \frac{1}{4} \sum_{i,j} F_i^{(0)}(Q) F_j^{(0)}(Q) \left(\cos(\mathbf{Q}\cdot\mathbf{R}_{i,j}) + i\sin(\mathbf{Q}\cdot\mathbf{R}_{i,j}) \right) \left[\sum_\alpha M_{i,\alpha}^\dagger M_{j,\alpha} - \left(\sum_\alpha \frac{Q_\alpha}{Q} M_{i,\alpha}^\dagger \right) \left(\sum_\beta \frac{Q_\beta}{Q} M_{j,\beta} \right) \right]
\end{aligned}
$$

We have therefore neglected the second order of the form factors F by considering only the term F^0 which no longer depends on the directions $\alpha, \beta = x, y, z$. The matrix elements $\langle n| \left(\widehat{S}_i^\dagger \mathbf{g}_i \right)_\alpha |m\rangle$ have been defined as $M_{i,\alpha}$, and applying the Kronecker delta gives the result shown in the second last row. Finally, the complex exponential is expressed as the sum of cosine and imaginary sine, giving the final result.

As said previously in chapter 2, in general the result of this relation is a complex number, but in which the imaginary part should give a null value.

In this fashion, the relationship can be encoded in the *owIns* program, as an additional option to the usual calculation of neutron scattering intensity for powder samples. All terms in the relation are already calculated in the code, which also allows operations between complex numbers. Having completed the implementation, the next step is therefore to test the new functionality of the program, which is shown in the next section.

7.2.2   Validation of the coded formula

Testing the program, Cr^{3+} dimer

To test the program, it is possible to study a simplified case with respect to the $3Dy^{3+}$ molecule, so that the data obtained from the simulations can be compared with theoretical models. We

can consider, for instance a single crystal dimer made of two Cr^{3+} ions of total angular moment $S = \frac{5}{2}$ positioned along the x axes with coordinates (-2,0,0) and (2,0,0). The lower spin value with respect to Dy^{3+} reduces the dimension of the Hilbert space, decreasing the computation time of the simulations.

We can set in a strong exchange interaction condition, choosing a big ferromagnetic exchange coupling $J = 100\ K$ and a lower Ising-type anisotropy value $D = -5\ K$, with the anisotropy axes along the z axes ($theta = 0°$, $phi = 0°$). The chosen configuration has been summarised and depicted in fig. 7.3.
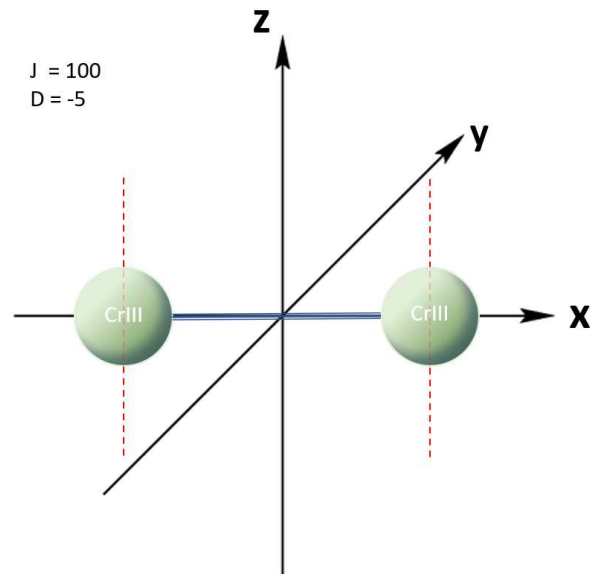
Figure 7.3: CrIII dimer configuration, antiferromagnetic Heisenberg coupling and Ising anisotropy parallel to the z axes.

Given that the simple structure of the molecule in question, it is easy to predict the energy spectrum and, consequently, the possible peaks visible through neutron scattering. As pointed out above, the two Cr ions have a total angular momentum $S = \frac{5}{2}$, which, following the rules of summation of angular moments, leads to a total angular momentum and its z projection given by:

$$S = S_1 + S_2 = |s_1 - s_2|, ..., |s_1 + s_2| = 0, 1, 2, 3, 4, 5$$
$$m = S, S - 1, ..., -S$$

Including only the exchange term, setting $D = 0\ K$, there will therefore be 5 degenerate energy levels, one for each total spin value. These levels will be further splitted by introducing the anisotropy term, which lifts the degeneracy; the energy scheme is shown in figure 7.4.

The presence of two magnetic ions therefore leads to two intensity peaks in the neutron scattering interactions at zero temperature, and these must satisfy the selection rules shown in equation 2.54. For a powder sample the INS peaks are plotted in figure 7.5, in which the relative energy values of the transitions obtained by means of neutron scattering were entered next to the peaks.

Given that the powder sample is produced by the random orientation of the molecules in the studied material, one can expect to find similar energy peaks for a single crystal sample as well. We can then proceed to simulate a neutron scattering experiment on a crystalline Cr^{3+} dimer using the new code, in which the Q_x, Q_y and Q_z components of the scattering vector must be specified in addition to the usual parameters. In this case we investigate the scattering vector in the range $Q_x \times Q_y = [-5; 5] \times [-5; 5]\ \mathring{A}^{-1} \times \mathring{A}^{-1}$, setting for now $Q_z = 0\ \mathring{A}^{-1}$. The results are
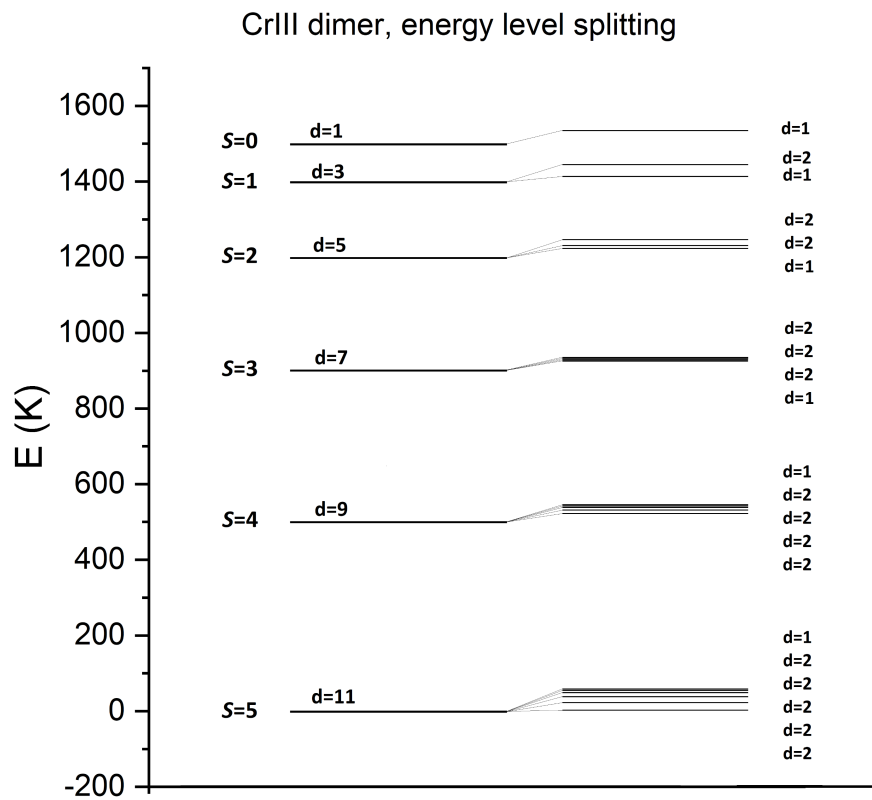
CrIII dimer, energy level splitting

Figure 7.4: Cr^{3+} dimer energy levels with their degeneracy. The levels on the left (calculated considering only the exchange coupling term) are splitted adding the anisotropy term, obtaining the ones in the right.
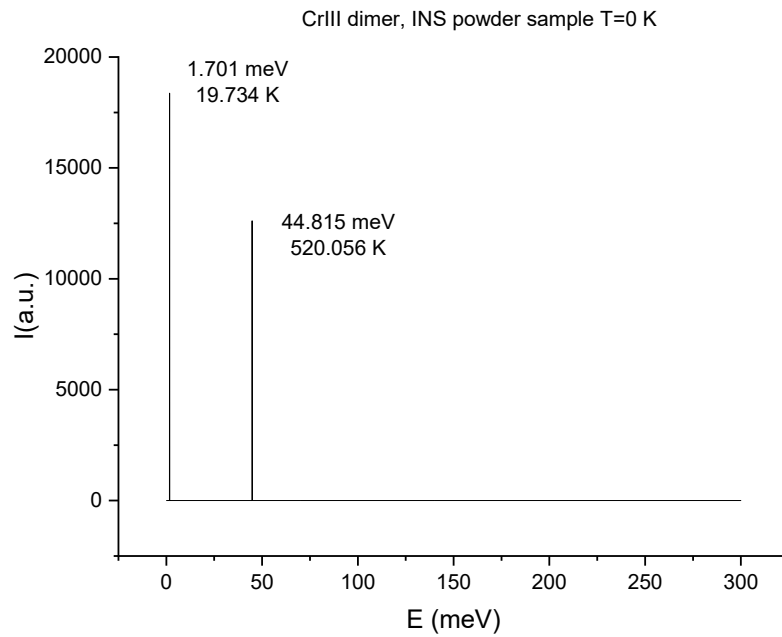
CrIII dimer, INS powder sample T=0 K

Figure 7.5: INS intensity peaks for Cr^{3+} dimer in powder sample at T=0 K.
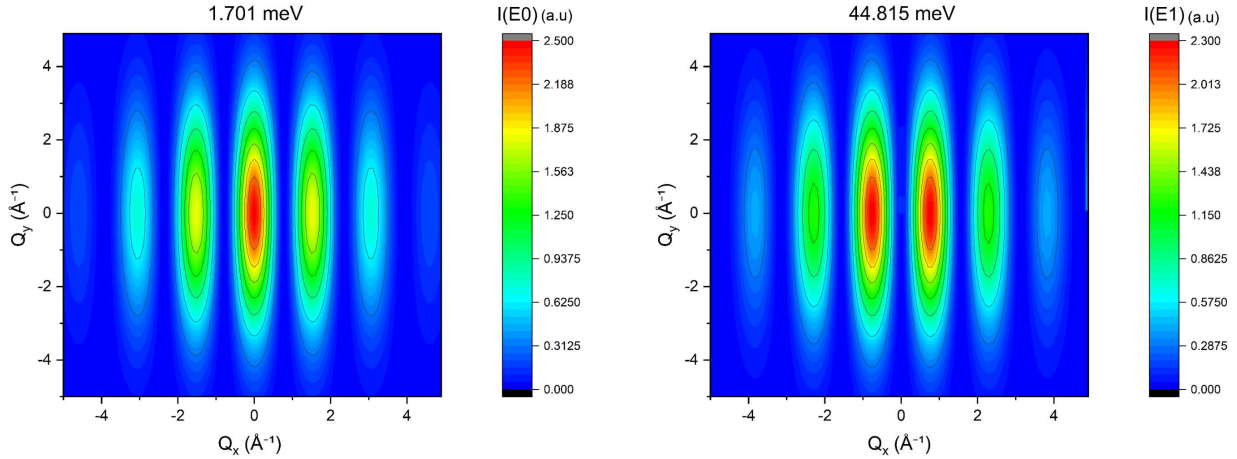
Figure 7.6: INS intensity peaks for Cr^{3+} dimer in single crystal sample at T=0 K.

shown in picture 7.6, in which the intensity of the scattered neutrons is plotted as a function of Q_x and Q_y for both energy peaks discussed above.

To check the reliability of the obtained results, it is possible to carry out similar simulations by excluding the presence of the form factor F (set equal to 1) in the formula of the INS. Retracing in fact what has been done in [22], it is possible to show that for a ferromagnetic cluster the INS formula for the intensity of a transition from the ground state to an excited state k is given by:

$$I_{0,k} = F_k(\mathbf{Q})\frac{1}{4}(2 - \kappa_x^2 - \kappa_y^2) \tag{7.1}$$

where $\kappa_\alpha = Q_\alpha/Q$ and the interference factor $F_k(\mathbf{Q})$ can be written as;

$$F_k(\mathbf{Q}) = \sum_{i,j} F_i F_j cos(\mathbf{Q}\mathbf{R}_{i,j})c_k(i)c_k(j) \tag{7.2}$$

where F_α is the form factor of the ion, while c_k can be seen as the classical amplitude of deflection of the spin from the polarization direction; so for the isotropic cluster under study it must hold $\sum_i c_k(i) = 0$. Moreover, as a consequence of the normalization condition of the eigenvectors, it is possible to obtain that $c^2 = s$, total spin of each ion ($s = 5/2$).

These conditions thus lead to two different possibilities:

– For the $\Delta S = 0$ selection rule it holds $c(1) = c(2) = s$, so:

$$F_k(\mathbf{Q}) = F^2 \left[s + s + scos(\mathbf{Q}\mathbf{R}_{1,2}) + scos(\mathbf{Q}\mathbf{R}_{2,1}) \right] = 2F^2 s \left(1 + cos(\mathbf{Q}\mathbf{R}_{1,2}) \right)$$

– For the $\Delta S = 1$ selection rule it holds $c(1) = -s$ and $c(2) = s$, so:

$$F_k(\mathbf{Q}) = F^2 \left[s + s - scos(\mathbf{Q}\mathbf{R}_{1,2}) - cos(\mathbf{Q}\mathbf{R}_{2,1}) \right] = 2F^2 s \left(1 - cos(\mathbf{Q}\mathbf{R}_{1,2}) \right)$$

Putting all the results together and substituting $s = 5/2$, we obtain the two relations that describe the intensity peaks for the two transitions of the Cr^{3+} dimer:

$$I_{0,k} = \frac{5}{2}F^2(1 + cos(\mathbf{Q}\mathbf{R})(\mathbf{Q})(2 - \kappa_x^2 - \kappa_y^2)$$
$$I_{0,k} = \frac{5}{2}F^2(1 - cos(\mathbf{Q}\mathbf{R})(\mathbf{Q})(2 - \kappa_x^2 - \kappa_y^2) \tag{7.3}$$

The form factor F is a value that depends on the ion species and makes it possible to modulate the intensity of scattering by considering magnetic interactions. To simplify the comparison between theoretical expectations and simulation results, it is convenient to disregard the form factor and set it to 1 in both cases, taking for granted the goodness of its calculation by means of code functions that have already been extensively tested. The same plots of figure 7.6 are then re-proposed in fig. 7.7 by setting $F = 1$ and placing the simulated values side by side with those obtained through equations 7.3.
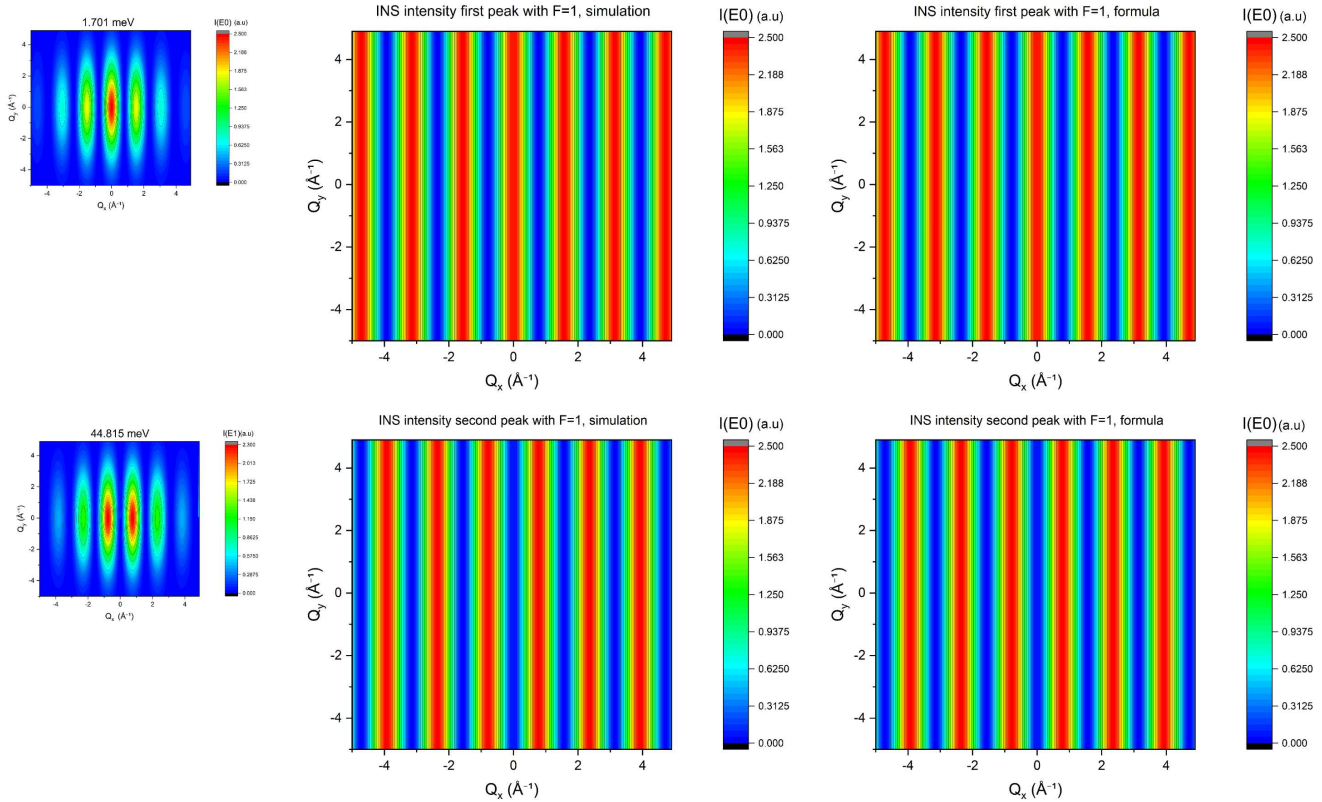

Figure 7.7: INS intensity peaks for Cr^{3+} dimer in single crystal sample at T=0 K setting the form factor F to 1. On the right the theoretical expectations are compared with the simulation results in the center, while on the left the full intensity plot is shown for completeness.

It is therefore easy to see that the two graphs obtained are perfectly superimposable, thus providing an initial confirmation of the good functionality of the code used.

In this section, we have analysed a particular case of a ferromagnetic dimer with anisotropy along the z-axis, finding a very good match between simulations and theoretical calculations; however, the particular configuration does not provide any information on the general functionality of the code, which can be further explored by considering rotations in the space of the dimer and the anisotropy. This will be therefore discussed in the next section.

Spatial rotations

In the previous tests, a particular symmetry of the dimer was adopted, placing the two ions along the x axis, mirrored with respect to the origin of the reference system, and with anisotropy axes along the z axis. As can be expected, however, the choice of reference system should not affect the simulation results, thus leading to the same intensity pattern suitably rotated with respect to the chosen representation. Figure 7.8 therefore shows the intensity patterns for the two energy transitions of Cr^{3+}, starting from the configuration described above and rotating the reference

system (or similarly the dimer) around the z axis by 45°, 90° and 135°, always keeping fixed the orientation of the anisotropy axes parallel to the z axis.

It is thus verified how rotations of the molecule in space do not affect the pattern of the neutron scattering, leaving its intensity and structure unchanged, and maintaining the robustness of the used formula.

Different representations are instead expected by changing the direction of the anisotropy axes, which, for example, can be positioned in the x-y plane on which the Cr ions lie. We have therefore decided to analyse the two $\hat{x}$ and $\hat{y}$ directions, initially placing the anisotropy axes along $\hat{x}$ and with the dimer axis first along $\hat{x}$ and then along $\hat{y}$. Similarly it is done with the anisotropy axes along $\hat{y}$. The results are shown in figure 7.9.

The same patterns are then obtained for the same orientations of the anisotropy axes with respect to the dimer axis, thus with the same configuration unless considering rotations in space. Whereas by changing the relational orientation of the anisotropy axes, a different pattern occurs, as expected.

Literature comparison

Given the success of the simple simulations carried out previously, it was decided to apply the code to a more complex molecule already studied in the literature. In [22], for example, a molecule consisting of 7 Mn ions was considered, and simulations of single crystal neutron scattering were carried out using *Mathematica* software.

The magnetic structure of the molecule consists of four Mn^{2+} ions and three Mn^{3+} ions, arranged hexagonally with a central ion at the origin of the reference system and with a mutual distance of $a = 3.31\,\mathring{A}$. The ions interact with each other via ferromagnetic and antiferromagnetic Heisemberg couplings, while possible anisotropy terms are neglected. The values of the interaction constants are: $J_a = J_b = 5.8\,K$, $J_1 = -2.0\,K$ and $J_2 = 2.45\,K$, and the structure of the molecule is shown in figure 7.10.

Analysing the molecule via single crystal INS, focusing on the x-y plane where the ions are positioned, four intensity peaks are detected, and they correspond to energies equal to those obtained in the article, i.e. equal to 0.3, 1.16, 3.44, and $4.84\,meV$.

Therefore, for each scattering peak, it is possible to obtain an intensity map in the reciprocal $Q_x - Q_y$ space, and thus compare the patterns obtained. The graphs in the article (top row) are then shown in figure 7.11 and compared with the corresponding graphs calculated using *ow_ins* (bottom row), trying to reproduce a similar plot range and colour scale. The latter was normalised for each plot in order to evaluate the same intensity range.

As can be seen, disregarding the non-identical graphical choices, the different plots show overlapping patterns, reconstructing the result of the INS congruently with what was done in the article. Therefore, from the result obtained and the preceding ones, we can rely on the code working well, which can thus be applied to the molecule under investigation.

7.2.3   Single Crystal INS on Al_2Dy_3 molecule

We can now use the recently implemented code to simulate an experiment with the Al_2Dy_3 molecule. The two peaks seen in figure 7.2, for a powder sample, are also found in the single crystal case. But now we no longer plot the intensity as a function of energy, but focus on the two energy values that have peaks and graph the intensity of the transition as a function of the scattering vector $\mathbf{Q}$. In particular, since the ions are positioned in the $x - y$ plane, we choose to display the x and y components of the scattering vector. The result, initially obtained in the ideal configuration ($theta = 90°$, $phi1 = 0°$, $phi2 = 120°$, $phi3 = 240°$,) is shown in figure 7.12.

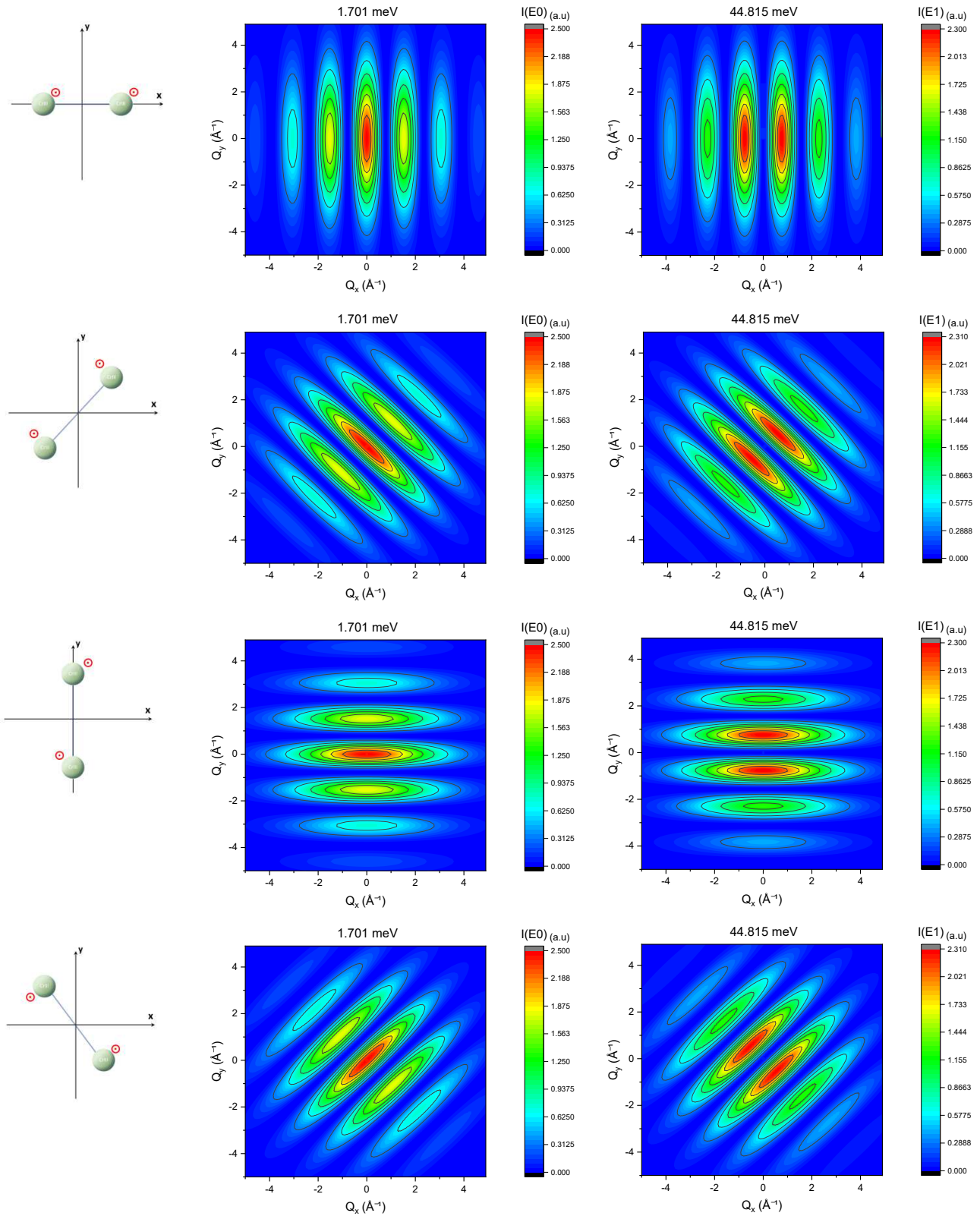Figure 7.8: INS intensity peaks for Cr^{3+} dimer in single crystal sample at T=0 K with anisotropy along z-axis and rotating the positions of the ions in the x-y plane.

It is not straightforward to derive information from the intensity pattern shown, and it is even more complicated to directly derive details on the *phi* angles. We therefore focus on verifying any variation in the intensity pattern for different configurations of *phi* angles, in particular the same configurations that led to the same peaks in the powder sample analysis.

We then show different graphs for both peaks, changing the ideal configuration of the anisotropy axes by adding the same $\Delta\phi$ value to each of the *phi* angles of the three Dy ions. The result is shown in the figure 7.13 where the left column shows the patterns for the first peak (120.669 meV) and the right column those for the second peak (120.693 meV). Centrally, the geometric pattern of the anisotropy axes of the molecule is shown.
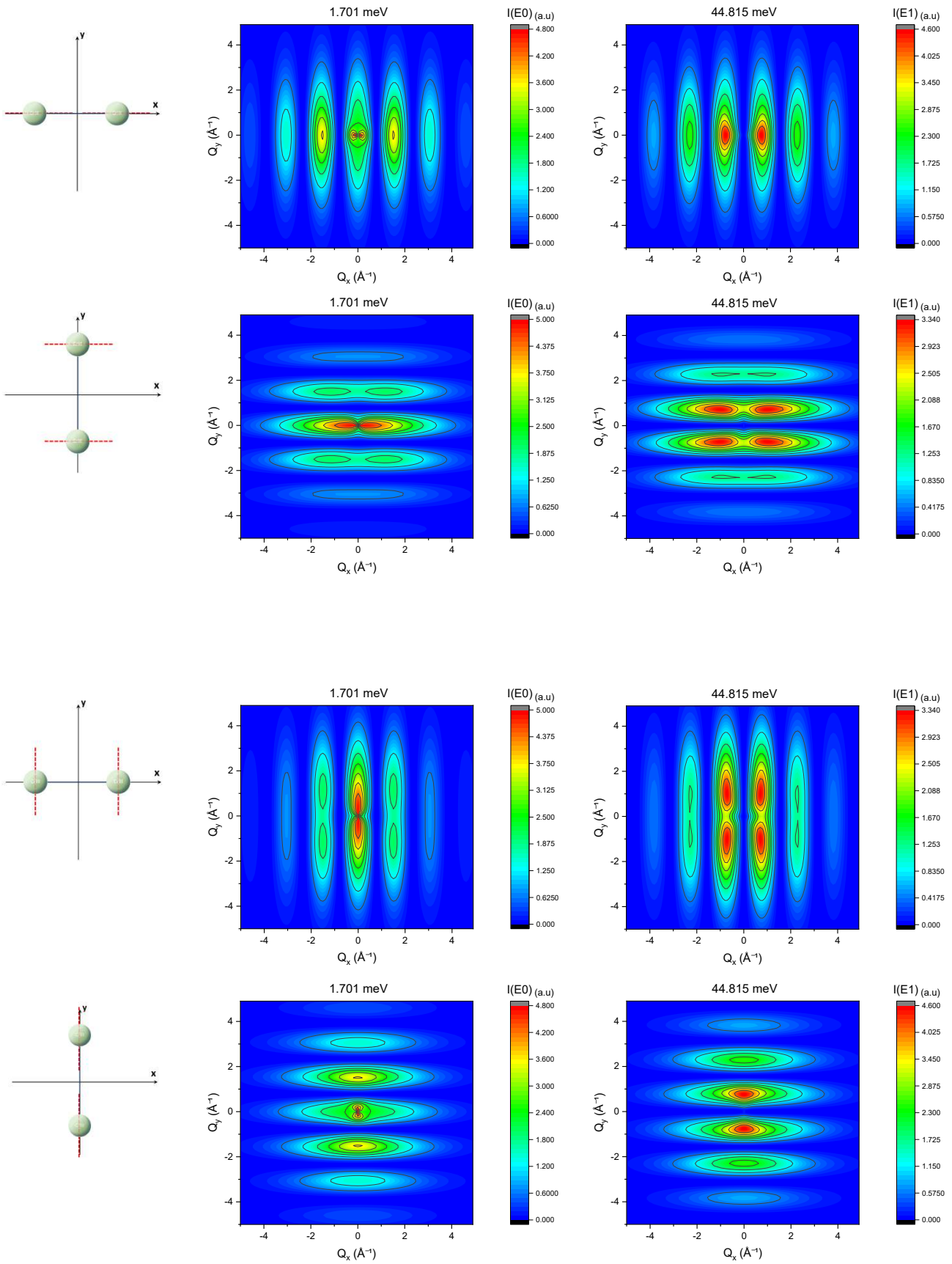
Figure 7.9: INS intensity peaks for Cr^{3+} dimer in single crystal sample at T=0 K with anisotropy along the x-axes (on top) and along the y-axes (in the bottom) and rotating the positions of the ions in the x-y plane.
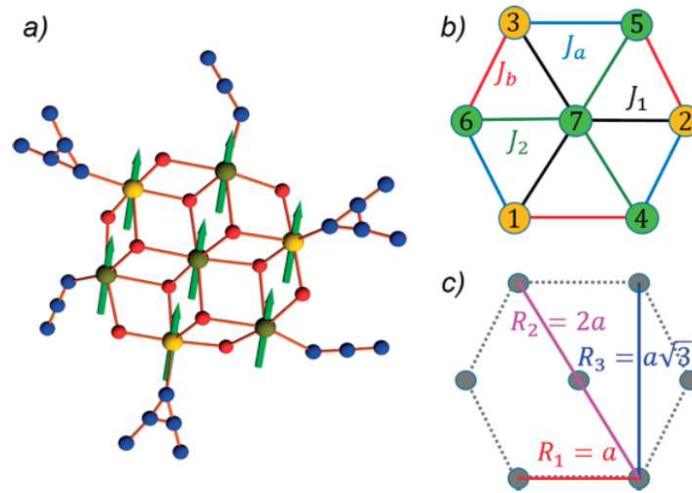
Figure 7.10: Mn_7 molecule scheme with ball-and-stick representation (a), interaction coupling between the ions (b) and relative positions of the ions (c). [22]
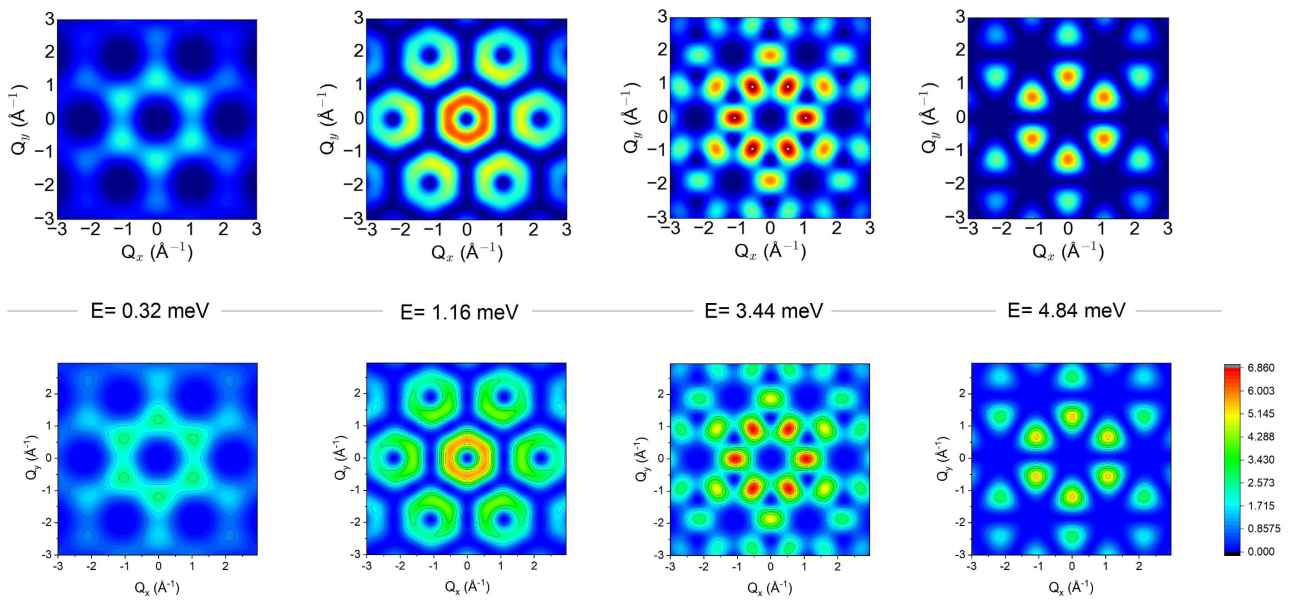

Figure 7.11: Comparison between the article $Q_x - Q_y$ plane intensity plots (top row), with the one obtained via *ow_ins*.
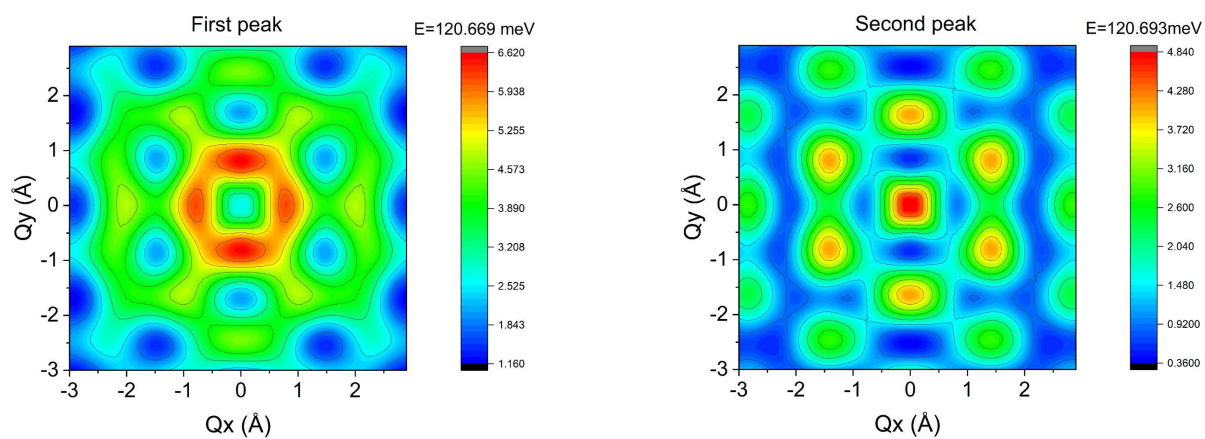
Figure 7.12: Single Crystal INS simulation on Al_2Dy_3 in the ideal configuration focusing on the two intensity peaks highlighted in figure 7.2.
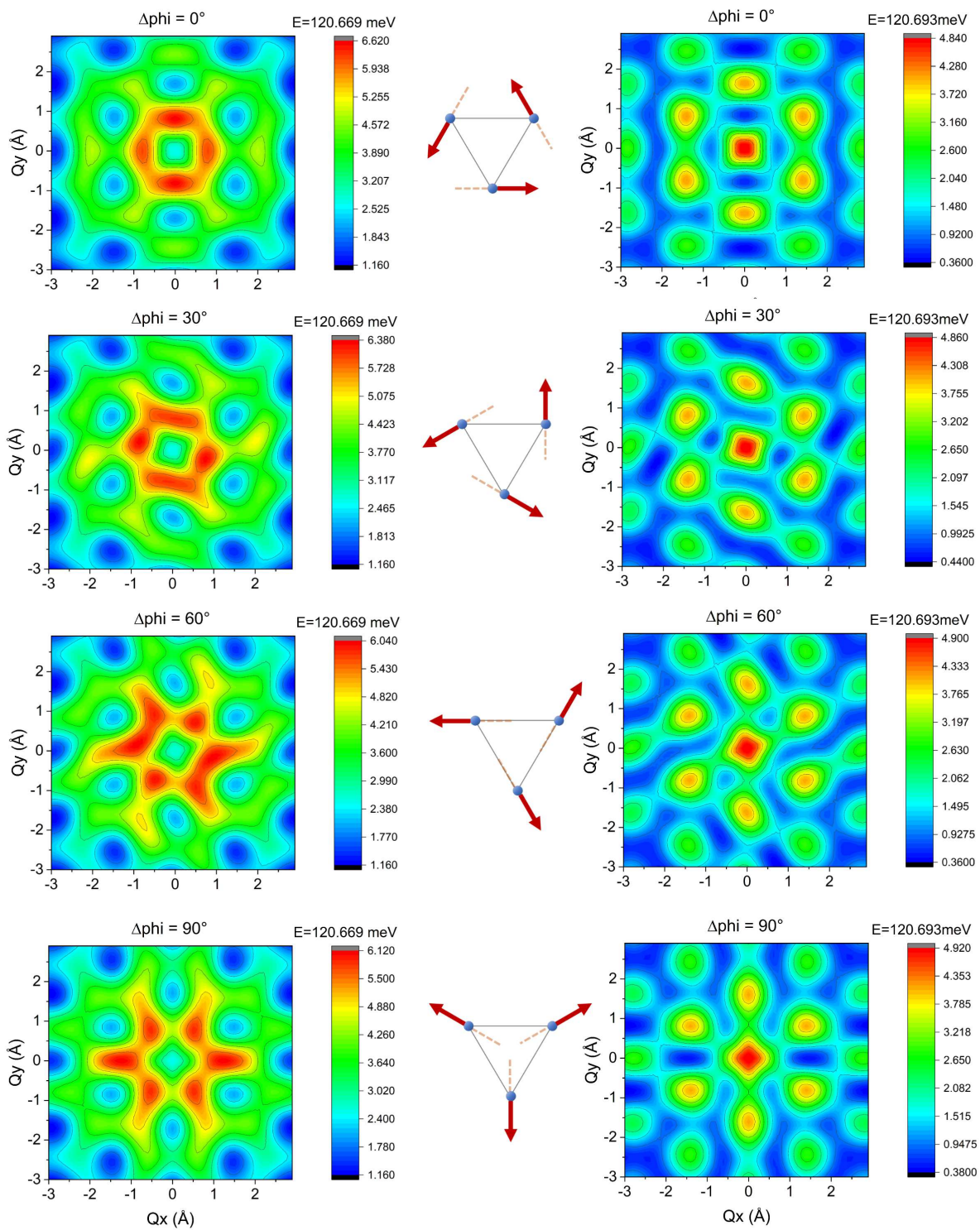
Figure 7.13: Single Crystal INS simulation on Al_2Dy_3 with $theta = 90°$ and adding a same quantity $\Delta\phi$ to each of the three phi angles, for the two peaks highlighted in figure 7.2.

Conclusions

In this thesis work, the magnetic properties of a molecule, Al_2Dy_3, were analyzed, with the aim of obtaining information on its possible toroidicity, a quantity described by the toroidal moment $\hat{\boldsymbol{t}} = \frac{g\mu_B}{2} \sum_{i=1,2,3} \boldsymbol{r_i} \times \hat{\boldsymbol{S_i}}$. The molecule has been modelled as three triangularly positioned Dy ions, since they are the only atoms to have magnetic properties.

Thus, starting with powder magnetization and susceptibility data, a set of parameters that well describes the experimental data was obtained. In particular, apart from some magnetic corrections on the mass and diamagnetic correction, we have seen how the anisotropy axes are inclined with $theta \simeq 21°$. Thus those axes are almost perpendicular to the plane in which the three Dy ions lie. However, no information could be obtained on the phi angles.

The energy levels of the molecule and its toroidal moment have then been explored by varying the parameters on which the Hamiltonian depends. It was possible to associate a toroidal moment to each of the 8 states (doublet + sextet) forming the low-energy states. These 8 states are well separated from the rest of high-energy states due to the large value of anisotropy considered. In the hypothesis of an ideal arrangement of the anisotropy axes, the Al_2Dy_3 molecule considered would thus show 8 different possibilities of toroidal moment, in which the magnitude of the one in the sextet is larger by a factor of 2 than the magnitude of the one in the doublet.

Finally, an inelastic neutron scattering experiment with the Al_2Dy_3 molecule has been simulated, showing that intensity peaks between the 8 lowest energy states are not possible. Instead, two peaks were found considering the two immediately following energy levels. But again, even from these intensity peaks, simulated for a powder sample, it is not possible to obtain sufficient information on the orientation of the anisotropy axes and thus on the toroidicity.

Therefore, a new code was implemented to simulate the inelastic neutron scattering on a single crystal. From these simulations, two different intensity patterns (one for each transition peak) were obtained as a function of the coordinates of the scattering vector $\mathbf{Q}$ on the ions plane. By progressively varying the configuration of the anisotropy axes from a perfectly toroidal to a non-toroidal behaviour, a variation in this pattern is observed, giving hope for the observation of azimuthal angles phi by single crystal experiment.

The results obtained with the single crystal INS are still preliminary, and confirmation and more study are needed. In particular, if the successful single-crystal patterns were confirmed, it would be possible to proceed with experimental measurements at the Institut Laue-Langevin in Grenoble, where there is a neutron source.

Aknowledgements

And finally the time has come to thank a few people who directly or indirectly took part in this work. A big thank you goes to Prof. Waldmann, who welcomed me into the group without having half a clue who I was, and I hope that at least some of this trust has been repaid. And still on the subject of professors, thanks also to Prof. Mattei, thanks to whom I emerged from the labyrinth of Erasmus bureaucracy and who was present throughout the project.

I would also like to thank my family, who gave me great (financial) support, and all the new friends I met who helped make this period great.

Finally, a big thank you to (almost dr.) Julius Mutschler, emperor of the master students, runner and mountain climber and in the end a good friend, a little less so when drunk. But without his support this work would not have been possible. So to give him credit I show in figure 7.14 one of his works of art, pen on paper (also known as Julius papers).
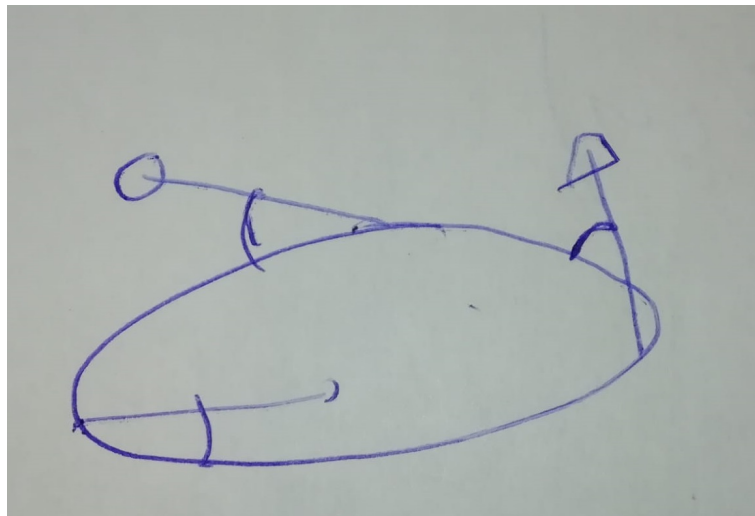

Figure 7.14: Julius Mutschler, 27 July 2022, pen on paper, "The spin representation".

Bibliography

[1] Schlenker M. Du Trémolet de Lacheisserie E. Gignoux D., ed. *Magnetism: Fundamentals.* Springer, 2005.

[2] Caneschi A. et al. "Alternating current susceptibility, high field magnetization, and millimeter band EPR evidence for a ground S = 10 state in [Mn12O12 (Ch3COO) 16(H2O)4] .2CH3COOH .4H2O." In: *American Chemical Society* 113 (1991).

[3] Chibotaru L. F. et al. "The origin of nonmagnetic Kramers doublets in the ground state of dysprosium triangles: evidence for a toroidal magnetic moment." In: *Angew Chem Int Ed Engl.* 47 (2008).

[4] Ungur L. et al. "Single-molecule toroics in Ising-type lanthanide molecular clusters". In: *Chem Soc Rev* 43 (2014).

[5] Affronte M. et al. "Single molecule magnets for quantum computation". In: *Journal of Physics D: Applied Physics* 40 (2007).

[6] Atzori M. and Sessoli R. "The Second Quantum Revolution: Role and Challenges of Molecular Chemistry". In: *American Chemical Society* 141 (2019).

[7] Gaita-Ariño A. et al. "Molecular spins for quantum computation". In: *Nature Chemistry* 11 (2019).

[8] Godfrin C. et al. "Operating Quantum States in Single Magnetic Molecules: Implementation of Grover's Quantum Algorithm". In: *Physical Review Letters* 119 (2017).

[9] Luzon J. et al. "Spin Chirality in a Molecular Dysprosium Triangle: The Archetype of the Noncollinear Ising Model". In: *Phisical Review Letters* (2008).

[10] Stevens K. W. H. "Proceedings of the Physical Society. Section A Matrix Elements and Operator Equivalents Connected with the Magnetic Properties of Rare Earth Ions". In: *Proceedings of the Physical Society* 65 (1952).

[11] Villain J. Gatteschi D. Sessoli R. *Molecular Nanomagnets.* Oxford University Press, 2006.

[12] del Barco E. et al. "Magnetic Quantum Tunneling in the Single-Molecule Magnet Mn12-Acetate". In: *Journal of Low Temperature Physics* 140 (2005).

[13] Odom B. et al. "New Measurement of the Electron Magnetic Moment Using a One-Electron Quantum Cyclotron". In: *Phisical Review Letters* (2006).

[14] Tanner B.K. *Introduction to the Physics of Electrons in Solids.* Cambridge University Press, 1995.

[15] Press W. H. et al. *Numerical Recipes: The Art of Scientific Computing.* Cambridge University Press, 2007.

[16] Ding L. "Field-tunable toroidal moment in chiral-lattice magnet". In: *Nature communications* (2021).

[17] Furrer A., ed. *Neutron Scattering in Novel Materials.* World Scientific, 2000.

[18] Strässle T. Furrer A. Mesot J., ed. *Neutron Scattering in Condensed Matter Physics.* World Scientific, 2009.

[19] Squires G.L. *Introduction to the Theory of Thermal Neutron Scattering.* Dover Publications, INC., 1996.

[20] Waldmann O. and Güdel H. U. "Many-spin effects in inelastic neutron scattering and electron paramagnetic resonance of molecular nanomagnets". In: *Phys. Rev. B* 72 (2005).

[21]   Tang J. et al. "Dysprosium Triangles Showing Single-Molecule Magnet Behavior of Thermally Excited Spin States". In: *Angewandte Chemistry* (2006), pp. 1729–1733.

[22]   Prsa K. and Waldmann O. "Inelastic Neutron Scattering Intensities of Ferromagnetic Cluster Spin Waves". In: *European Journal of Inorganic Chemistry* (2019), pp. 1128–1141.

[23]   Furrend A. Böni P. and Schefer J. "Principles of Neutron Scattering". In: *Neutron Scattering in Novel Materials*. Ed. by Albert Furrer editor. World Scientific, 2000, pp. 1–21.